Thesis for Doctor of Philosophy

Hydrogen Embrittlement in TRIP and TWIP Steels

Ryu, Joo Hyun (류 주 현)

Department of Ferrous Technology

(Computational Metallurgy)

Graduate Institute of Ferrous Technology

Pohang University of Science and Technology

2012

Hydrogen Embriittlement in TRIP and TWIP Steels 2012 Ryu, Joo Hyun

TRIP강과 TWIP강의 수소취성

Hydrogen Embrittlement in TRIP and TWIP Steels

Hydrogen Embrittlement in TRIP and TWIP Steels

By

Ryu, Joo Hyun
Department of Ferrous Technology
(Computational Metallurgy)
Graduate Institute of Ferrous Technology
Pohang University of Science and Technology

A thesis submitted to the faculty of Pohang University of Science and Technology in partial fulfillments of the requirements for the degree of Doctor of Philosophy in the Graduate Institute of Ferrous Technology (Computational Metallurgy)

Pohang, Korea
29 May 2012

Approved by

Prof. Bhadeshia, H. K. D. H.	Prof. Suh, Dong-Woo
Major Advisor	Co-advisor

Hydrogen Embrittlement in TRIP and TWIP Steels

Ryu, Joo Hyun

This dissertation is submitted for the degree of Doctor of Philosophy at the Graduate Institute of Ferrous Technology of Pohang University of Science and Technology. The research reported herein was approved by the committee of Thesis Appraisal

29 May 2012

Thesis Review Committee

Chairman: Prof. Suh, Dong-Woo	(Signature)
Member: Prof. Kim, Han Soo	(Signature)
Member: Prof. Kim, Kyoo Young	(Signature)
Member: Prof. Lee, Chong Soo	(Signature)
Member: Dr. Lee, Sang Yoon	(Signature)

Preface

This dissertation is submitted for the degree of Doctor of Philosophy at Pohang University of Science and Technology. The research reported herein was conducted under the supervision of Professor H. K. D. H. Bhadeshia, Professor of Computational Metallurgy in the Graduate Institute of Ferrous Technology, Pohang University of Science and Technology and Professor of Physical Metallurgy, University of Cambridge, between March 2008 and May 2012.

This work is to the best of my knowledge original, except where acknowledgements and references are made to previous work. Neither this, nor any substantially similar dissertation has been or is being submitted for any other degree, diploma or other qualification at any other university. This dissertation does not exceed 60,000 words in length.

Part of this work has been submitted and some has been published as follows:

Ryu, J. H., Kim, D. I., Kim, H. S., Bhadeshia, H. K. D. H., Suh, D. W.: Strain partitioning and mechanical stability of retained austenite. *Scripta Materialia*, Vol. 63 (2010) pp. 297–299

Ryu, J. H., Chun, Y. S., Lee, C. S., Bhadeshia, H. K. D. H., Suh, D. W.: Effect of Deformation on Hydrogen Trapping and Effusion in TRIP-Assisted Steel. *Accepted to Acta Materialia*, 2012

Ryu, J. H., Kim, S. K., Lee, C. S. Bhadeshia, H. K. D. H., Suh, D. W.: Effect of Al on Hydrogen Embrittlement in TWIP Steel. *To be submitted,* 2012

Joo Hyun Ryu

2012

DFT Ryu, Joo Hyun
20080958 Hydrogen Embrittlement in TRIP and TWIP Steel
Department of Ferrous Technology (Computational Metallurgy)
2012, 133 p
Advisor: Prof. Bhadeshia, H. K. D. H and Prof. Suh, Dong-Woo
Text in English

Abstract

The presence of hydrogen in steels often leads to embrittlement which is sensitive to the strength level of steel. High strength steels developed recently for automotive applications, such as the TRIP and TWIP steels, also suffer from such embrittlement even though they contain austenite which is relatively immune to brittle behaviour.

One of the important factors for the embrittlement in TRIP steels is the mechanical stability of retained austenite. The stability is attributed usually to chemical composition, size and shape of austenite. The work presented here demonstrated that another factor, the partitioning of strain between phases with different mechanical properties, can dramatically influence the stability.

The trapping of hydrogen at a variety of sites in TRIP steels with the different austenite mechanical stabilities has been characterised using thermal desorption spectroscopy, and the results have been modelled using diffusion theory to predict the desorption quantitatively as a function of phase transformation. The work shows that the hydrogen dissolved in austenite can be regarded as trapped given the large activation energy of diffusion, which is greater than that of generic traps found within the ferrite and martensite. As a consequence, the deformation-induced martensitic decomposition of the austenite leaves the inherited hydrogen in a more mobile state. The mechanical degradation of the steel by hydrogen is therefore more

pronounced in TRIP steel containing austenite which is relatively less stable to martensitic transformation during deformation.

It was discovered that an aluminium addition in TWIP steel improves the resistance to hydrogen embrittlement, using tensile tests with dynamic hydrogen charging. This is because the Al suppresses not only the hydrogen-induced ε martensite reported to be susceptible to embrittlement but also mechanical twins which act as diffusible-hydrogen trap sites based on their huge density of dislocations. The hydrogen can be accumulated on the twins and grain boundaries during the tensile test through hydrogen transport via dislocations, thereby increasing a crack initiation there. Consequently, fracture surfaces were observed with both intergranular and transgranular mode of failure. It was demonstrated that transgranular fracture surfaces were parallel to interfaces between the ε martensite and austenite, or to mechanical twin boundaries.

Contents

Preface……...……...i

Abstract…….…...……..…….……ii

Nomenclature and Abbreviations……..vii

Chapter 1: Introduction……..1

1.1 Hydrogen in Iron and Steel……...1

1.1.1 Solubility……1

1.1.2 Diffusivity……..3

1.1.3 Hydrogen-Trap Interactions……...5

1.1.4 Hydrogen Trapping and Transport by Dislocations……...9

1.1.5 Thermal Desorption Analysis……..11

1.1.6 Theories of Hydrogen Embrittlement……..15

1.1.6.1 Internal Pressure……..15

1.1.6.2 Surface Energy…….16

1.1.6.3 Decohesion……..16

1.1.6.4 Hydrogen Enhanced Plasticity……17

1.1.6.5 Hydrogen Enhanced Strain-Induced Vacancies……..19

1.2 Hydrogen Embrittlement in TRIP Steels……21

1.2.1 TRIP Steels……...21

1.2.2 Mechanical Degradation by Hydrogen……23

1.2.3 Hydrogen Effect on the Stability of Austenite…….28

1.2.4 Thermal Desorption Analysis for TRIP Steels…….28

1.3 Hydrogen Embrittlement in TWIP Steels……...29

1.3.1 TWIP Steels…….29

1.3.2 Effect of Hydrogen on the Stacking Fault Energy……...30

1.3.3 Delayed Fracture……..34

Chapter 2: Strain Partitioning & Mechanical Stability of Retained Austenite

2.1 Introduction……36

2.2 Experimental……...37

2.3 Results and Discussion……...39

2.4 Summary……44

Chapter 3: Effect of Deformation on Hydrogen Trapping and Effusion in TRIP-Assisted Steel……45

3.1 Introduction……45

3.2 Experimental……..46

3.2.1 Alloys……...46

3.2.2 Microstructural Characterisation……..46

3.2.3 Hydrogen Charging and Thermal Desorption……..47

3.2.4 Mechanical Test……...48

3.3 Results and Discussion……...48

3.3.1 Microstructure……..48

3.3.2 Hydrogen Effusion……...51

3.3.3 Simultaneous Effusion from Traps and Austenite……...59

3.3.4 Tensile Properties and Trap Transfer……...62

3.4 Summary……66

Chapter 4: Effect of Al on Hydrogen Embrittlement in TWIP Steel……67

4.1 Introduction……67

4.2 Experimental……...67

4.2.1 Alloys……...67

4.2.2 Microstructural Characterisation……..68

4.2.3 Hydrogen Charging and Thermal Desorption……..68

4.2.4 Mechanical Test……...69

4.2.5 Hydrogen Microprint Technique……..70

4.3 Results and Discussion……...70

4.3.1 Microstructure……70
4.3.2 Degradation of Tensile Properties……...73
4.3.3 Hydrogen Trapping……..77
4.3.4 Hydrogen-Induced ε Martensite……...85
4.4 Summary……91

Chapter 5: Conclusions……...92

Appendix: Approach to Develop Stainless δ-TRIP Steel……...94
A.1 Introduction……94
A.2 Alloy Design and Manufacture……..94
A.3 Experimental……..94
A.4 As-cast Microstructures...……..97
A.5 Bainitic Transformation……...100
A.6 Effect of Hot-Rolling……...104
A.7 Summary……..110

References……..111
Acknowledgements……132
Curriculum Vitae……..……133

Nomenclature

b	magnitude of the Burgers vector
C^H	hydrogen concentration
C_T^H	total hydrogen content
C_L^H	hydrogen content in solid solution
C_z^H	hydrogen concentration at a depth z
C_s^H	hydrogen concentration at surface
D_i	region where hydrogen atoms are subjected to an attractive force
D_0	pre-exponential term
D^H	diffusion coefficient of hydrogen
D_α^H	diffusion coefficient of hydrogen in ferrite lattice
D_γ^H	diffusion coefficient of hydrogen in austenite lattice
D_{app}^H	apparent diffusion coefficient of hydrogen
E_d	activation energy for lattice diffusion
E_a	trap activation energy
E_b	trap binding energy
E_b	saddle point energy
G_L	free energy at lattice site
G_T	free energy at trap site
J^H	diffusion flux of hydrogen
k	Boltzmann constant
k^H	constant which adjust the units
L_{gb}	grain boundary length per unit area
M_s	martensite start temperature
n	empirical order of reaction
n_j^H	fraction of j trap sites that are filled with hydrogen

N^H	number of trap sites per unit volume
N^L	number of lattice sites per unit volume
N_j^H	number of j trap sites per unit volume
$N_{dislocation}^H$	number of dislocation trap sites per unit volume
$N_{grain\ boundary}^H$	number of grain boundary trap sites per unit volume
P^H	hydrogen gas pressure
R	gas constant
t_P	duration of plastic deformation
T	absolute temperature
T_P	temperature at which maximum hydrogen desorption occurs
x	position
x_s^H	atom fraction of dissolved hydrogen
x_0^H	atom fraction of hydrogen at equilibrium
X	fraction reacted
z	depth from surface
z_p	penetration depth during plastic deformation
z_L	penetration depth by lattice diffusion
α	ferrite
α′	martensitic ferrite with body-centered cubic structure
γ	austenite
ε	martensitic ferrite with hexagonal-closed packed structure
ρ	surface density of atoms in the $\{111\}_\gamma$ plane
$\sigma^{\gamma/\varepsilon}$	interfacial energy per unit area between γ and ε
HMT	hydrogen microprint technique
SFE	stacking fault energy
TDS	thermal desorption spectroscopy
TEM	transmission electronviiimicroscopy

TRIP	transformation-induced plasticity
TWIP	twinning-induced plasticity
XRD	X-ray diffraction

Chapter 1: Introduction

1.1 Hydrogen in Iron and Steels

The presence of hydrogen in iron and steels is deleterious to mechanical properties, an effect commonly referred to as hydrogen embrittlement. The effect was first documented by Johnson (1875), who reported that the hydrogen causes a reduction in ductility and fracture stress. Since then, it has been shown that the phenomenon is not restricted to the iron and steels but occurs in many materials such Ni, Al, Ti, Zr, Ta, Nb, V, W and Mo (Dayal and Parvathavarthini, 2003) although the individual mechanisms may not be identical. Concentrations as small as 1 part per million by weight can be enough to cause premature failure in steels. The steels pick up the hydrogen during processes such as picking, electroplating without baking, welding in damp condition and excessive cathodic protection. The hydrogen can enter the steels during service. Contact with an aqueous environment may cause the following reactions to occur (Dayal and Parvathavarthini, 2003):

$$x\mathrm{Fe} + y\mathrm{H_2O} \rightarrow \mathrm{Fe}_x\mathrm{O}_y + 2y\mathrm{H}^+ \tag{1.1}$$

$$\mathrm{H}^+ + e \rightarrow \mathrm{H} \tag{1.2}$$

The embrittlement is associated with a combination of several elementary steps like surface adsorption, transport through a structure, accumulation (trapping) and fracture. At least five mechanisms for the hydrogen embrittlement have been proposed. In all of them, the transport of hydrogen and its trapping behaviour are important aspects for the embrittlement in steels.

1.1.1 Solubility

Sieverts (1929) demonstrated that the solubility of hydrogen in iron is proportional to the square root of external hydrogen pressure for the reaction

$$\frac{1}{2}\mathrm{H_2} \rightleftarrows \underline{\mathrm{H}} \tag{1.3}$$

where $\underline{\mathrm{H}}$ is hydrogen in solution. Quick and Johnson (1978) showed that the atom fraction of hydrogen x_0^H in equilibrium at pressure P^H in atm is

$$x_0^H = 0.00185\sqrt{P^H}\exp\left(-\frac{3440}{T}\right) \quad (1.4)$$

where T is the absolute temperature in the range 322 to 779 K. The dissolved hydrogen is in interstitial sites in ferritic iron (Bernstein, 1969) due to its relatively large partial molar volume of about 2×10^{-6} m^3 mol^{-1} (Load, 1967) and small atom diameter of 1.06 Å. The x_0^H in equilibrium at a pressure of one atmosphere is only about 1.9×10^{-8} at room temperature. This value increases moderately with temperature and to a maximum 1.7×10^{-4} (3 parts per million by weight, ppmw) at the ferrite to austenite transformation temperature.

A homogeneous distribution of about 1.9 hydrogen atoms for every 10^8 atoms of iron is not sufficient to cause embrittlement at room temperature. However, greater quantities of total hydrogen can be introduced into the metal, because it can associate with internal traps such as dislocations, grain boundaries and vacancies. Fig. 1.1 shows the solubility in α-iron as a function of temperature at a pressure of one atmosphere (Kiuchi and McLellan, 1983). It is clear that the degree of scatter increases rapidly as the temperature decreases and the data do not conform to an Arrhenius plot of $\ln x_0^H$ vs $1/T$ as presented in Eq 1.4. The trapping effect is measureable below 550 K for a trap density of 10^{23} m^{-3} and is negligible for smaller trap densities (Hirth, 1980). This value of trap density is an upper limit for grain boundaries while dislocation trap densities can exceed this at room temperature. However, recovery reduces the dislocation density above 550 K. Thus the trapping there has little effect on the measurable solubility in α-iron.

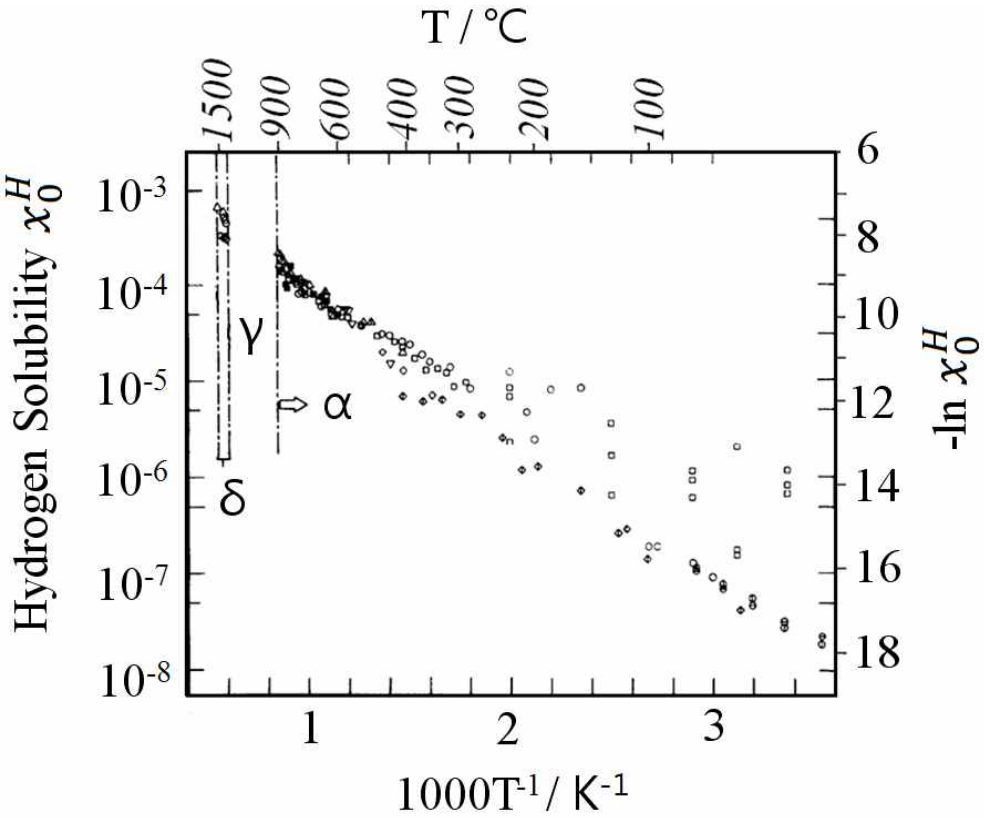

Fig. 1.1: Hydrogen solubility in α-iron as a function of temperature (Kiuchi and McLellan, 1983).

1.1.2 Diffusivity

Hydrogen transport is often controlled by lattice diffusion when it is in solution. The driving force for the diffusion is a gradient of chemical potential due to concentration variations. The diffusion flux of hydrogen J^H is represented with Fick's first law in one dimension as:

$$J^H = -D^H \frac{\partial C^H}{\partial x} \tag{1.5}$$

where C^H is the hydrogen concentration and x is the position. The diffusivity D^H can be expanded in terms of temperature and activation energy E_d for the lattice diffusion in α-iron as:

$$D_{\alpha}^{H} = D_0 \exp\left(-\frac{E_d}{RT}\right) \quad (1.6)$$

where D_0 is pre–exponential term and R is the gas constant, and it can be measured using permeability experiments.

Fig. 1.2 shows the apparent diffusivity of hydrogen D_{app}^{H} in well-annealed α-iron (Kiuchi and McLellan, 1983). Above about 400 ℃, the apparent diffusion coefficient is close to the diffusivity D_{α}^{H} ($m^2\ s^{-1}$) of hydrogen in the perfect lattice, given by (Gonzalez, 1969):

$$D_{\alpha}^{H} = 0.78 \times 10^{-7} \exp\left(-\frac{7949}{RT}\right) \quad (1.7)$$

where E_d is about 7.9 kJ mol^{-1}.

However, the diffusivity of hydrogen deviates markedly from that predicted by the extrapolation of high temperature data and the degree of discrepancy increases sharply at lower temperatures. The apparent activation energy in the low temperature region is in the range 33 to 38 kJ mol^{-1} (Choo and Lee, 1982), while in the high temperature region it is about 7.9 kJ mol^{-1}. This is because hydrogen diffusion is interrupted by the trap sites which capture and delay migrating of hydrogen atoms at the low temperature.

Darken and Smith (1949) were the first to suggest that the delayed diffusion of hydrogen in cold worked iron is caused by an attractive interaction between the lattice dissolved hydrogen and the microstructural imperfections. The mobility of dissolved hydrogen in cold worked iron was then analyzed by Oriani (1970) assuming local equilibrium between the mobile and the trapped populations. The apparent diffusivity (D_{app}^{H}) becomes

$$D_{app}^{H} = D_{\alpha}^{H}\left[1 + \frac{N^H}{N^L}\exp\left(\frac{E_b}{RT}\right)\right]^{-1} \quad (1.8)$$

where N^L is the number of normal sites per unit volume, N^H is the number of trap sites per unit volume and E_b is binding energy between the trap and hydrogen. The binding energy was found to be about 27.2 kJ mol^{-1} by using the equation and available data obtained from various absorption, permeation and out-gassing experiments. The possibility of multiple trapping sites was suggested for hydrogen

in deformed iron including not only dislocations but also internal interfaces and microscopic cracks. Hagi *et al.* (1979) compared the diffusivity of single crystal and polycrystal α-iron and also concluded that the trapping in grain boundaries decrease the apparent diffusivity more than 100 times at room temperature.

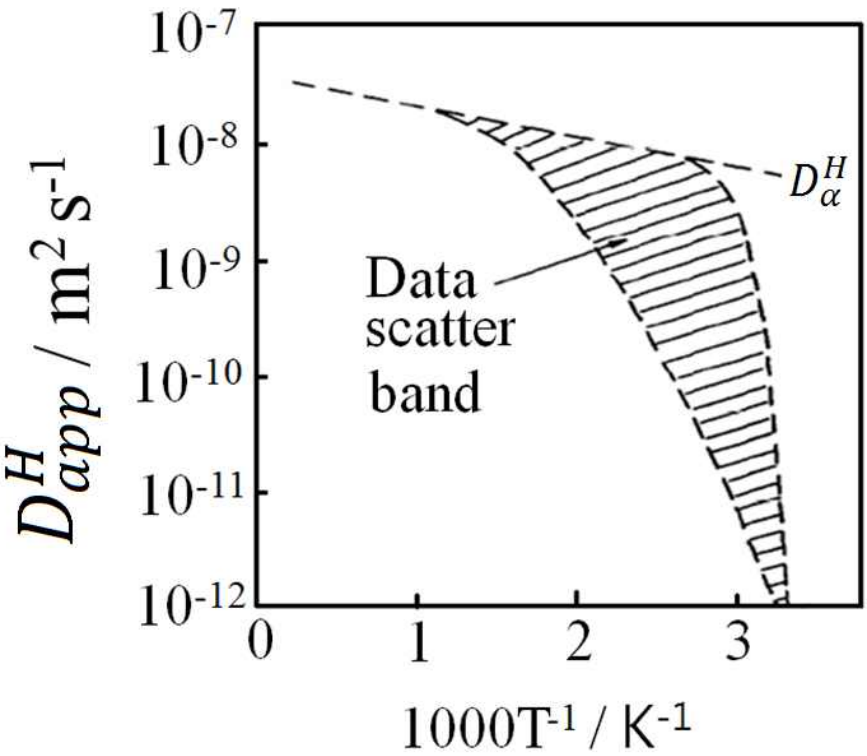

Fig. 1.2: Approximate data scatter band encompassing 36 individual H-diffusivity measurement sets for well-annealed α-iron (Kiuchi and McLellan, 1983).

1.1.3 Hydrogen-Trap Interactions

Pressouyre (1979) has classified types of trap sites by their physical nature for hydrogen in steels as shown in Fig. 1.3. If in Fig. 1.3a, there exists a force that pushes the hydrogen atoms in a preferred direction, it is easy for an atom in site B to jump into site A than into C. When the lattice is distorted, the average jump height is changing from site to site like Fig. 1.3b. From these reasons, it is possible to

distinguish between two extreme types of traps such as attractive and physical trap. The attractive trap is illustrated in Fig. 1.3c. It is a region of the lattice, of dimension D_i, where hydrogen atoms are subjected to an attractive force. The force includes stress fields (Oriani, 1970) induced by defects such as dislocations, coherent and semicoherent grain boundaries, and crack tips. Furthermore, the attractive force also can be generated by thermal gradients and chemical potential gradients. A schematic of the physical traps is shown in Fig. 1.3d. Such a trap owes its existence to modifications of the crystal lattice, where it is energetically more favourable for the hydrogen to stay. High angle grain boundaries, incoherent particle-matrix interface and voids are in that situation. The edge dislocation which has both the attractive character due to the mechanical force induced by the stress field and the physical character to the tensile region of the core is the case of mixed traps in Fig. 1.3e.

Strength of a trap site depends on a binding energy of hydrogen atom to the trap. The definition of binding energy and its relationship to other thermodynamic parameters are shown in Fig. 1.4 (Lee and Lee, 1986). Table 1 gives the energies of various trap sites in α-iron.

The total hydrogen content in a steel (C_T^H) is the sum of that which is in solid solution (C_L^H) and a residue trapped at various sites (Hirth, 1980):

$$C_T^H = C_L^H + \sum_j k^H n_j^H N_j^H \tag{1.9}$$

where n_j^H is the fraction of j trap sites that are filled with hydrogen, N_j^H is the number of trap sites per unit volume, and k^H is a constant which adjusts the units of the terms in the summation. When considering trapping at dislocations, $N_{dislocations}^H \approx \pi b^{-1}\rho$ where ρ is the dislocation density and b is the magnitude of the Burgers vector. Similarly, $N_{grain\ boundary}^H \approx b^{-2}L_{gb}$ where L_{gb} is the grain boundary length per unit area of observation (Mine *et al.,* 2010).

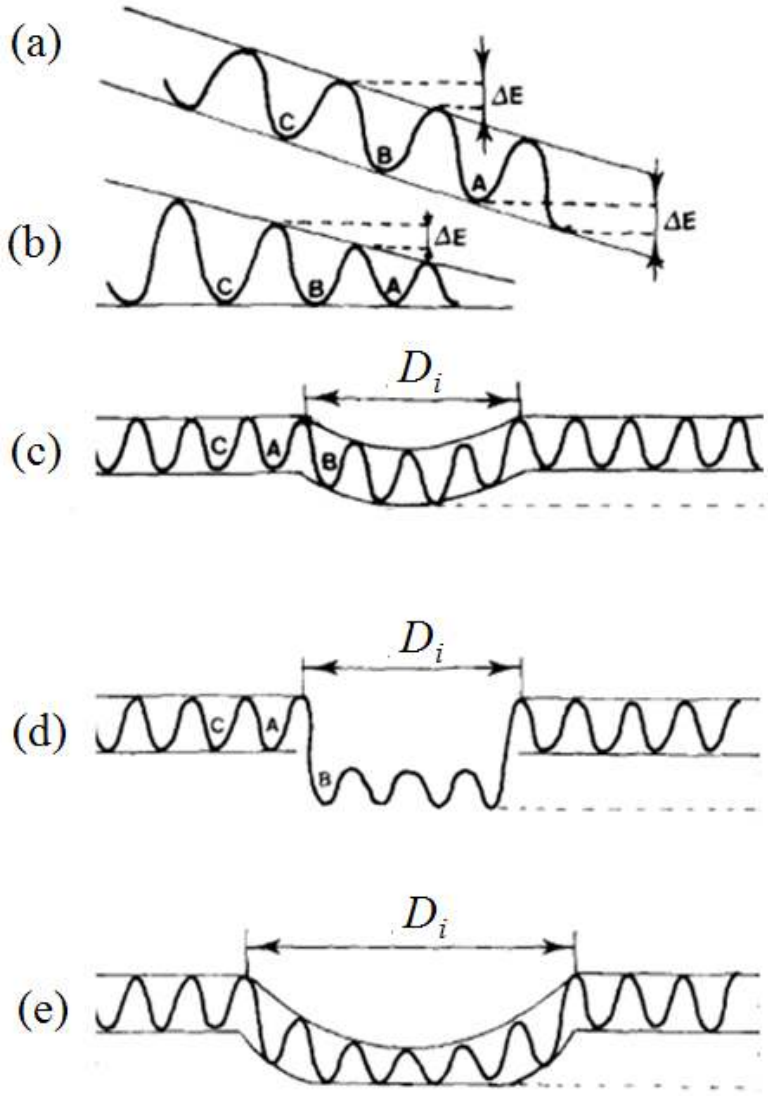

Fig. 1.3: Schematic of energy steps necessary to the diffusion of a hydrogen atom through a metal lattice, in some particular cases: (a) Existing attractive force from left to right, (b) distorted lattice, (c) attractive trap, (d) physical trap, (e) mixed trap (Pressouyre, 1979).

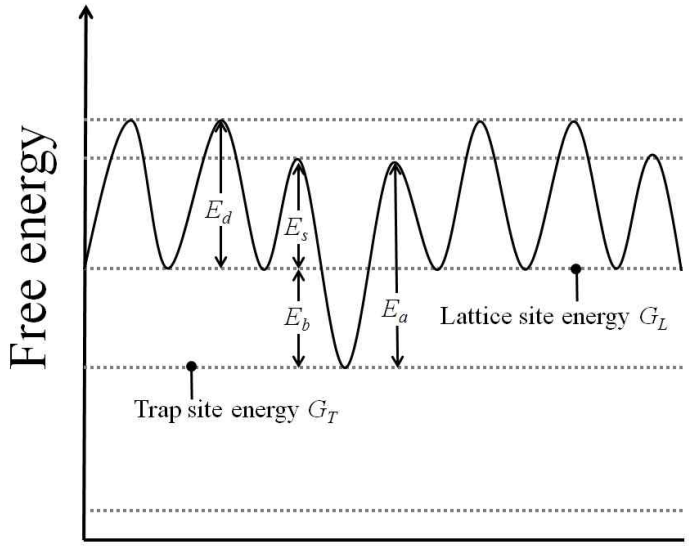

Fig. 1.4: Energy level of hydrogen around trap sites: E_d, diffusion activation energy in normal lattice; E_s, saddle point energy; E_a, trap activation energy (Lee and Lee, 1986). The binding energy is a difference between the lattice site energy G_L and trap site energy G_T (E_b=G_L-G_T).

Table 1. Binding energies (E_b) of various trap sites in α-iron.

Trap site	E_b (kJ mol^{-1})	References
Grain boundary	9.6	Choo and Lee, 1982
Dislocation elastic stress field	20	Gibala and Kumnick, 1977
Dislocation core	59	Kumnick and Johnson, 1980
Free surface	70	Chornet *et al*., 1972
AlN-ferrite interface	65	Podgurski and Oriani, 1972
MnS-ferrite interface	72	Lee and Lee, 1983
Fe_3C-ferrite interface	84	Lacombe *et al*., 1977
Al_2O_3-ferrite interface	79	Lee and Lee, 1986
TiC-ferrite interface	87	Lee and Lee, 1984
Vacancy	46	Gibala and Kumnick, 1977

1.1.4 Hydrogen Trapping and Transport by Dislocations

The binding energy between hydrogen and dislocations in α-iron can be inferred from several experimental techniques. First, the binding energies with dislocations of around 27 kJ mol^{-1} are obtained using internal friction measurements (Zielinski *et al.*, 1977). The hydrogen permeation studies by Kumnick and Johnson (1980) on high purity α-iron deformed by cold-rolling have shown that the dislocations are trap sites for hydrogen, but with a very high E_b of 60 kJ mol^{-1} and trap densities in the range of 10^{20}-10^{23} m^{-3} as a function of cold work. They have concluded that the traps are probably either jogs in dislocations or imperfection debris left behind by moving dislocations. Choo and Lee (1982) used thermal desorption analysis to identify types of trapping site and to evaluate the corresponding binding energies. They monitored the release of hydrogen from charged specimens during heating at uniform heating rates. The binding energy was inferred from observed peak temperatures of desorption curves at different heating rates and to be 19.2 kJ mol^{-1} for the dislocations.

In contrast to the trapping, it is also known that the dislocation motion during deformation enhances the transport of hydrogen by forming "Cottrell atmospheres" (Tien *et al.*, 1976). Donovan (1976) reported an accelerated evolution of hydrogen during deformation from iron pre-charged, attributed to the release of hydrogen by egressing dislocations. Therefore, the release rate is dependent on the strain as shown in Fig. 1.5 (Louthan *et al.,* 1972).

If the plastic deformation is implemented during exposure to hydrogen then its apparent hydrogen diffusivity is effectively increased. Fig. 1.6 clearly shows the larger concentration of hydrogen attained in the specimen interior by the plastic deformation for nickel (Louthan *et al.,* 1972). The interaction between hydrogen and dislocation enhanced the uptake and penetration depth of hydrogen into the specimen.

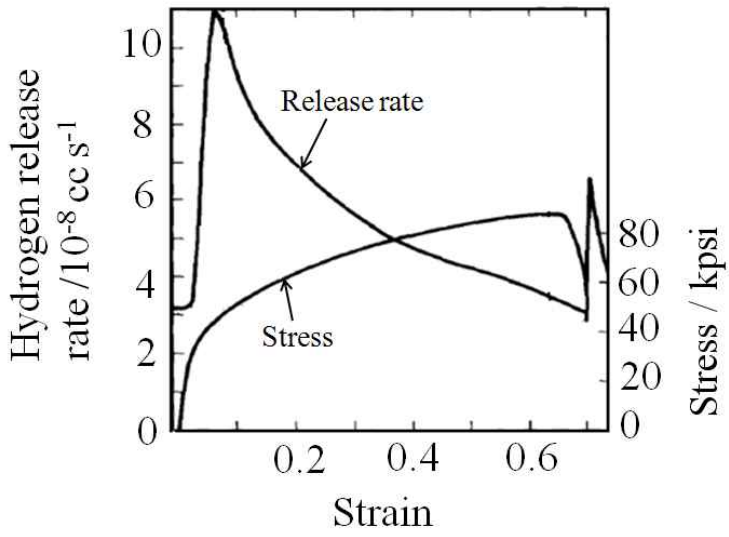

Fig. 1.5: Stress and strain curves and hydrogen release rate as a function of strain for Armco iron pre-charged (Louthan *et al.,* 1972).

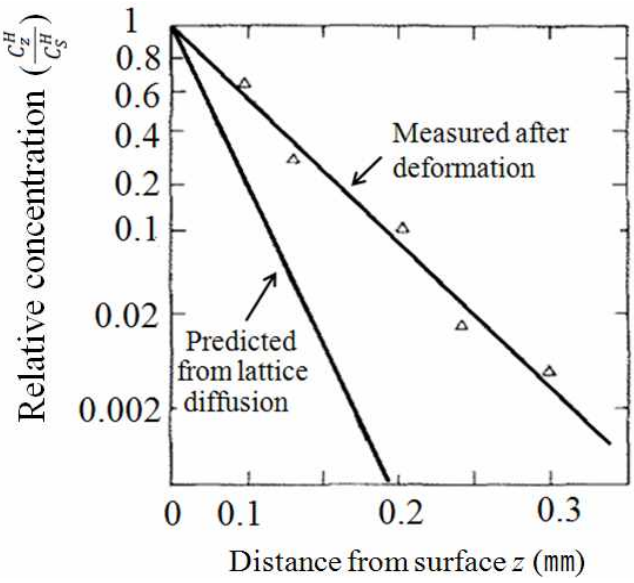

Fig. 1.6: Relative concentration as a function of penetration distance into a nickel tensile specimen deformed during exposure to hydrogen, which is compared with the predicted profile for diffusion only (Louthan *et al.,* 1972). The C_z^H is a concentration of hydrogen at a distance z and C_S^H the concentration at the surface.

A kinetic model for the transport of hydrogen by dislocations with Cottrell atmospheres was proposed by Tien *et al*. (1976). The dislocations can drag or sweep such a cloud of hydrogen atoms which are then be deposited at microstructural locations which are critical during fracture such as grain boundaries, inclusions and microvoids. Defining the maximum penetration distance z_p of hydrogen in plastically deformed metal as

$$z_p = \frac{D_{app}^H}{kT} \cdot \frac{E_b}{30b} t_p \tag{1.11}$$

where k is Boltzmann constant, $30b$ is the interaction distance of the dislocation with its impurity cloud and t_p is the duration of the plastic deformation. In contrast, the penetration depth z_L due to the lattice diffusion is expressed as

$$z_L = \sqrt{6 D_{app}^H t_p} \tag{1.12}$$

Except for very short time of the deformation, *i.e.* milliseconds or less, a value of z_p/z_L is $10^4\sqrt{t_p}$ for $D_{app}^H = 10^{10}$ m^2 s^{-1} or $10^2\sqrt{t_p}$ for $D_{app}^H = 10^{14}$ m^2 s^{-1} taking E_b of the dislocation is to be 0.3 eV (Tien *et al.,* 1976). Thus, the hydrogen transport mode involving dislocations can be effective.

The effect of interactions between the hydrogen and dislocations on diffusion in metals is of two types. First, the hydrogen is trapped in the dislocations generated by prior deformation, or newly introduced during deformation, thus hindering diffusion. However, the hydrogen also can be transported by mobile dislocations during deformation, which enhances the apparent diffusivity. Dislocation trapping and transport are competing process for the transport of hydrogen.

1.1.5 Thermal Desorption Analysis

Thermal desorption analysis (TDA) can help identify different hydrogen trapping states. The technique measures the amount of hydrogen desorbed from specimens heated at a constant rate and derives a relation between the desorption rate and the specimen temperature. This relation is called a hydrogen desorption profile, in which are observed several characteristic desorption peaks at certain temperatures.

Those peaks correspond to the hydrogen trapping states. From hydrogen desorption profiles, it is possible to obtain information on hydrogen states and to identify the trapping sites such as vacancies, dislocations, grain boundaries, and interfaces between different phases.

Fig. 1.7 shows a schematic illustration of the typical set-up for the thermal desorption analysis with gas chromatography. When the charged specimen is heated in the furnace, the trapped hydrogen starts to evolve. The desorbed hydrogen moves into the gas chromatograph with the aid of a carrier gas He. Then the amount of desorbed hydrogen is monitored by a detector. A standard gas mixture of He + H_2 can be used for the calibration of hydrogen content.

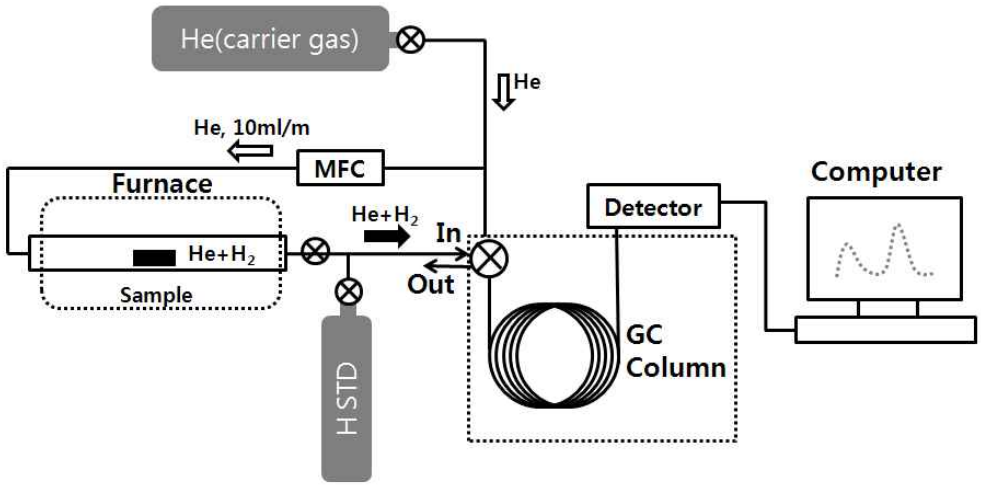

Fig. 1.7: Schematic illustration of the typical set-up for thermal desorption analysis with gas chromatography.

For the analysis of the desorption profile, the hydrogen escape rate from the trap sites is traditionally expressed as (Kissinger, 1957):

$$\frac{dX}{dt} = A(1-X)^n \exp\left(-\frac{E_a}{RT}\right) \tag{1.13}$$

where $\frac{dX}{dt}$ is the desorption rate, *A* is constant, X is the fraction "reacted" and n is the empirical order of reaction. To reach a maximum desorption rate with uniform heating rate with the assumption of a first–order reaction,

$$\frac{d}{dt}\left(\frac{dX}{dt}\right) = \frac{dX}{dt}\left(\frac{\emptyset E_a}{RT^2} - A\exp^{-E_a/RT}\right) = 0 \tag{1.14}$$

or

$$\frac{\emptyset E_a}{RT_p^2} = A\exp^{-E_a/RT_p} \tag{1.15}$$

where $\emptyset$ is heating rate and T_p is the temperature at which the maximum hydrogen desorption occurs. Taking the logarithm of Eq. 1.15 and differentiating with respect to $(1/T_p)$ yields

$$\frac{\partial \ln\left(\emptyset/T_p^2\right)}{\partial(1/T_p)} = -\frac{E_a}{R} \tag{1.16}$$

If $\emptyset$ and T_p are known, the activation energy of trap site can be evaluated from the slope of a $\ln(\emptyset/T_p^2)$ *vs* $(1/T_p)$ plot. Choo and Lee (1982) found that the activation energies for hydrogen evolution from trap sites are 17.2, 26.8 and 35.2 kJ mol^{-1} for the grain boundary, dislocation, and microvoid respectively by using the Kissinger equation and thermal desorption analysis. However, the Kissinger equation does not represent the physical events appropriately for the hydrogen diffusing out of free surfaces of thick samples. First–order kinetics of the type described by the Kissinger analysis are more appropriate for cases where the reaction occurs homogeneously throughout the assembly so that specimen dimensions are not relevant.

To deal with this, Yamaguchi and Nagumo (2003), and Yurioka *et al*. (2005) analyzed the thermal desorption profiles using the diffusion equation such as

$$\frac{dC^H}{dt} = D_{app}^H \frac{d^2C^H}{dx^2} \tag{1.17}$$

where *x* is a distance which determines the gradient of concentration. The apparent diffusivity of hydrogen in the steels depends on the temperature, the density and binding energy of trap sites as shown in the Eq. 1.8. Then the equation gives the

hydrogen distribution in a specimen along the thickness of specimen as time increases. The difference between the initial and residual hydrogen distribution is the desorbed hydrogen, and the time is linearly converted to the temperature at the uniform heating rate, thus yielding the thermal desorption profiles. The density and binding energy of trap sites can be evaluated by the fitting of the calculated curves to experimental data. Fig. 1.8 shows that the increase in both the binding energy and density of trap sites shifts the calculated desorption curves to higher temperature, indicating a reduced apparent diffusivity of hydrogen due to the trapping effect (Yamaguchi and Nagumo, 2003).

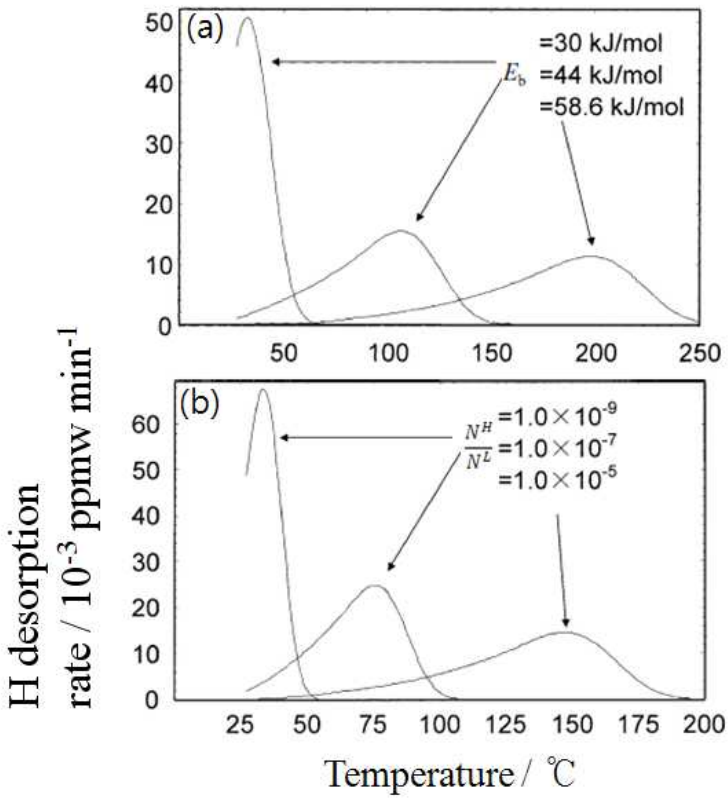

Fig. 1.8: Effect of (a) binding energy and (b) density of trap sites on the predicted thermal desorption curves of a ferritic steel (Yamaguchi and Nagumo, 2003).

1.1.6 Theories of Hydrogen Embrittlement

Hydrogen embrittlement is dependent on many variables such as concentration, temperature, level and type of applied or residual stress, the strength of steel, microstructural constituents and surface conditions of the material. Numerous mechanisms have been proposed to explain the effect of hydrogen on the mechanical properties.

1.1.6.1 Internal Pressure

The oldest and the most popular mechanism for hydrogen embrittlement has been the pressure theory. This attributes it to the entry of atomic hydrogen into the metal and its accumulation at internal defects such as voids (Zapffe and Sims, 1941). The high pressure developed by formation of molecular hydrogen enhances void growth and crack propagation. This phenomenon certainly occurs, as shown by blister formation during exposure of the material to a hydrogen-rich environment as represented in Fig. 1.9.

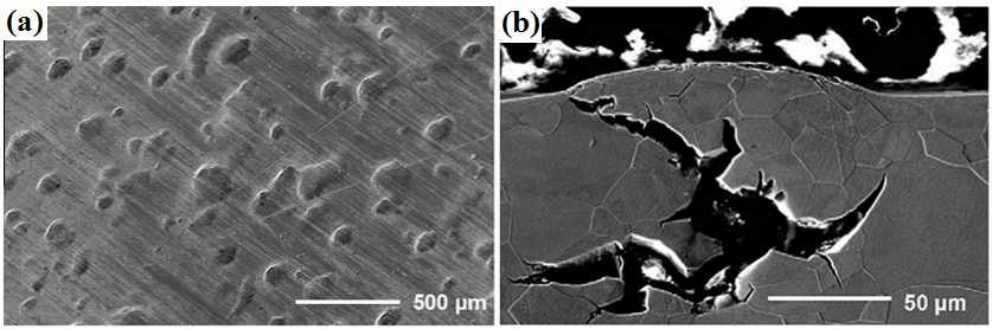

Fig. 1.9: Blister formation in pure iron charged for 1 h at a charging current density of 500 A m^{-2} with arsenic-poisoned electrolyte. (a) Surface and (b) cross section of the specimen (Escoba *et al.,* 2011).

However, the observation of stable crack growth (Hancock and Johnson, 1965) in hydrogen gas at low sub-atmospheric pressure demonstrates that the pressure mechanism cannot be general. Although, the argument also has been made that the

transport of hydrogen by dislocation could create the large internal pressures in voids even when the external pressure was low as in the above case (Tien *et al*., 1976). On the other hand, the supersaturation by dislocation transport was greatly overestimated. The attainable supersaturation in the void is only a factor of 2 or 3 (Johnson and Hirth, 1976).

1.1.6.2 Surface Energy

According to this theory hydrogen absorption decreases the energy of the surface created in crack propagation, thus lowering the work of fracture (Petch and Stables, 1952). However, this cannot explain why the reduction of surface free energy by adsorption of oxygen does not have the same deleterious effect as the hydrogen (Lynch, 1979). A possibility for the oxygen effect is that it preferentially adsorbs at the crack tip, blocking ingress of hydrogen (Simmons *et al.*, 1978).

1.1.6.3 Decohesion

The idea is that dissolved hydrogen lowers the cohesive energy of the iron lattice because the interatomic distance increases due to the filling of the *d* bands of the transition metal by the electron of the hydrogen atom as shown in Fig. 1.10 (Troiano, 1960). Recently, first principles calculations by Takano (2010) showed that the hydrogen reduces the cohesive energy in cleavage fracture on the usual {100} planes of single crystal α-iron.

The decohesion theory for the hydrogen-induced crack propagation (Oriani and Josephic, 1974) postulates that the highly elastically stressed region at the crack front lowers sufficiently the chemical potential of dissolved hydrogen, which then attains a concentration that is several orders of magnitude larger than normal. This in turn lowers the maximum cohesive energy between the atoms. Cracks propagate when the local maximum tensile stress normal to the plane of the crack, which is controlled by the externally applied load and the crack-front geometry, is equal to the maximum cohesive energy.

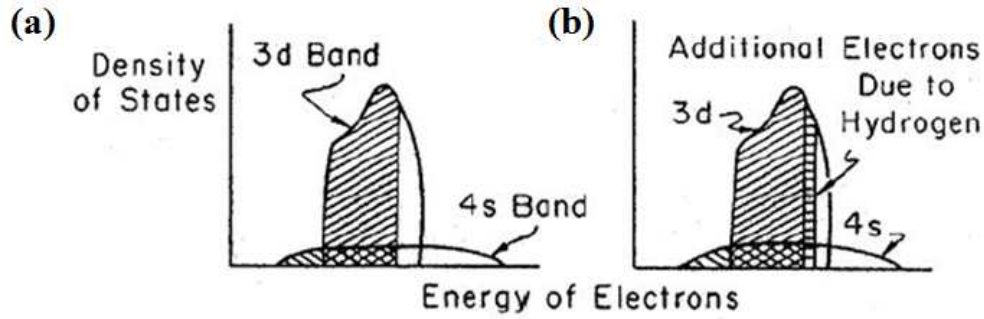

Fig. 1.10: Schematic density of states in (a) hydrogen-free and (b) hydrogenated nickel (Troiano, 1960).

1.1.6.4 Hydrogen Enhanced Plasticity

Birnbaum and Sofronis (1994) proposed a mechanism in which the hydrogen formed the atmosphere around the dislocations and other elastic stress centers. The redistribution of hydrogen atmosphere around two edge dislocations on the same slip plane and with the same Burgers vector is shown in Fig. 1.11. As a result of the linear superposition of the stress fields of the dislocations the distribution of hydrogen around the dislocations changes as they move closer together. The effect of this hydrogen redistribution on the shear stress experienced by one dislocation due to the presence of the other is shown in Fig. 1.12. The shear stress decreases with increasing hydrogen concentration. Consequently, the effect of hydrogen is to reduce the applied stress necessary to move an edge dislocation with a hydrogen atmosphere. This is supposed to lead to localized deformation in the vicinity of fracture surface because the elastic stress field at a crack tip attracts the hydrogen which in turn softens the region by facilitating slip (Tabata and Birnbaum, 1984), giving the appearance of brittle fracture. It causes the formation of shallow and numerous microscopic ductile voids which rapidly link in order to give what appears to be a macroscopically brittle fracture.

However, the mechanism of ductile-void formation is not explained, and the number density required to produce an apparently brittle fracture is not clear. There are results which contradict the softening theory, and show instead that the hardness

increases in proportion to the hydrogen content (Vaughan and de Morton, 1956a). Similarly, the yield strength has been reported to increase in a hydrogen mild steel (Vaughan and de Morton, 1956b). Attempts have been made to explain the inconsistencies by arguing that the presence of hydrogen limits the number of slip systems that operate, thereby leading to an increase of strength in austenitic steel (Ulmer and Altstetter, 1991).

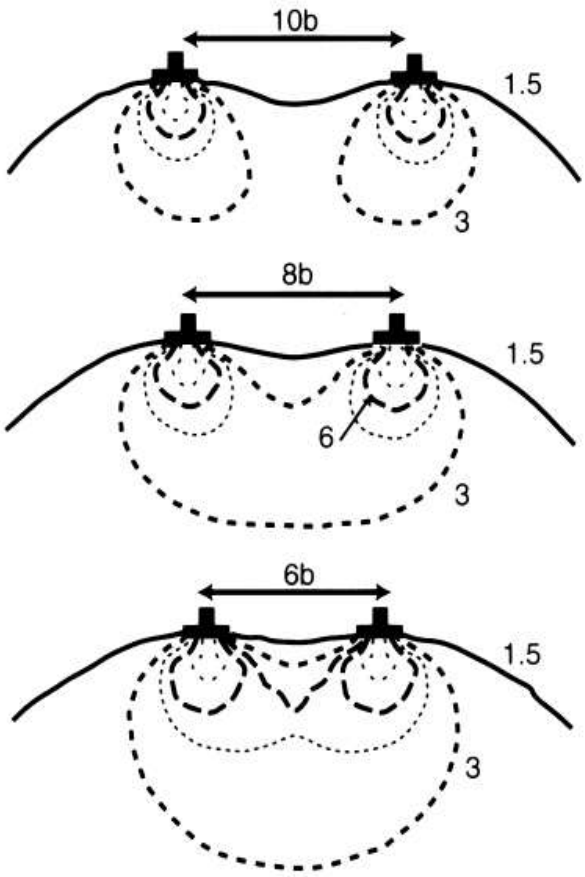

Fig. 1.11: Changes in the hydrogen isoconcentration lines around two edge dislocations on the same slip plane and with the same Burgers vector as a function of separation distance (Birnbaum and Sofronis, 1994).

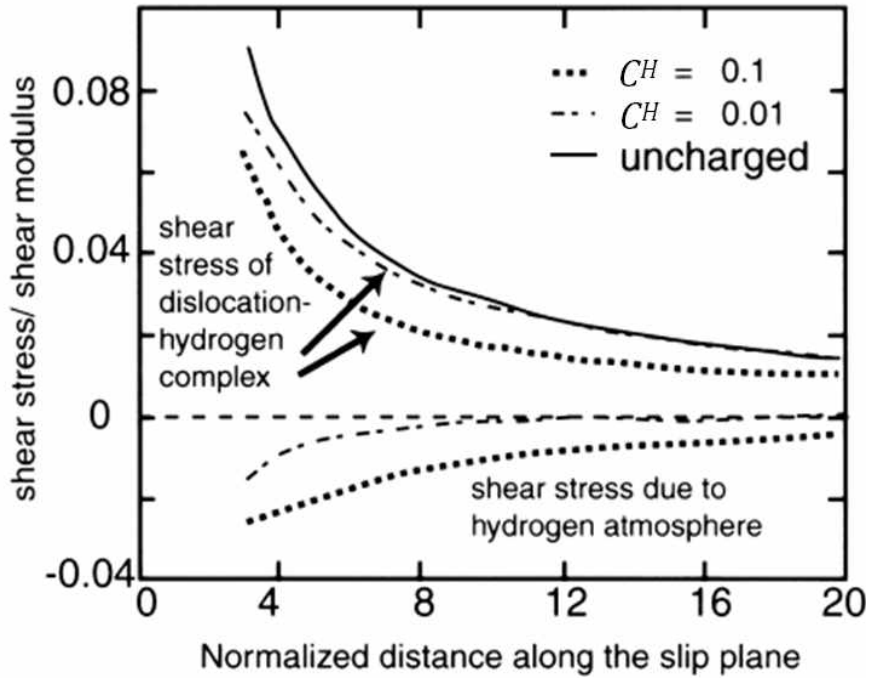

Fig. 1.12: Effect of the redistribution of hydrogen on the shear stress experienced by one edge dislocation due to the presence of the other on the same slip plane. Calculations were carried out for the parameters characteristic of Nb at 300K (Birnbaum and Sofronis, 1993).

1.1.6.5 Hydrogen Enhanced Strain-Induced Vacancies

The fractographic features of fine and shallow dimple surfaces (Gordon *et al*, 1992), and fine striations along slip plane traces (Terasaki *et al*., 1998) which indicate ductile fracture in hydrogen embrittlement are often observed. The effect of hydrogen on promoting ductile crack initiation and reducing crack growth resistance (Nagumo *et al.,* 2001) have been demonstrated with low-alloyed steels. The model proposes that the primary function of hydrogen in degradation is to enhance the strain-induced creation and agglomeration of vacancies, thus promoting easy formation and linking of microvoids for the fracture process (Nagumo, 2004). Creation of a high density of strain-induced vacancies has been theoretically estimated with dislocation dynamics (Cuitino and Ortiz, 1996), suggesting vacancy

agglomeration as a mechanism of the microvoid formation observed in the crack front area in iron (Gardner and Wilsdorf, 1980). Furthermore, the presence of hydrogen during the plastic deformation enhances the generation of vacancies (Takai *et al.* 2008). It was demonstrated that the hydrogen absorption capacity increases in α-iron because of the enhanced creation of strain-induced defects as shown in Fig. 1.13 when the hydrogen was present during the straining. However, the annealing at low temperature of 200 ℃ for the sample strained with hydrogen, totally eliminates the hydrogen effect on increasing strain-induced defects, indicating that the defects are mostly point defects such as vacancies. Sakaki *et al.* (2006) utilized positron life time measurement to observe directly the increase of vacancy generation with the aid of the hydrogen during the deformation. Nagumo *et al.* (2003) observed that an amorphous zone developed beneath tensile fracture surfaces of hydrogen charged ferritic steel due to lattice instability, attributed to the formation of a high density of vacancies with the aid of hydrogen. It also has been found that a vacancy density far exceeding thermal equilibrium values is created under a high pressure and high temperature hydrogen atmosphere, resulting from hydrogen–vacancy interactions that reduce the effective formation energy of vacancies in iron (McLellan and Xu, 1997).

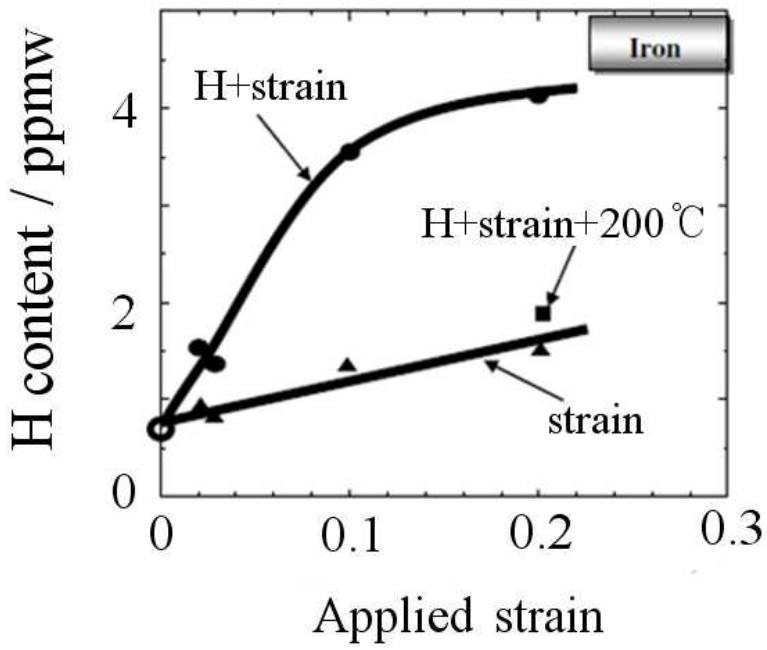

Fig. 1.13: Content of hydrogen absorbed to saturation in α-iron samples after straining with and without hydrogen charging. The absorbed content for the sample given annealing at 200 ℃ for 2 h after straining with hydrogen charging is also shown (Takai *et al.,* 2008).

1.2 Hydrogen Embrittlement in TRIP Steels

1.2.1 TRIP Steels

Transformation induced plasticity (TRIP) steel was developed primarily for the automotive industry to attain weight reduction and to improve impact safety of vehicles. The steels consist predominantly of allotriomorphic ferrite with 15-30% of carbon-enriched retained austenite (Matsumura *et al*., 1992; Sakuma *et al*., 1991; Sugimoto *et al*., 1992). The steels utilize the transformation of the retained austenite during the course of deformation to optimise the mechanical properties (Scott and Drillet, 2007). The mechanical driving force due to stress, can make the transformation possible above the martensite-start temperature M_s by supplying the shortfall of the necessary thermodynamic driving force [Patel *et al*., 1953]. This is

illustrated schematically in Figure 1.15. The free energy change, ΔG_1, available at the M_s temperature is the critical driving force necessary for transformation. At a temperature T_1 above M_s, the magnitude of the free energy change for transformation, ΔG_2, is less than the critical driving force, ΔG_1. Martensite can form at this temperature only if the additional energy of a magnitude U, so that $U + \Delta G_2 = \Delta G_1$. This can be done by applying stress. The transformation becomes possible at the temperature higher than M_s through the work done by external stress, as a mechanical driving force, adding to the available chemical free energy change. The higher the temperature above M_s the greater is the magnitude of the stress required. However, the strength of the austenite diminishes at high temperatures. When the stress required for transformation exceeds that of austenite, plastic strain precedes transformation. This makes it difficult to provide further mechanical driving force so a temperature limit termed M_d is reached, above which austenite does not transform.

A moderate stability of retained austenite is required to retard the onset of necking during the deformation and to achieve strength/ductility balance. If transformation is exhausted at small plastic strains then the protection against a necking in-stability is lost, and if the austenite is too stable then it does not contribute to strain hardening at stress concentrations. The stability of retained austenite is affected mainly by the chemical composition (Le-Houillier *et al*., 1971; Syn *et al.,* 1978; Duchateau and Guttmann, 1981; Takahashi and Bhadeshia, 1991), grain size (Lesilie and Miller, 1964; Bai *et al*., 1998; Yang and Bhadeshia, 2009) and shape (Bhadeshia and Edmonds, 1983).

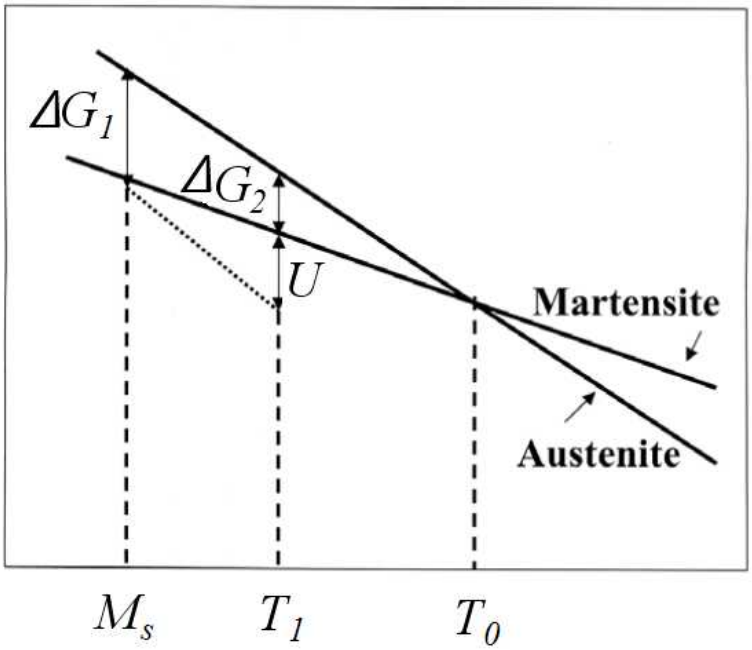

Fig. 1.15: A shortfall in driving force for martensitic transformation above the M_s temperature can be compensated by the application of stress [Chatterjee 2006].

1.2.2 Mechanical Degradation by Hydrogen

Hydrogen is known to embrittle strong martensitic alloys (Kim *et al.*, 2007; Ham *et al*., 2011). Actually, hard martensite is the most susceptible microstructure in the context of hydrogen embrittlement (Hirth, 1980). Furthermore, martensitic transformation also increases an apparent hydrogen diffusivity in steels, which assists continuous crack propagation. It has been found that the hydrogen had to be continuously transported and accumulated in the crack tip for the crack propagation, thus the crack advance rate was controlled by the hydrogen transport rate (Gerberich *et al.*, 1975; Oriani and Josephic, 1977). Xiukui *et al.* (1989) reported that the apparent diffusivity of hydrogen increased exponentially with the presence of martensite after cold deformation in metastable austenitic stainless steels (Fig. 1.16). Furthermore, Mine *et al*. (2009) showed that, if the austenite containing hydrogen transformed to martensite by the deformation, the excess diffusible

hydrogen induced by the martensitic transformation could move faster to the crack tip through the martensite. This is because the diffusivity of hydrogen in the ferrite is 3–4 orders of magnitude greater than in the austenite at 323K (Murakami *et al*., 2008), and the hydrogen is 10-1000 times more soluble in the austenite than in the ferrite (Kiuchi and McLellan, 1983; Turnbull and Hutchings, 1993).

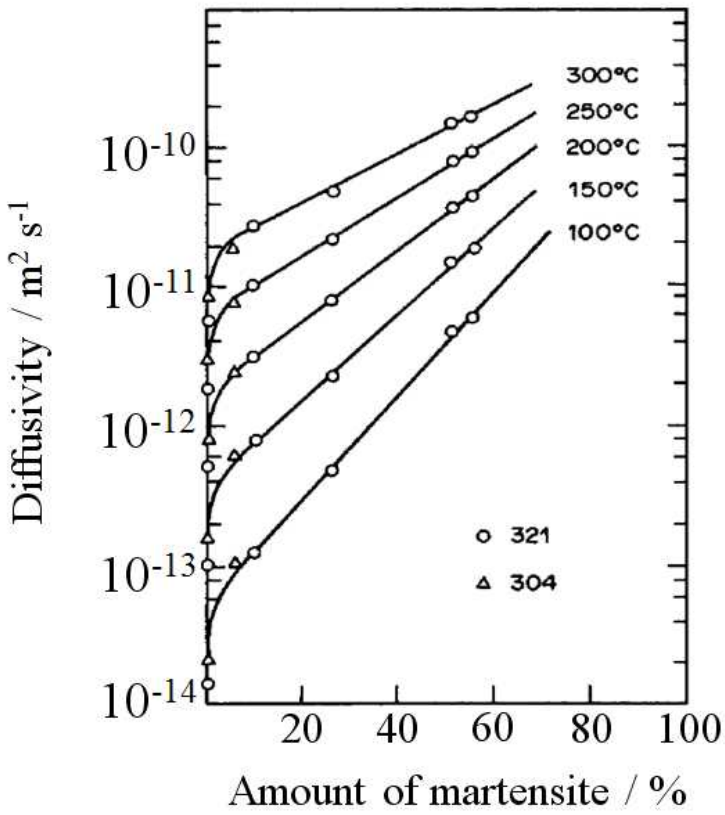

Fig. 1.16: Effect of the martensite fraction on the hydrogen diffusivity in cold-rolled 321 and 304 stainless steels.

As a consequence, there is concern that the high-strength steels such as those which rely on transformation-induced plasticity are also susceptible to such embrittlement (McCoy and Gerberich, 1973; Duprez *et al.*, 2009; Ronevich *et al*., 2010; Sojka *et al.*, 2011). Fig. 1.17 shows the effect of hydrogen on engineering

stress-strain curves with the measured hydrogen contents for TRIP980 steel (Ronevich *et al*., 2010). The increase of hydrogen content results in a decrease of ductility without significant change in the deformation behaviour; the reduction in flow stress based on hydrogen-softening theory was not observed here. Fractographic analysis shows an increasing presence of brittle manner with the increasing of hydrogen content as shown Fig. 1.18 (Lovicu *et al*., 2012).

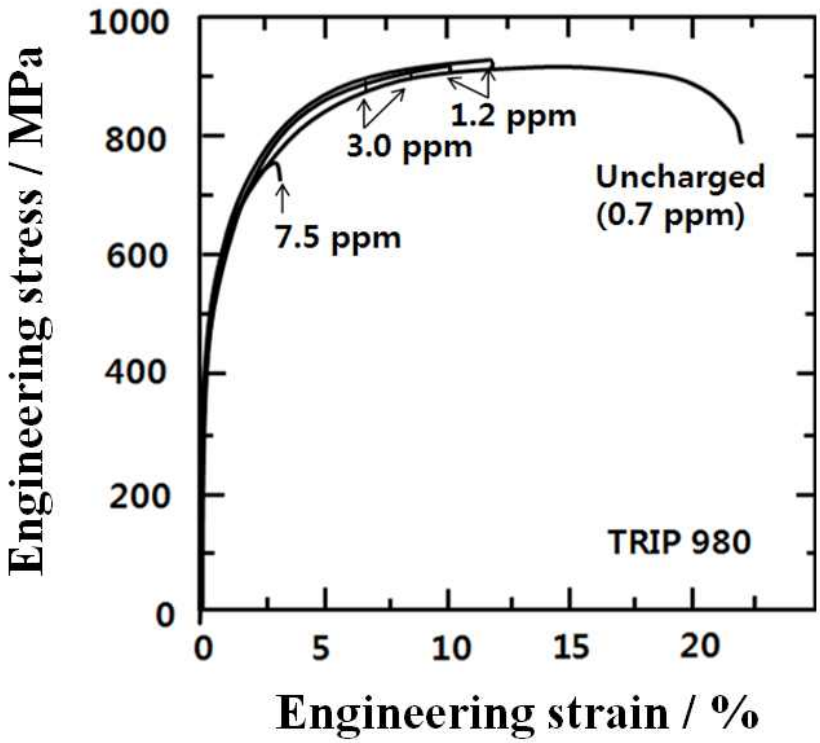

Fig. 1.17: Engineering stress-strain curves for hydrogen charged TRIP980 steels (Ronevich *et al*., 2010).

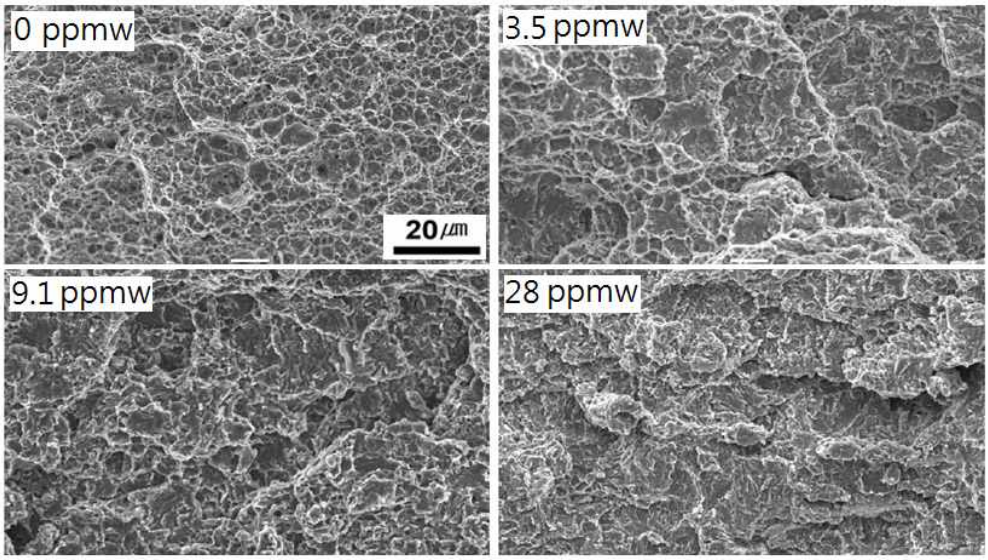

Fig. 1.18: Micrographs of fracture surface of TRIP steel samples charged with different hydrogen contents (Lovicu *et al*, 2012).

1.2.3 Hydrogen Effect on the Stability of Austenite

Many researchers reported the hydrogen-induced phase transformation of austenite to α' or ε martensite by cathodic hydrogen charging in austenitic stainless steels (Ulmer and Altstetter, 1993; Rozenak and Bergman, 2006) as shown in Fig. 1.19 (Yang *et al*., 1999). Rozenak and Bergman (2006) showed that the hydrogen-induced martensitic transformation does not occur if the stability of austenite increases by alloying with solutes such as Ni, Mn and C in austenitic stainless steel. Thus, it is believed that the solute hydrogen can raise the M_s temperature and reduce the stability of austenite (Bentley and Smith, 1986; Hojo *et al.*, 2008). Furthermore, surface cracking has been observed in only specimens in which the hydrogen-induced martensitic transformation is detected after the hydrogen charging in 304 stainless steel (Yang *et al*., 1999). This result implies that the hydrogen can cause the mechanical degradation by decreasing the stability of austenite.

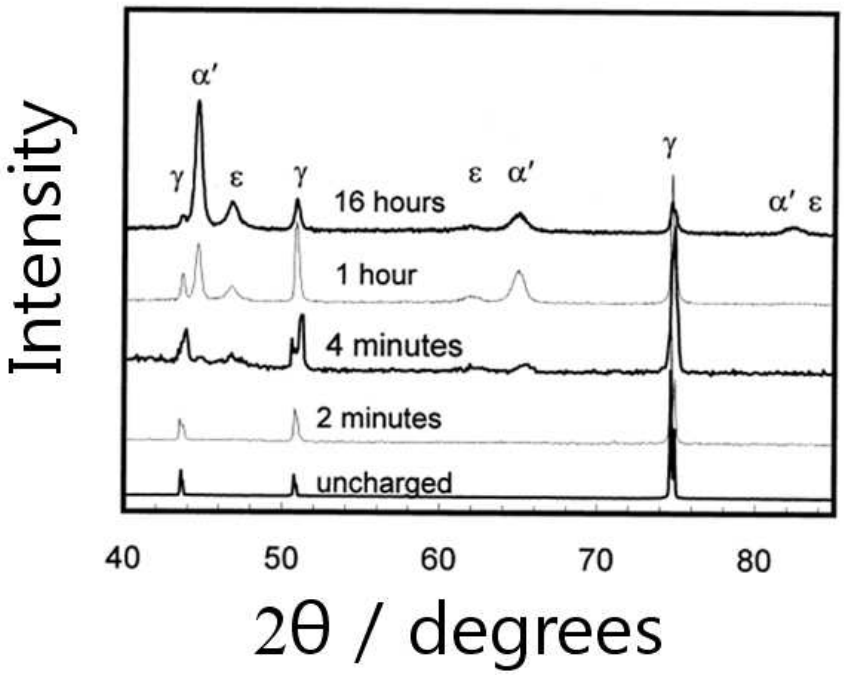

Fig. 1.19: Hydrogen-induced martensitic transformation observed with XRD spectra of the uncharged and charged specimens at 200 A m^{-2} for different charging times (Yang *et al*., 1999).

However, almost all observations of the hydrogen induced phase transformation were obtained by charging the specimens at high cathodic current density more than 200 A m^{-2} (Yang *et al.*, 1999) which results in concentrations in excess of 300 ppmw (Rozenak and Bergman, 2006). In the case of TRIP steels, only about 10 ppmw was enough for the severe mechanical degradation as indicated in the Fig. 1.17. Therefore, the effect of hydrogen-induced martensitic transformation for the mechanical degradation seems to be negligible in TRIP steels. Iyer (1987) reported that the hydrogen has no significant effect on the stability of austenite with the amount of 10-13 ppmw hydrogen. Garrison and Hyzak (1986) also showed the absence of hydrogen influence on the mechanical stability of retained austenite even though the amount of hydrogen can dramatically embrittle the steels.

1.2.4 Thermal Desorption Analysis for TRIP Steels

It has been known that the retained austenite itself provides a strong trapping site for hydrogen in multi-phase steels (Andreone and Murut, 1990; Chan *et al*., 1991) because the austenite has a greater solubility but lower diffusivity than the ferrite. Thus, the austenite increases the resistance to the hydrogen embrittlment (Park *et al*., 2002; Gu *et al*., 2002) in the TRIP steels. The hydrogen trapping sites in the TRIP steels, however, include not only the austenite but also the defects such as grain boundaries and dislocations. Thus, the hydrogen trapping behavior becomes complicated due to the deformation which not only changes the fractions of microstructural constituents but also generates defect.

There have recently been several investigations to reveal the role of retained austenite on the hydrogen trapping using TDA for multi-phase steels. The thermal desorption rate was reported to increase, where the profile consists of one large peak, due to the presence of retained austenite accommodating more hydrogen (Tsubakino *et al*., 1999; Hojo *et al.,* 2008). However, the TDS spectrum of one large curve was also increased even though the fraction of retained austenite decreased with extended deformation as shown in Fig. 1.20 (Escoba *et al.*, 2009). Actually, the distribution of hydrogen in various trap sites and thus the contribution of each trap site on the change of desorption curves was not quantitatively evaluated so far because the desorption from different trap sites such as grain boundaries, dislocation and retained austenite is overlapped in almost the same temperature interval. Therefore, the effect of deformation and consequential change of microstructure on the hydrogen behavior in the multi-phase steels is still ambiguous.

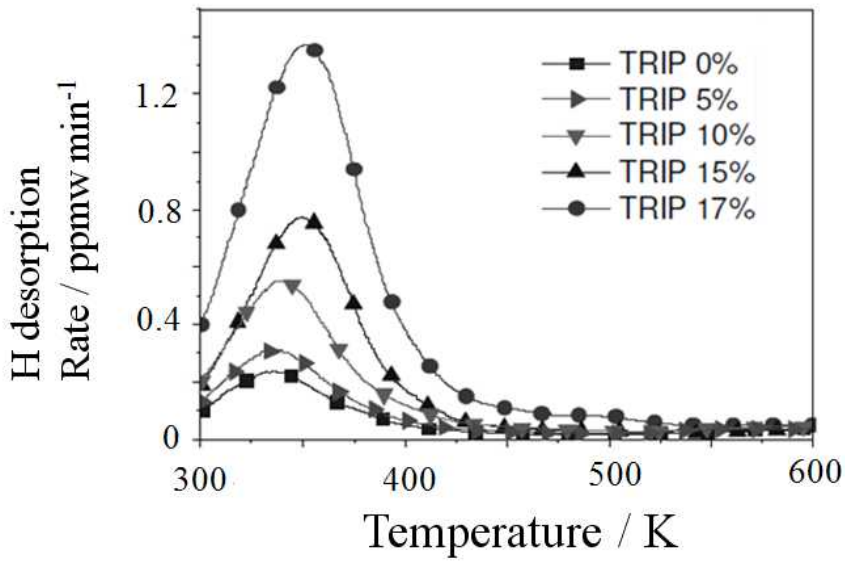

Fig. 1.20: Thermal desorption profiles of TRIP700 steel strained to different amount and then charged (Escoba *et al*., 2009).

1.3 Hydrogen Embrittlement in TWIP Steels

1.3.1 TWIP Steels

High-manganese twinning-induced plasticity (TWIP) steels are currently promising candidates for applications in the automotive industry due to their exceptional combination of strength and elongation, as shown in Fig. 1.21 (De Cooman *et al*., 2009). The metallurgical development of the relevant Fe-Mn-C system began with the work of Hadfield (1888). The austenite remains stable during deformation and some of the plastic deformation occurs by twinning, which is said to enhance elongation. Recently, industrial research has focused mainly on Fe-18Mn-0.6C (wt%) and Fe-22Mn-0.6C (wt%) TWIP steels containing more manganese and less carbon than the Hadfield steel, which may be alloyed with Al and/or Si (De Cooman *et al*., 2009).

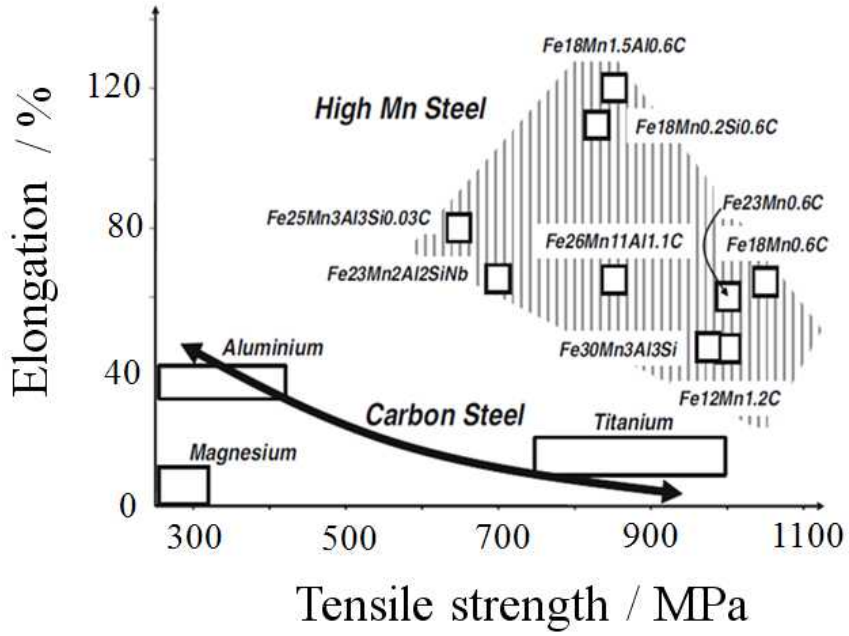

Fig. 1.21: Overview of the materials currently used in the construction of car bodies. TWIP steels have a high manganese concentration in the range of 15-30 wt%, which results in a fully austenitic microstructure (De Cooman *et al*., 2009).

The high ductility of TWIP steel is obtained as a result of its high work hardening rate (Asgari *et al*., 1997). However, the associated mechanism is still a matter of debate. Some authors attribute the hardening to dynamic strain aging mechanism for those alloys containing an appreciable amount of solute C, typically more than 0.5 wt% (Adler *et al*., 1986; Shun *et al*., 1992). The interaction between C-Mn bonds and mobile dislocations may cause the strain aging and lead to serrated flow curves (Kim *et al*., 2009). Mechanical twinning can also improve the strain hardening. This is so called the TWIP is considered to results from a dynamical Hall-Petch effect (Remy, 1978; Allain *et al*., 2004; Bouaziz *et al*., 2008; Idrissi *et al*., 2010). It is argued that the mechanical twins that contain a huge density of sessile dislocations resulting from the mechanism of twin nucleation and growth (Idrissi *et al*., 2010) play the role of planar obstacles for the dislocation glide. Bouaziz *et al.* (2008)

proposed a model describing the kinematic hardening in relation to the grain size and the twin spacing during straining for the dynamical Hall-Petch effect.

1.3.2 Effect of Hydrogen on the Stacking Fault Energy

There are three mechanisms during the austenite plastic deformation; martensite transformation, twinning and dislocation movement. The relevant parameter for the selection of mechanism is thought to be the stacking fault energy (SFE) as shown in Fig. 1.22 (Remy and Pineau, 1977). Thus, it is necessary to obtain the stacking fault energy, which depends on the temperature as well as the chemical composition, in the right region for twinning.

In austenitic structures, twinning is due to stacking faults extending in parallel adjacent closed-packed planes. If this occurs not on every plane but every two planes, then it leads to the formation of ε martensite. The stacking fault can be modelled by the two atomic layers of ε martensite on $\{111\}_\gamma$, so the SFE is given by as (Hirth, 1970)

$$\mathrm{SFE} = 2\rho\Delta G^{\gamma\to\varepsilon} + 2\sigma^{\gamma/\varepsilon} \qquad (1.19)$$

where $\Delta G^{\gamma\to\varepsilon}$ is free energy change of the transformation $\gamma \to \varepsilon$, ρ is the surface density of atoms in the $\{111\}_\gamma$ planes, and $\sigma^{\gamma/\varepsilon}$ is the interfacial energy between γ and ε. Fig. 1.23 shows the calculated SFE when adding each element to the Fe-22Mn-0.6C (wt%) steel (Dumay *et al*., 2008).

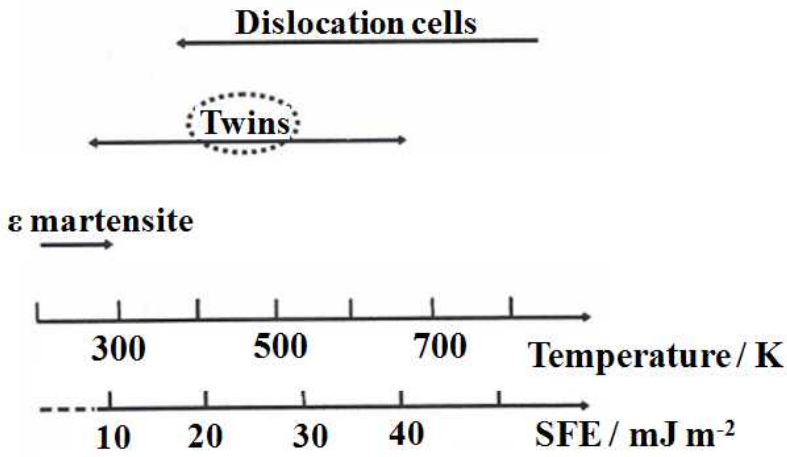

Fig. 1.22: Effects of temperature and stacking fault energy (SFE) on the deformation mechanism in Fe-20Mn-4Cr-0.5C (wt%) steels (Remy and Pineau, 1977).

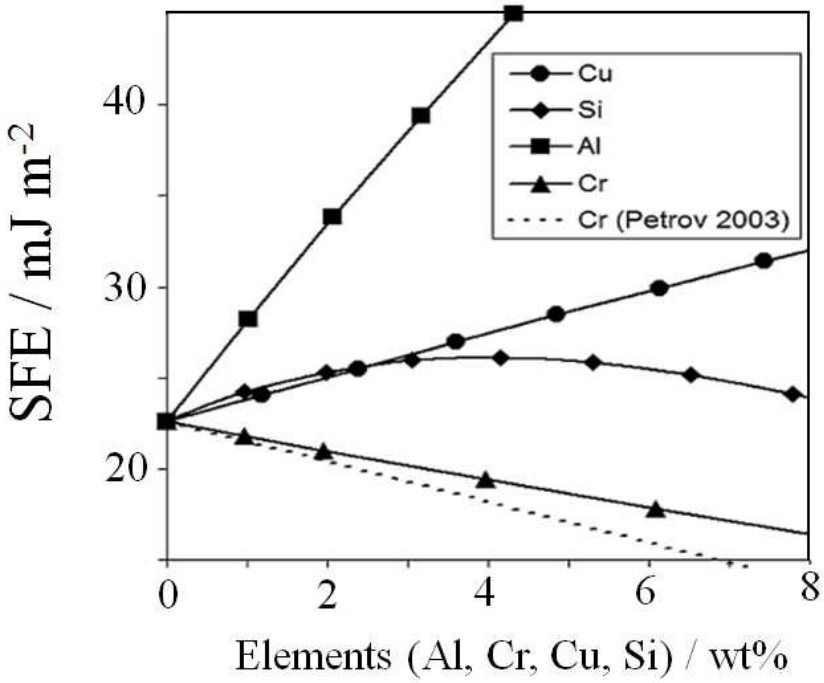

Fig. 1.23: Predicted influence of alloying elements on the SFE of the Fe-22Mn-0.6C (wt%) reference (Dumay *et al*., 2008).

Many experimental results showed the hydrogen induced phase transformation of austenite to ε martensite by cathodic hydrogen charging in unstable austenitic stainless steels (Rigsbee, 1977; Yang and Luo, 2000), stable austenitic stainless steels (Narita *et al*., 1982; Minkovitz and Eliezer, 1982) and Fe-21Mn (wt%) alloy (Aikawa *et al*., 1993). This phenomenon is interpreted on the assumption that the hydrogen lowers the SFE of austenite and the high stress gradients resultant from the forced hydrogen absorption would produce the martensite at room temperature. Whiteman and Troiano (1964) reported the reduction of SFE caused by hydrogen with the measurement of TEM in 310 stainless steel. Pontini and Hermida (1997) measured by XRD the reduction of 37 % of SFE in the presence of 274 ppmw hydrogen at room temperature for 304 stainless steel.

One possibility for the reduction of SFE is the formation of H-H pairs proposed by More *et al*. (1998). The phenomenon can be interpreted as an energetically convenient response of the system generating a larger faulted zone to favour spontaneous H-H pairs formation by chemical reaction. During faulting, it was shown that the H-H pair formation is more likely to occur along directions connecting octahedral interstices of the HCP stacking sequence and that are normal to the {111} planes as shown in Fig. 1.24 (Hermida and Roviglione, 1998), decreasing the total energy. Thus the stacking faults also can act as the hydrogen traps.

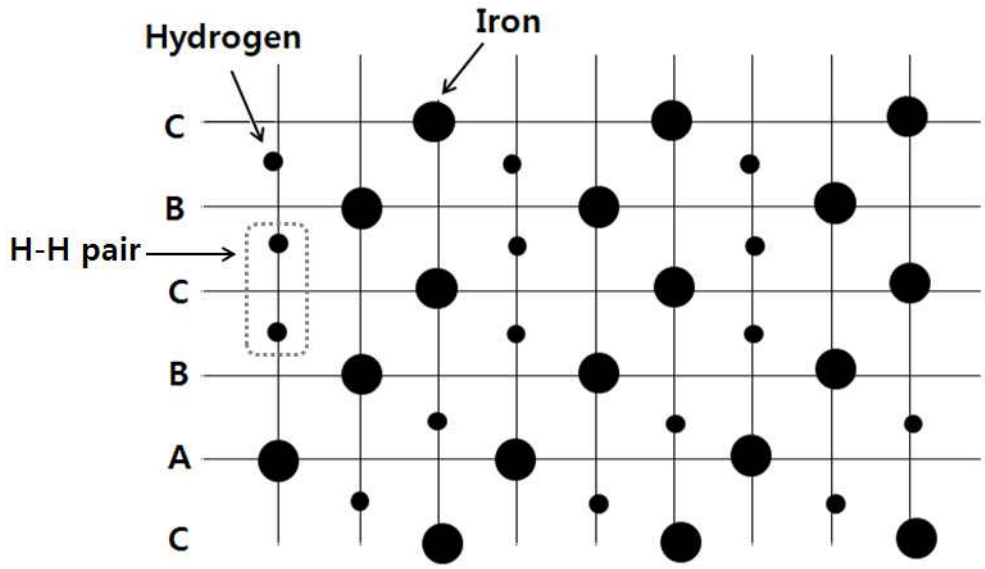

Fig. 1.24: H-H pair formation at faulted zone when the all octahedral interstitial sites are occupied with the hydrogen in austenite (Hermida and Roviglione, 1998).

1.3.3 Delayed Fracture

The high manganese TWIP steels have yet to be commercialised because some of them may be prone to delayed fracture after forming, which attributes to hydrogen embrittlement (Chun *et al*., 2012). Chin *et al*. (2011) reported that the delayed fracture occurred after cup-forming and subsequent exposure in air for 7 days even though the specimen was not cracked or fractured during the forming of Fe–22Mn–0.6C (wt%) TWIP steel. However, in the Fe-18Mn-1.2Al-0.6C (wt%) TWIP steel, the cracking did not occur regardless of the exposed times to the air. Although the delayed fracture can be avoided by adding the Al as also shown in Fig. 1.25 (Kim *et al*., 2008), the prevention mechanism has not been revealed.

There are several investigations about the hydrogen embrittlment in TWIP steels (Ronevich *et al*., 2010; Jung *et al*., 2008; So *et al*., 2009; Mittal *et al*., 1994). However, the observed mechanical degradation by tensile testing after pre-charging with hydrogen was negligible. Recently, only Koyama *et al*. (2011) showed the

clear deterioration of tensile properties for Fe-18Mn-0.6C (wt%) TWIP steels strained during the charging as shown in Fig. 1.26.

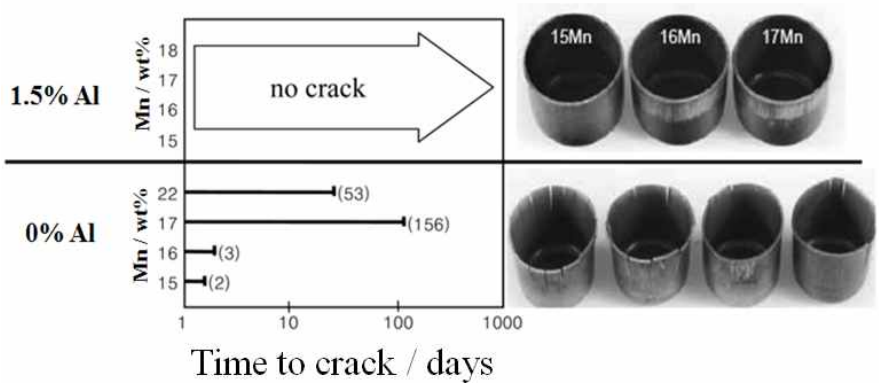

Fig. 1.25 Delayed fracture after cup deformation in TWIP steels (Kim *et al*., 2008).

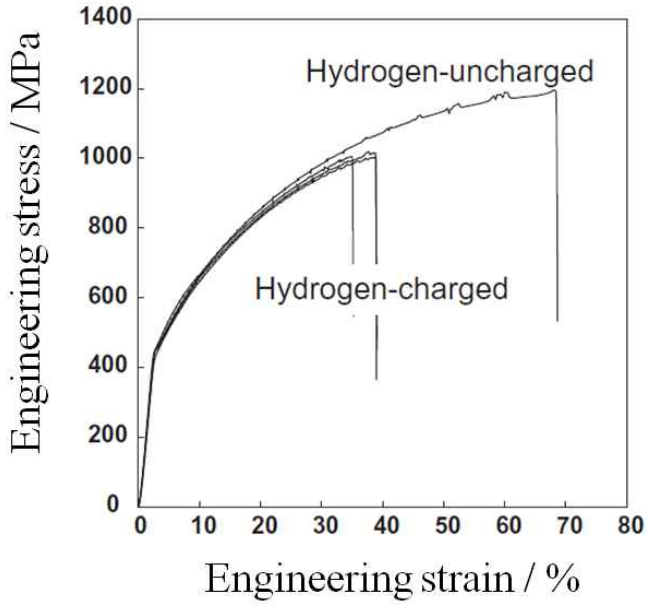

Fig. 1.26: Engineering stress–strain curves of hydrogen-charged and uncharged Fe-18Mn-0.6C (wt%) TWIP steels (Koyama *et al*., 2011).

Chapter 2: Strain Partitioning & Mechanical Stability of Retained Austenite

2.1 Introduction

Many modern steels rely on a microstructure containing some retained austenite which transforms into martensite during the course of deformation (Jacques, 2004; De Cooman, 2004). This stress or strain-induced transformation leads to additional plasticity which enables strong steels to be formed into complex shapes. Critical in this behaviour is the mechanical stability of the austenite; if transformation is exhausted at small plastic strains then the protection against a necking instability is lost, and if the austenite is too stable then it does not contribute to strain hardening at stress concentrations.

On the other hand, it is well known that martensitic transformation also increases the susceptibility to hydrogen embrittlement (McCoy and Gerberich, 1973). It is because brittle martensite can be susceptible microstructure in the context of hydrogen embrittlement (Hirth, 1980) and has a high hydrogen diffusivity permitting hydrogen-assisted continuous crack propagation (Xiukui *et al*, 1989; Mine *et al*., 2009). Thus the mechanical stability of austenite is often indicated as a critical factor for the hydrogen embrittlement in TRIP steels (Ronevich *et al.,* 2010, Jung *et al.*, 2008).

The stability of retained austenite, which is important not only for the transformation induced plasticity but also for the hydrogen embrittlement, is well understood and the chemical composition (Le-Houillier *et al*., 1972; Syn *et al*., 1978; Duchateau and Guttmann, 1981; Takahashi and Bhadeshia, 1991; Tomita and Okawa, 1993), size (Bai *et al*., 1998) and shape (Bhadeshia and Edmonds, 1983) of the austenite are the main factors. In most cases, TRIP steels are only partly austenitic because this phase is retained without using expensive solutes by ensuring that the carbon that is partitioned into the parent phase during the course of the bainite transformation does not precipitate as cementite (Jacques, 2004; De Cooman,

2004). The austenite therefore occurs in mixed microstructures where the majority phase is the mechanically softer allotriomorphic ferrite. During deformation, it is the softer phase which yields first and after appropriate work hardening, sufficient stress is transferred onto the harder regions to cause them to yield (Tomota *et al*., 1976). The distribution of plastic strains is therefore nonuniform (Furnémont *et al*., 2004). In the present work we demonstrate that the heterogeneous distribution of plastic strain is an important factor in determining the mechanical stability of the retained austenite.

2.2 Experimental

The experimental plan was to characterise in situ, the partitioning of plastic strain in two microstructures with similar retained austenite characteristics, but which in macroscopic tensile tests have exhibited quite different martensitic transformation behaviour as a function of strain, Fig. 2.1 (Suh *et al*., 2010). These two samples are made of aluminium-containing TRIP steels (Suh *et al*., 2010), with chemical compositions (wt %) and designations as shown in Table 2.1.

Two alloys were prepared as described in the literature (Suh *et al*., 2010). Vacuum-melted ingots were hot-rolled to 4.5 ㎜ thick with a finishing temperature above 800 ℃. After removing surface scale, the hot-rolled sheets were cold-rolled to 1 ㎜ in thickness. Both alloys, after heating to 720 ℃ (L–Al) and 780 ℃ (H–Al) for two minutes contained a volume fraction 0.3 of retained austenite on cooling to ambient temperature at 10 ℃ S^{-1}. The martensite-start temperature (M_s) of the retained austenite was determined by monitoring the austenite fraction with X-ray diffraction analysis at temperature interval between ambient temperature and liquid nitrogen temperature using an atmosphere control chamber. A field emission scanning electron microscope equipped with electron back scatter diffraction and an in situ tensile test attachment was used for the experiments. Tensile test specimens with a gauge length of 15 ㎜ and width 4 ㎜ were mechanically polished with colloidal silica in the final stage. Four square dots of amorphous carbon were

deposited using a focused ion beam facility in rectangle $2 \times 2 \times 0.5$ μm to mark the region observed in the scanning electron microscope during tensile testing. The step size for EBSD measurements was 70 nm and tension was applied using a crosshead speed of $5\,\mu m\,s^{-1}$, with images captured every 100 μm of displacement. The strain distribution on the marked area in the scanning microscope images was analysed using ARAMIS software which uses digital image correlation.

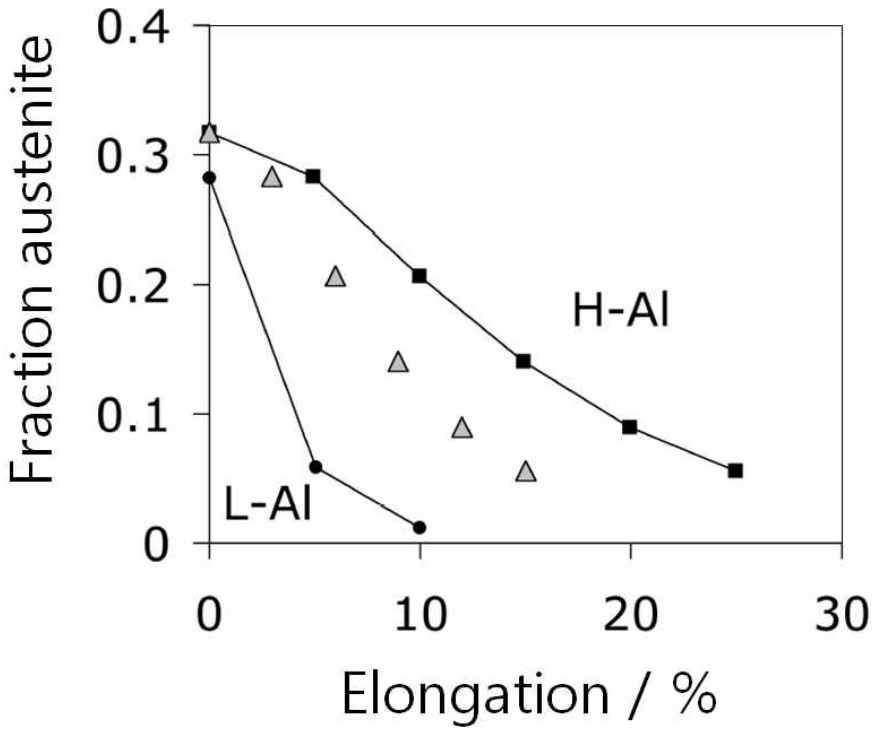

Fig. 2.1: Showing a remarkable difference in the mechanical stability of the austenite even though the chemical composition and size of the retained austenite have been verified to be similar (Suh *et al*., 2010). The triangular points are discussed later in the text.

Table 2.1: Chemical composition of samples in wt %

	C	Mn	Si	Al
L-Al	0.12	4.6	0.55	1.1
H-Al	0.12	5.8	0.47	3.1

2.3 Results and Discussion

Fig. 2.2(a) and (b) show the phase maps for the two alloys. The important point to note is that the L-Al microstructure contains a uniform dispersion of ferrite and austenite, whereas that of H-Al has a bimodal size-distribution of ferrite grains, some of which are very coarse. Fig. 2.2(c) shows data from X-ray measurements done as a function of sub-zero temperatures. The two samples have similar martensite-start temperatures in the vicinity of -120 °C with a maximum difference of about 30 °C due to the slightly higher manganese concentration in H-Al. The similar M_s temperatures are expected since the austenite has comparable composition and size (Suh *et al*., 2010).

Fig.2.3 shows SEM images of mechanically polished surfaces with carbon markers for the L-Al and H-Al alloys during straining. The blue rectangle stands for analyzed area for strain distribution, which is the same one appearing in the phase mapping in Fig. 2.2. The analyzed area was selected to have similar fraction of austenite with a macroscopic scale. The evolution of strain in the selected regions of alloys by the digital image correlation is shown in Fig. 2.4. The maximum, minimum and mean microstrains are recorded as a function of the elongation of the tensile sample. The local response of the alloys to the tensile elongation is quite different. For example, the difference between the minimum and maximum microstrain is evaluated to be 4.8% at the tensile elongation of 13% in the L-Al alloy, but the difference in the H-Al alloy is 16.3 %, getting larger as the tensile elongation increases. It means that the strain is more partitioned into certain microsturctural constituents during the deformation of H-Al alloy. Fig 2.5 shows the

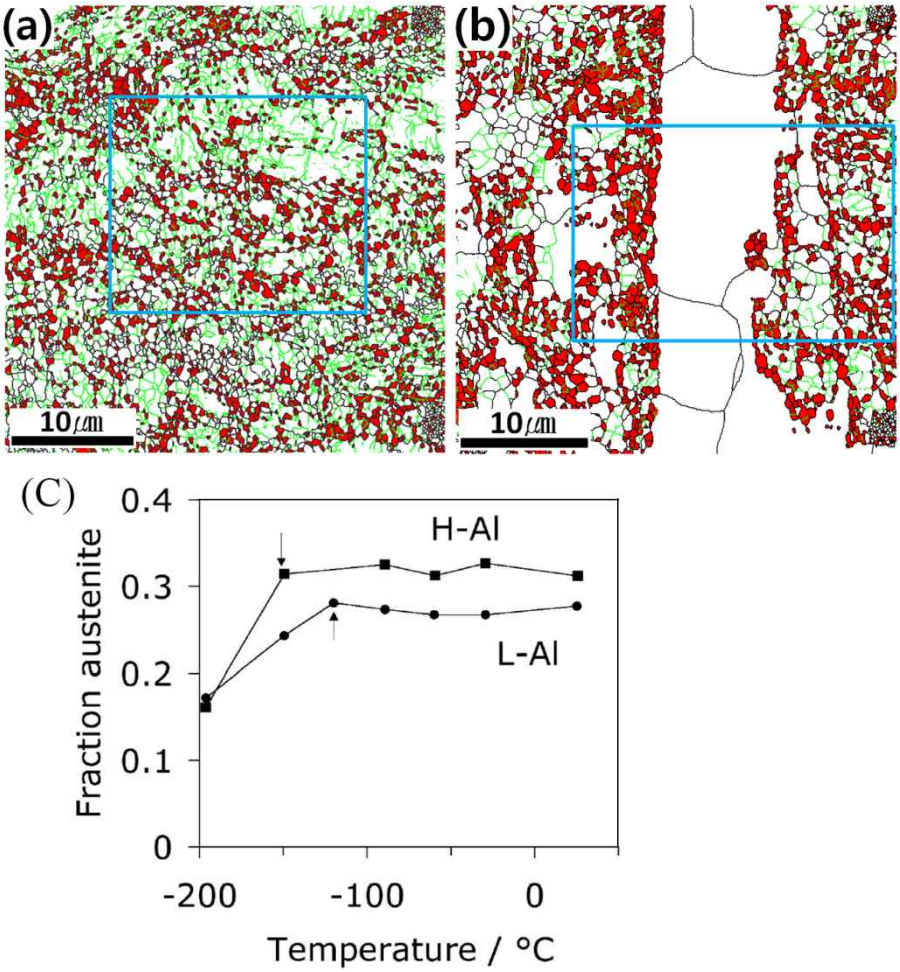

Fig. 2.2: EBSD phase mappings in which austenite is red and the rectangles indicate the areas designated for strain analysis. Crystallographic misorientations in the range 2-15° are marked by green boundaries and larger deviations by black interfaces; (a) L-Al, (b) H-Al. (c) Thermal stability of the retained austenite. The arrows mark the onset of martensitic transformation.

distributions of local strain at the tensile elongation of 4.9 % and 9.6 % for L-Al alloy, and of 12.8 % and 19.1 % for H-Al alloy, respectively. It is clear that the distribution of strain is much more heterogeneous in H–Al. Comparison of local

strain distributions with the EBSD mapping in the Fig. 2.2(b) reveals that the highest strains are located in the coarse ferrite, but the local strain in the austenite is much lower than the mean strain. In other words, the apparent large mechanical stability of the austenite as illustrated in Fig. 1 is a reflection of the fact that the austenite experiences less deformation than the average elongation recorded on the tensile specimen.

These results could at least partly explain why steel-specific (Sugimoto *et al*., 1992), or even generic theory (Sherif *et al*., 2004), for the mechanical stability of austenite is not able to explain the experimental data on TRIP-assisted steels to an accuracy of better than ±0.05 volume fraction of austenite; this is a large discrepancy given that the fraction of retained austenite is of the order of 0.15. Such theories test experimental data based on the assumption that the plastic strain experience by the austenite is identical to the overall elongation of a tensile–test specimen.

Judging from the data in Fig. 2.4(b), the strain experienced by the austenite is a factor of 0.6 less than the overall elongation. Assuming that this is representative of all the austenite present in the H-Al steel, the triangular points in Fig. 1 represent the fraction of austenite as a function of the strain in austenite. It is seen that the discrepancy in the mechanical stabilities of austenite in H-Al and L-Al is substantially reduced when a comparison is made using the strain in austenite. We have made the reasonable assumption in this comparison that the distribution of strain in L-Al is homogeneous.

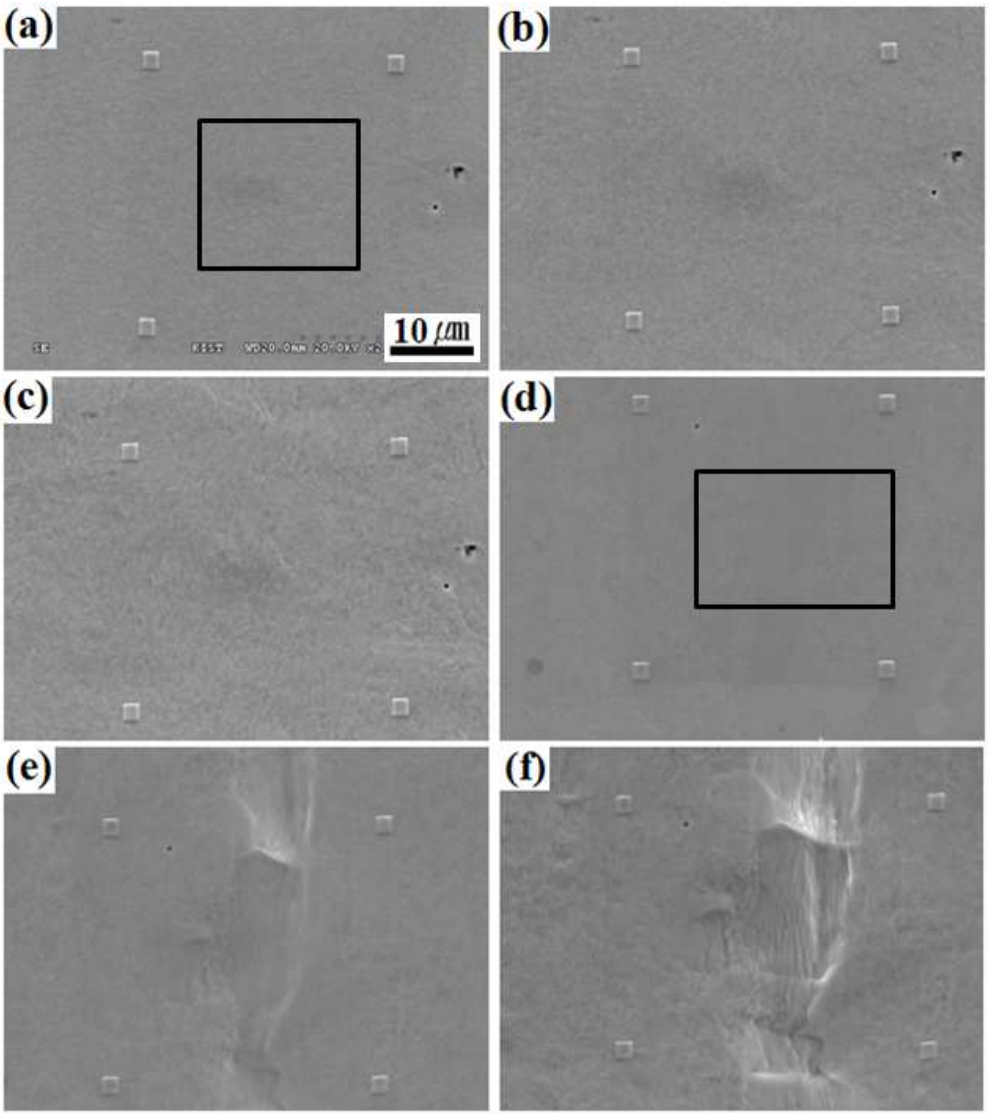

Fig. 2.3: Scanning electron microscope images showing the locations of strain analysis at a tensile elongation of 0 % (a), 4.9 % (b) and 9.6 % (c) in sample L–Al, and at a tensile elongation of 0 % (d), 12.8 % (e) and 19.1 % (f) in sample H–Al. The carbon markers are evident at the corners of the images.

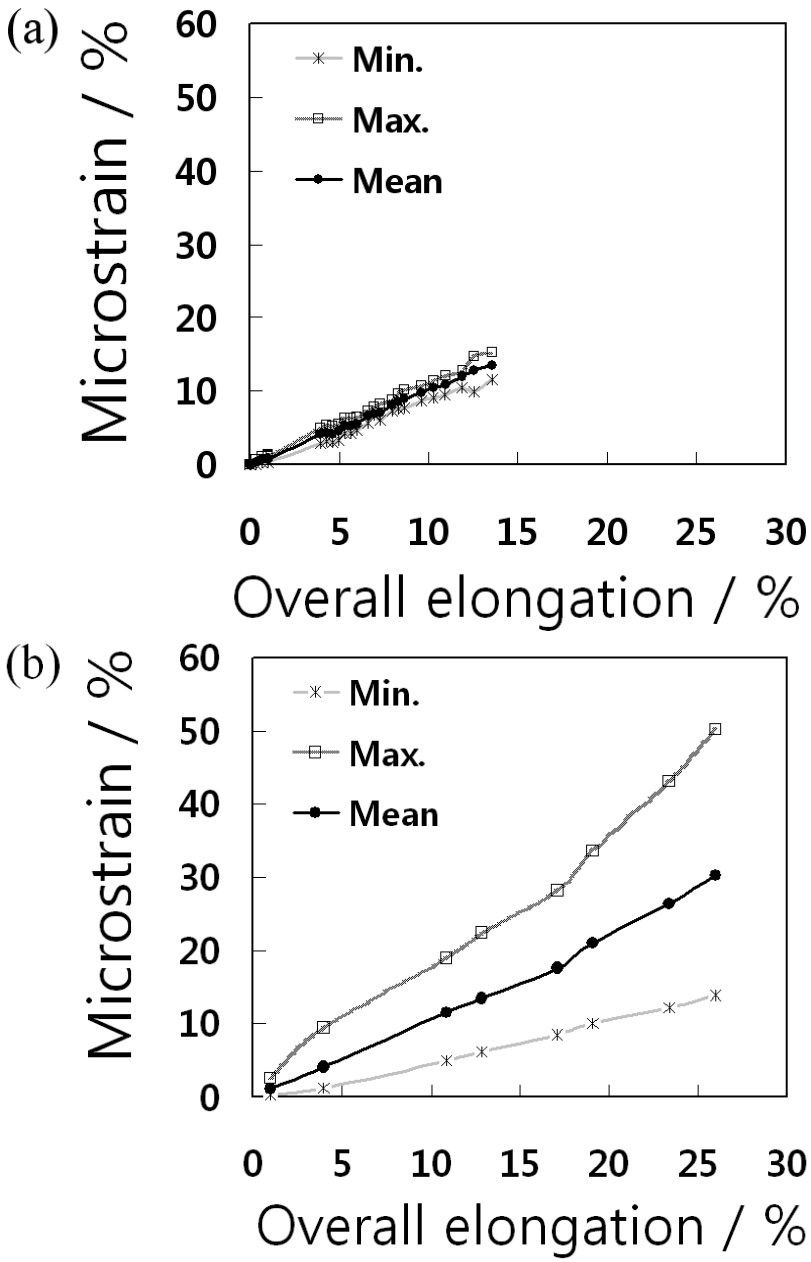

Fig. 2.4: The maximum, minimum and mean microstrains recorded as a function of the elongation of the tensile sample, for samples L-Al (a) and H-Al (b).

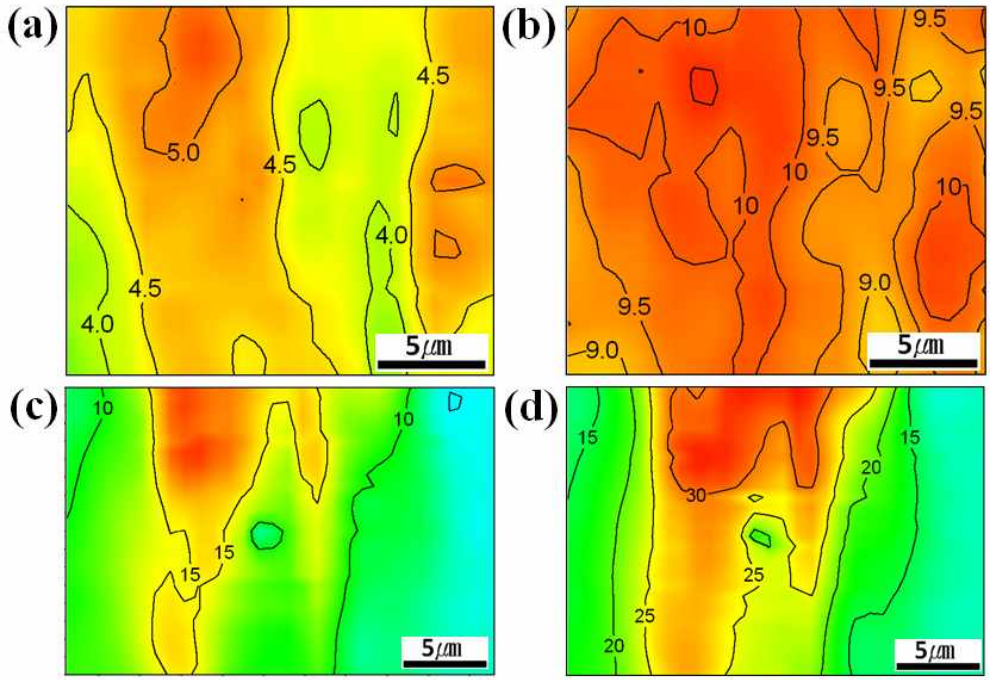

Fig. 2.5: The strain map at a tensile elongation of 4.9 % (a) and 9.6 % (b) in sample L-Al, and the corresponding map at a tensile elongation of 12.8 % (c) and 19.1 % (d) in sample H-Al.

2.4 Summary

The mechanically harder phase, the retained austenite, experiences less deformation than the average elongation recorded on the tensile specimen because the softer phase, the allotriomorphic ferrite, covers considerable part of apparent deformation. Thus, it appears that the partitioning of strain between the different phases present in TRIP-assisted steels can lead to a misleading impression of the mechanical stability of retained austenite when comparisons are made between steels with substantially different microstructures, or when attempts are made to explain the stability in terms of chemical composition alone.

Chapter 3: Effect of Deformation on Hydrogen Trapping and Effusion in TRIP-Assisted Steel

3.1 Introduction

Hydrogen is legendary in its ability to harm the toughness of steels (Oriani and Josephic, 1974; Hirth, 1980) and its role in static failure, i.e., unexpected failure after a component has been in service for a period well below its design life (Kushida *et al*., 1996). Resistance to hydrogen-induced static fracture now is a basic acceptance criterion in the exploitation of TWIP steels (So *et al*., 2009), strong automotive-steels (Loidl *et al*., 2011; Kim *et al*., 2007) and is a suspect in the occurrence of early failures in large bearings for wind turbines (Bhadeshia, 2012).

TRIP-assisted steels consist predominantly of allotriomorphic ferrite with 15-30 % of carbon-enriched retained austenite; the latter can undergo martensitic transformation during the course of plastic deformation. Of all the steels susceptible to embrittlement, the role of hydrogen in the TRIP steels is particularly unclear (Loidl *et al*., 2011) because the deformation mechanism involves displacive transformation which not only leads to changes in the fractions of microstructural constituents, but also generates defects which are potential hydrogen trapping sites. Any hydrogen inherited by the martensite will have quite different solubility and diffusivity when compared with the parent austenite.

Thermal desorption spectroscopy (TDS) is commonly used to follow the evolution of hydrogen from a variety of sources within the steel as the sample is heated at a constant rate. Hydrogen atoms which are more strongly bound to traps evolve at higher temperatures so that the resulting spectrum can be interpreted to reveal information about the sources. Previous work on hydrogen-charged TRIP-assisted steels has largely involved qualitative interpretations of TDS spectra (Tsubakino *et al*., 1999; Hojo *et al*., 2009; Escoba *et al*., 2009). The present work is an investigation of the release of hydrogen from TRIP-assisted steels, both experimentally using TDS and with a theoretical interpretation which permits the

desorption spectrum to be predicted as a function of deformation, phase transformation and heating rate.

3.2 Experimental

3.2.1 Alloys

Table 3.1 lists the chemical compositions of two alloys, L-Al and H-Al, which are TRIP-assisted steels when appropriately heat treated. Vacuum induction-melted ingots of dimensions 300 × 150 × 50 mm were reheated at 1200 ℃ for 2 h and hot-rolled to 4.5 mm in thickness with finishing temperature above 800 ℃ followed by air cooling to room temperature. The alloys were cold-rolled to 1 mm in thickness after pickling in a 10 % HCl solution and then intercritically annealed using an infrared furnace at 720 (L-Al) and 780 ℃ (H-Al) respectively for 2 min. The heating and cooling rates were 10 ℃ s^{-1}. This gives both alloys a comparable retained austenite content, albeit of different mechanical stabilities (Suh *et al*., 2010). A third treatment, H-Al 900, involved annealing to 900 ℃ in order to produce a structure without retained austenite; the detailed microstructures and mechanical properties have been presented elsewhere (Suh *et al*., 2010).

Table 3.1: Chemical composition of samples in wt %

	C	Mn	Si	Al
L-Al	0.12	4.6	0.55	1.1
H-Al	0.12	5.8	0.47	3.1

3.2.2 Microstructural Characterisation

The microstructure was observed using a field emission gun scanning electron microscope (FE-SEM) equipped with an electron back-scattered diffraction (EBSD) facility. In the latter case the specimens were finally mechanically polished with a colloidal silica suspension and the step size was 0.07 μm. The retained austenite

was determined using X-ray diffraction with CuK_α radiation; the samples in that case were finally chemically polished in a 5 % HF + H_2O_2 solution. Integrated intensities of 110_α, 200_α, 211_α, 220_α, and 111_γ, 200_γ, 220_γ, 311_γ reflections were used for the quantitative phase fraction measurements (Jatczak, 1980). The focused ion beam was used in preparing a specimen for transmission electron microscopy to observe the microstructure around the micro-crack causing the mechanical degradation.

3.2.3 Hydrogen Charging and Thermal Desorption

Tensile test coupons with a 32 mm parallel length, 6 mm width and 1 mm thickness were prepared according to the ASTM E8M, polished with the 800 SiC grit papers and charged electrochemically with the hydrogen for periods between 1-72 h in an aqueous mixture of 3 % NaCl + 0.3 % NH_4SCN at 0.5 A m^{-2}. Charging for 72 h was found sufficient to saturate the samples. Thermal desorption spectroscopy with gas chromatography was conducted at constant heating rates of 100-300 ℃ h^{-1} to a maximum temperature of 500 ℃. The parallel length part of each charged-tensile sample was cut immediately after charging and placed in the TDS furnace. The sample gas was analysed at 5 min intervals using helium as a carrier gas and the desorption rate was defined as the amount of hydrogen evolved in 1min per gram of the specimen. A standard mixture He + 10.2 volume ppm of H_2 was used for the calibration.

The hydrogen contents of the tensile specimens were evaluated with a duplicated sample prepared under the same condition. Hydrogen contents in tensile specimens were controlled by adjusting the current from 0.1 to 30 A m^{-2} in either 3 % NaCl + 0.3 % NH_4SCN or 0.1 N NaOH aqueous solutions. However, the charging time of 72 h was kept for the steady state distribution of hydrogen. It is noteworthy that hydrogen-induced surface damage or cracking was not observed even after charging at the highest current density of 30 A m^{-2}.

3.2.4 Mechanical Tests

Slow strain rate tensile tests were conducted on the specimens charged with hydrogen at a constant crosshead speed of 0.015 mm min^{-1}, corresponding to a nominal strain rate of 10^{-5} s^{-1}. A faster strain rate of 10^{-2} s^{-1} was used to examine the dynamic transition of trapping sites during deformation.

3.3 Results and Discussion

3.3.1 Microstructure

Fig. 3.1 illustrates representative microstructures; the austenite fractions in L-Al and H-Al are 0.26 and 0.30 respectively. L-Al alloys contains recovered ferrite with low-misorientation boundaries, H-Al has a fully recrystallised structure. The coarse ferrite grains in H-Al originate from its large Al content, which results in an expanded two-phase region of ferrite and austenite at the hot-rolling temperature. Fig. 3.1c confirms that the H-Al 900 specimen has a negligible retained austenite content because of the higher annealing temperature of 900 ℃.

As will be discussed later, the mechanical stability of retained austenite is related to the degradation of mechanical properties by hydrogen in these multiphase steels. The mechanical stability in terms of the decrease in austenite content as a function of plastic strain, is illustrated by the solid symbols in Fig. 3.2. The austenite in H-Al is significantly more stable than that in L-Al; the reasons for this are described in chapter 2 but the apparent stability depends on the austenite composition, grain size and the partitioning of strain between the phases during the course of deformation.

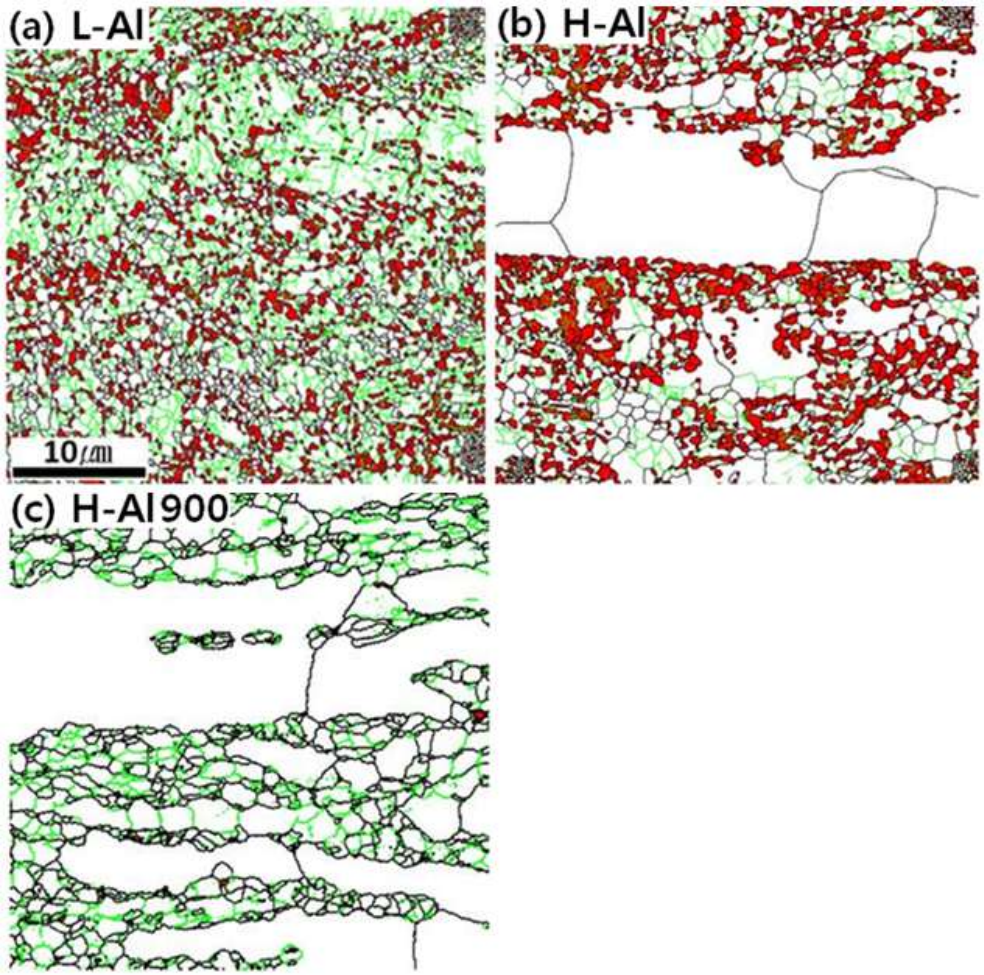

Fig. 3.1: EBSD phase mappings of (a) L-Al, (b) H-Al and (c) H-Al 900 in which ferrite and austenite is represented by white and red, respectively. Green lines indicate low-misorientation (2-15°) boundaries whereas black lines represent high-misorientation boundaries.

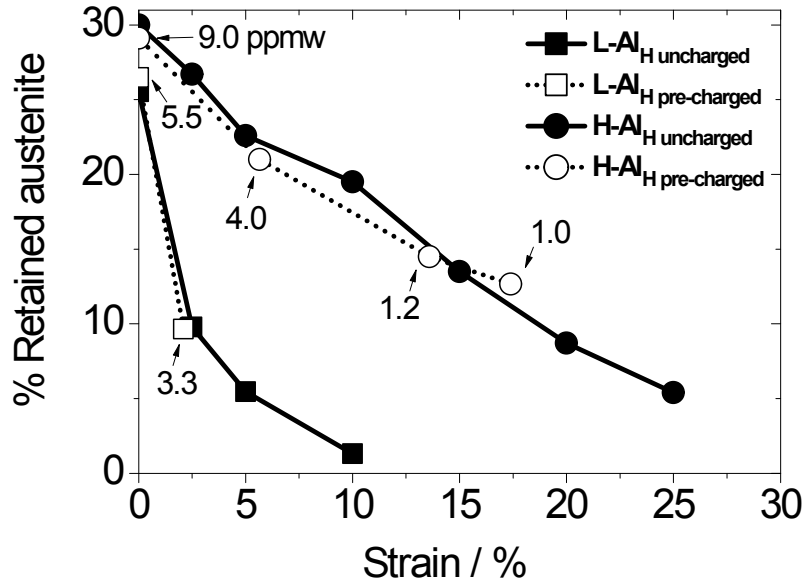

Fig. 3.2: Solid symbols show the mechanical stability of austenite in samples H-Al and L-Al. The open symbols are discussed later in the paper, to illustrate that the mechanical stability of the retained austenite in the alloys studied does not depend on the hydrogen concentration.

3.3.2 Hydrogen Effusion

Fig. 3.3 shows the TDS spectra for samples hydrogen-charged using a current density of 0.5A m^{-2}; the desorption rate increases with the charging time, but hardly changes beyond a charging time of 60 h for L-Al and H-Al and 12 h for H-Al 900. The temperature of maximum desorption rate (T_p) is mostly less than 100 ℃, suggesting the release of hydrogen from reversible trap sites (Pressouyre and Bernstein, 1978). Since the desorption profiles and T_p do not change after prolonged charging, it is assumed for those cases that a steady state distribution of hydrogen is established within the specimens.

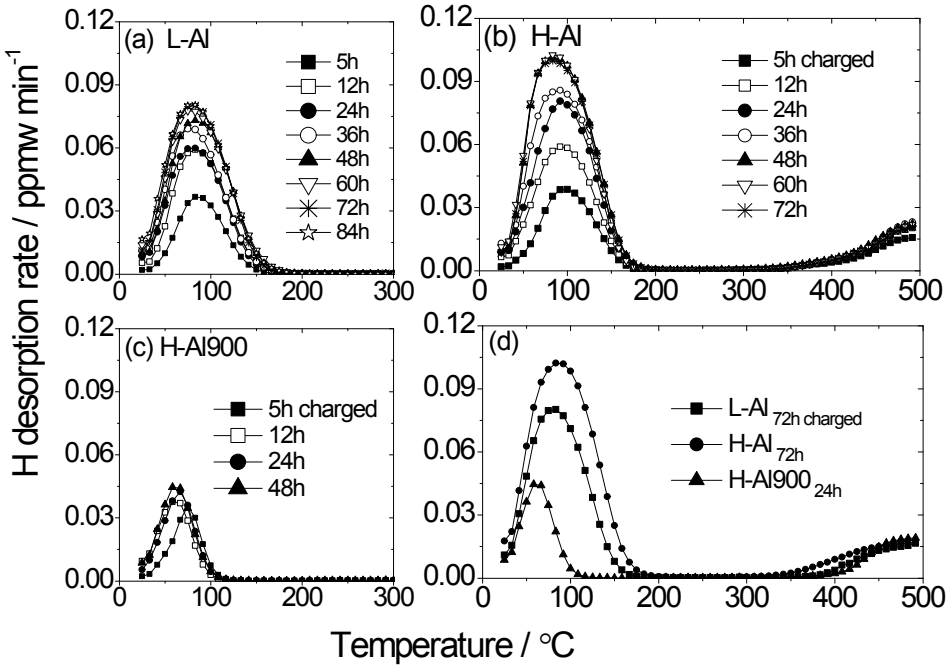

Fig. 3.3: Thermal desorption profiles of (a) L-Al, (b) H-Al and (c) H-Al 900 as a function of hydrogen charging time. (d) Comparison of desorption profiles for samples charged to saturation.

Fig. 3.3b,d indicate another desorption peak above 400 ℃ for all the specimen, irrespective of the charging condition or the amount of retained austenite. The trapping there is regarded to be irreversible and not considered in the present study because such hydrogen does not lead to a deterioration of mechanical properties (Takai and Watanuki, 2003). Fig. 3.4a confirms that the diffusible hydrogen content is almost constant after 60 h of hydrogen charging for L-Al and H-Al alloys and 12 h for H-Al 900. The faster saturation of H-Al 900 specimen than L-Al or H-Al alloys is attributed to the absence of retained austenite, for two reasons, that the diffusivity of hydrogen at 323 K in ferrite is 3-4 orders of magnitude greater than in austenite (Murakami *et al*., 2008) and the secondly hydrogen is 10 times more soluble in austenite than in ferrite (Kiuchi and McLellan, 1983). This is consistent also with the greater saturation hydrogen contents (4 and 5.4 ppmw in L-Al and H-Al respectively) of the samples containing retained austenite. One discrepancy is that the austenite fraction in H-Al alloy is greater by 15 % but the saturation hydrogen is higher by 35 %; it is suggested that this is because the fine recrystallised grains in H-Al with their large misorientation boundaries provide additional trapping sites (Martinez-Madrid *et al*., 1985).

The interpretation of the data described above is difficult, given the multiphase character of the samples. To separate the desorption from austenite, samples of L-Al and H-Al were charged to saturation at 1A m^{-2} for 72 h, then aged at ambient temperature for 168 h in order to allow any diffusible hydrogen with the non-austenitic regions to escape; calculations based on $\sqrt{6Dt}$ using a published diffusion coefficient D for hydrogen in ferrite (Kiuchi and McLellan, 1983) over t = 168 h indicate a diffusion distance in excess of 360 mm, far greater than the 0.5 mm half-thickness of the sheet samples studied. This assessment was confirmed by the fact the mobile hydrogen in H-Al 900 completely diffused out within 24 h of ageing at ambient temperature, Fig. 3.4b.

(a)

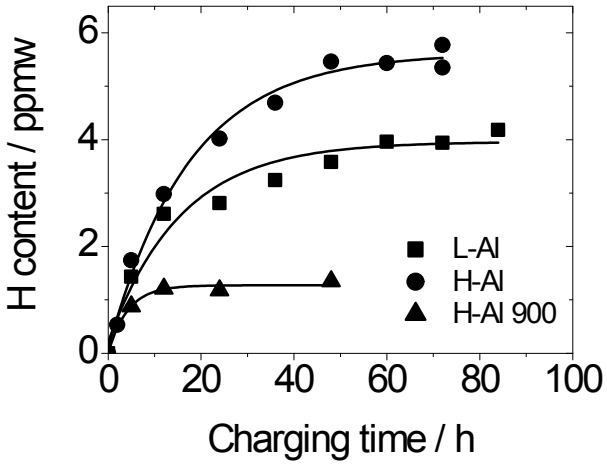

(b)

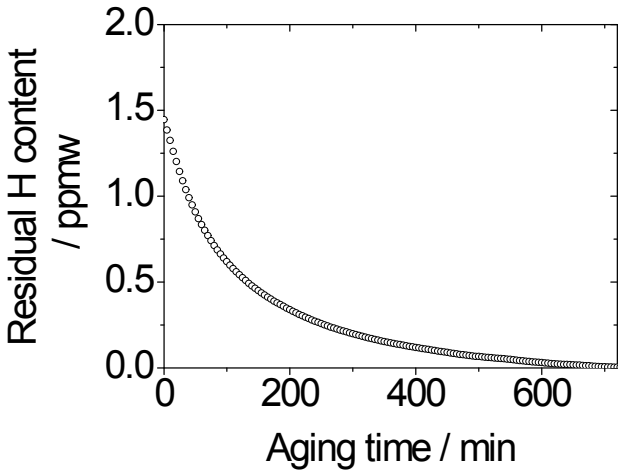

Fig. 3.4: (a) Total diffusible hydrogen content as a function of charging time. (b) Mobile hydrogen in H-Al 900 is completely removed in less than 24 h of ageing at ambient temperature.

Fig. 3.5 shows the results from the charged and aged samples. To analyse the TDS spectra for activation energy, Fick's first law of diffusion was applied in a stepwise manner to calculate the flux J^H emerging from each broad surface of the

steel sheet:

$$J^H = -D_0 \exp\left(-\frac{E_a}{RT}\right) \times \frac{C^H - C_e^H}{x} \quad (3.1)$$

where C^H is the concentration of hydrogen within the steel, C_e^H is that outside the steel, taken to be zero, and x is a distance which determines the gradient of concentration. D_0 and E_a are the pre-exponential term and activation energy respectively, of an effective diffusion coefficient. Two factors need to be taken into account in applying this equation, the first that TDS analysis involves continuous heating, and the second that the composition within the steel changes as the hydrogen effuses out. The calculation was therefore done in 1 ℃ steps, with a modification of T and C^H at each step, in the latter case correcting the concentration within the steel to account for the hydrogen that had escaped.

When considering the escape of hydrogen from austenite into the environment of the TDS equipment, it is necessary to account for the fact that the austenite is not continuous through the steel but is present as clusters of grains. It can, however, be assumed that the controlling feature is the concentration gradient within the austenite since any hydrogen that leaves the austenite can diffuse much more rapidly through the ferrite. It is reasonable then to set x as a measure of the size of the austenite regions. To analyse the data, the diffusion coefficient used was that measured for austenite using independent permeability experiments, i.e., D_0 = 7 × 10^{-7} m^2 s^{-1} and E_a = 48 kJ mol^{-1}, (Xiukui *et al*., 1989).

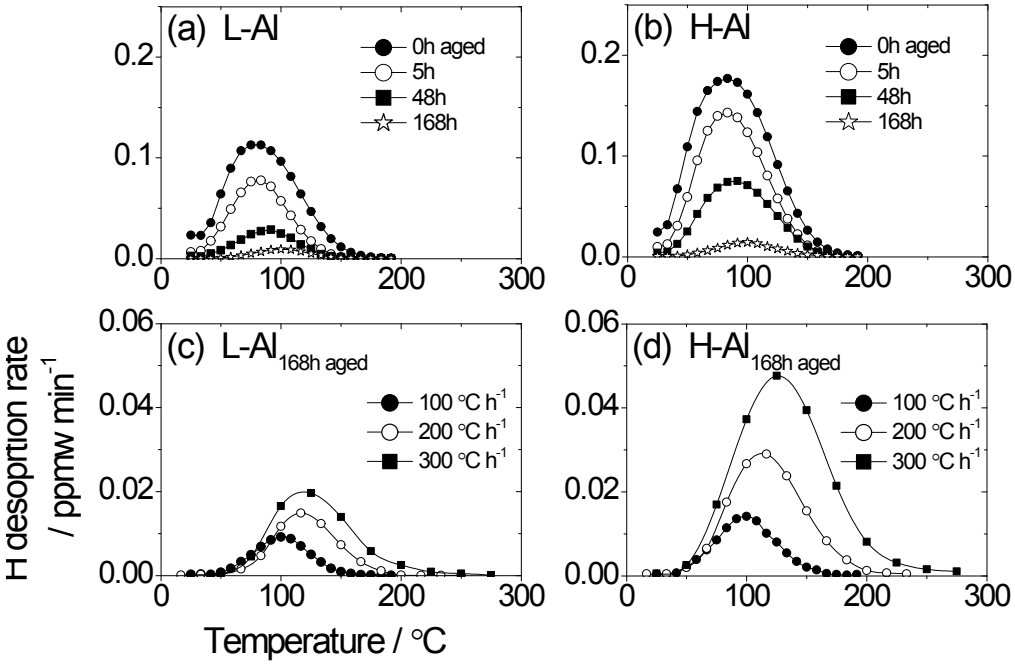

Fig. 3.5: A comparison of (a,b) hydrogen charged, against (c,d) charged and aged samples as a function of the heating rate. Note that the vertical scale for (c,d) is magnified relative to (a,b).

The analysis using the stepwise application of Eq. 3.1 was then applied to the charged and aged data for 100 °C h^{-1}, allowing x to be a fitting parameter. The distance x was in this way determined to be 12 μm, which is not an unreasonable value considering the size of the clusters of austenite grains in Fig. 3.1. Using this value of x, and without changing any other parameter, predictions were made for the heating rates 200 and 300 °C h^{-1}. The results are illustrated in Fig. 3.6a,b and the predictions of the unfitted higher heating rate data are gratifying, although with some discrepancies at the highest of temperatures.

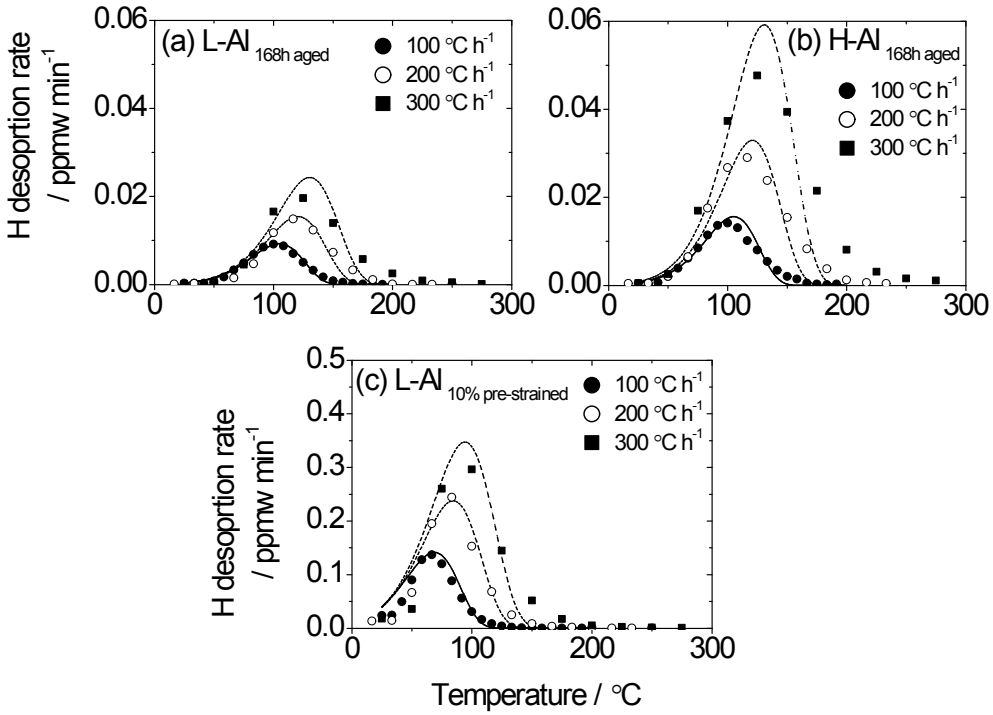

Fig. 3.6: (a,b) Charged and aged samples. Experimental data (points) for 100 ℃ h^{-1} fitted (continuous curves) using a stepwise application of Eq. 3.1 together with predicted dashed-curves for the other two heating rates. (c) Similar data and fit for a sample strained 10 % prior to TDS measurements.

To test the basis of this analysis further, a saturation-charged and unaged sample of L-Al, which has less mechanically stable austenite, was deformed to a 10 % plastic strain after which the fraction of austenite that survived was only 0.013. In such a case the diffusion distance must be set to the half-thickness of the steel sheet. Using this value of x but allowing D to be fitted for the 100 ℃ h^{-1} heating rate, gave the fit illustrated in Fig. 3.6c, with $D_0 = 2.3 \times 10^{-4}$ m^2 s^{-1} and $E_a = 39$ kJ mol^{-1}. Not surprisingly, this represents a much faster diffusion rate than in austenite but is nevertheless dramatically less than expected for ferrite where the

activation energy should be about 7 kJ mol^{-1} (Kiuchi and McLellan, 1983). This is because the hydrogen is trapped at defects, and the observed activation energy of E_a = 39 kJ mol^{-1} is well within the range of reported values for the binding energy of hydrogen at defects such as dislocations, i.e., 19-58 kJ mol^{-1} (Hirth, 1980; Choo and Lee, 1982). Once again, good agreement was obtained when the fitted values of D_0 and E_a were used to predict the desorption curves for the two greater heating rates, giving confidence in the analysis.

It is normal to analyse TDS spectra for activation energies by studying the change in T_p as a function of heating rate $\emptyset$ using the Kissinger equation (Kissinger, 1957) with the additional assumption of a first-order reaction as:

$$\frac{dX}{dt} = A(1-X)\exp\left(-\frac{E_a}{RT}\right) \tag{3.2}$$

$$\frac{\partial \mathrm{h}\ (\emptyset T_p^{-2})}{\partial T_p^{-1}} = -\frac{E_a}{R} \tag{3.3}$$

where $\frac{dX}{dt}$ is the desorption rate, A is constant and X is the fraction "reacted". For example, the energy of 29 kJ mol^{-1} for L-Al sample 10 % strained is inferred from the slope of a $\ln(\emptyset T_p^{-2})$ *vs* T_p^{-1} plot as shown in Fig. 3.7a. The value is quite consistent with the reported that of 27 kJ mol^{-1} for the dislocations with the TDS and Kissinger equation (Choo and Lee, 1982). Using this value of E_a but allowing A of Eq. 3.2 to be fitted for the 100 ℃ h^{-1} heating rate, gave the fit illustrated in Fig. 3.7b, with the A = 24 s^{-1}. The desorption curves for the two greater heating rates were predicted with the fitted values. However, the activation energies did not adequately represent the shapes of the desorption curves. This is because the Kissinger equation does not represent the physical events appropriate for such experiments, where we have hydrogen diffusing out of the free surfaces of the 1mm steel sample used. First–order kinetics of the type described by the Kissinger analysis are more appropriate for cases where the reaction occurs homogeneously throughout the assembly so that specimen dimensions are not relevant.

(a)

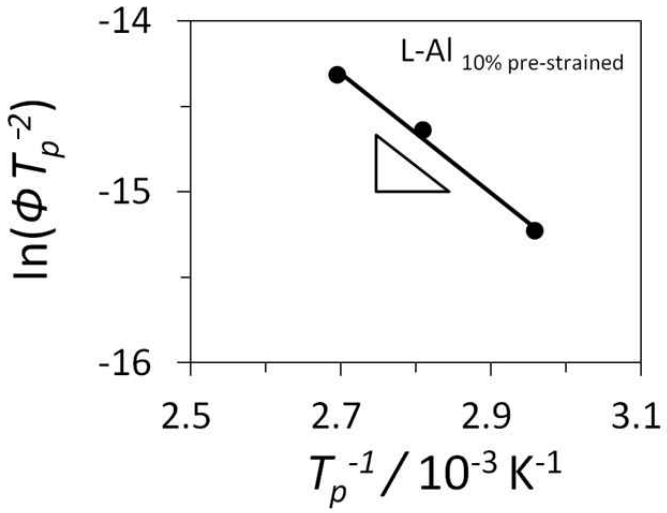

(b)

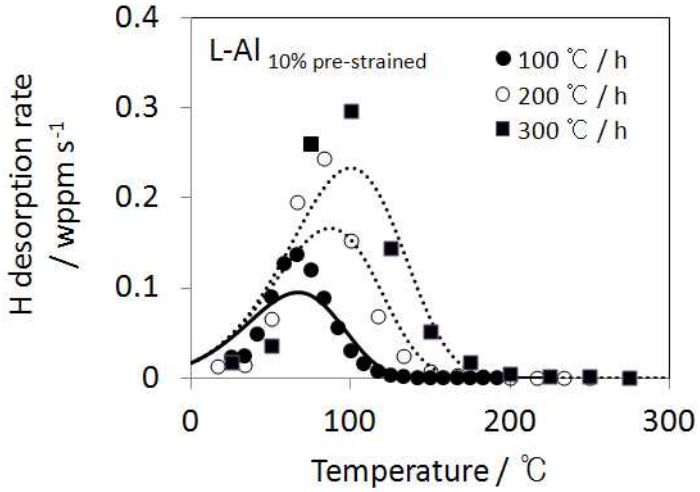

Fig. 3.7: (a) Plots of a $\ln(\emptyset T_p^{-2})$ *vs* T_p^{-1}. The activation energy can be inferred from the labeled slopes of plot according to Eq. 3.3. (b) Experimental data (points) for 100 ℃ h^{-1} fitted (continuous curves) using Eq. 3.2 together with predicted dashed-curves for the other two heating rates.

3.3.3 Simultaneous Effusion from Traps and Austenite

The data used in the preceding analysis with the Eq. 3.1 are summarised in Table 3.2; they define the separated data for the trapping of hydrogen in austenite (derived from charged and aged samples) and at defects within the ferrite (derived from deformed material). It now becomes possible to use these to interpret multiphase effects where the TDS spectra of saturation charged samples containing both retained austenite and traps within the ferrite, but it is necessary to partition the total hydrogen into these two sites. Fig. 3.8 shows the deconvolution of the 100 ℃ h^{-1} data into hydrogen evolving from traps in the ferrite and that from austenite. This was achieved by best fitting the experimental data to assumed values of the concentrations of hydrogen at traps C_α^H and in austenite C_γ^H, with $C^H = C_\alpha^H + C_\gamma^H$, but taking all other values as listed in Table 2. The values of these concentrations are

Sample	C_α^H / ppmw	C_γ^H / ppmw
L-Al	2.5	3
H-Al	4	5

With these values fixed, it is possible to predict reasonably well the corresponding TDS curves for the other two higher heating rates as illustrated in Fig. 3.8.

Table 3.2: Parameter values derived from present work. α and γ represent ferrite and austenite respectively. The values of x are specific to the present work, with x_γ being the size of austenite clusters in the mixed structure, and x_α the steel sheet half-thickness in a fully ferritic sample.

Comment	D_0 / m^2 s^{-1}	E_a / kJ mol^{-1}	x / mm
Reported values for H dissolved in γ	7×10^{-7}	48	0.012
Fitted values for H at defects in α	2.3×10^{-4}	39	0.5

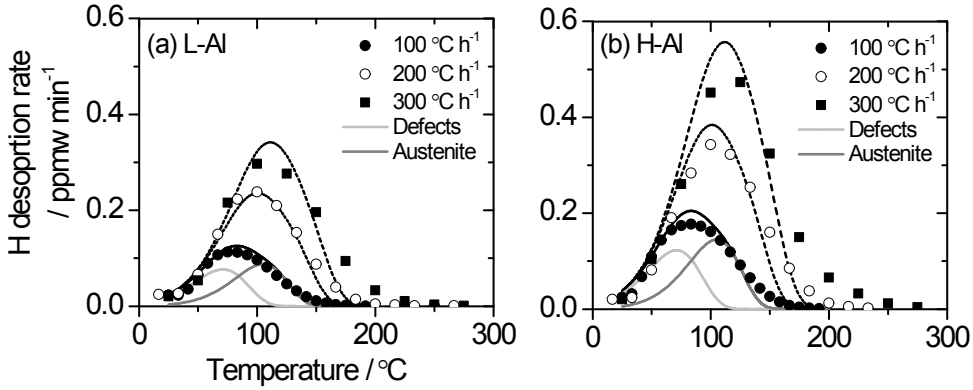

Fig. 3.8: Saturation charged specimens in which the 100 ℃ h^{-1} data are used to determine the partitioning of hydrogen trapped in austenite and defects, and the remaining heating rate curves (dashed) are predicted.

Fig. 3.9 shows the C^H for samples strained prior to saturation hydrogen-charging. Generally in ferritic steels, the C^H is known to increase with the generation of defects by deformation as H-Al 900 specimen. However, some of the austenite will undergo martensitic transformation when the TRIP steel is plastically deformed. Thus, both the increment of defect density and the decrement of austenite fraction with deformation have influence on the overall content. If it is assumed that the amount of hydrogen trapped in austenite is proportional to its fraction, then it should be possible now to predict the TDS curves for samples which are deformed, charged and subjected to desorption analysis. However, there have been suggestions that hydrogen influences the stability of retained austenite in severely charged samples (Ulmer and Altstetter, 1993; Rozenak and Bergman, 2006; Mine *et al*., 2009). It was therefore felt necessary to first investigate whether the decomposition of austenite depends on the hydrogen concentration, but it is in fact found that there is no significant dependence in the alloys studied, as illustrated in Fig. 3.2.

The analysis presented in Fig. 3.10 shows that without any fitting parameters beyond those already described, and the retained austenite data from Fig. 3.2, it becomes possible to predict the TDS spectra of samples which have been deformed,

saturation charged and then heated at 100 ℃ h^{-1}.

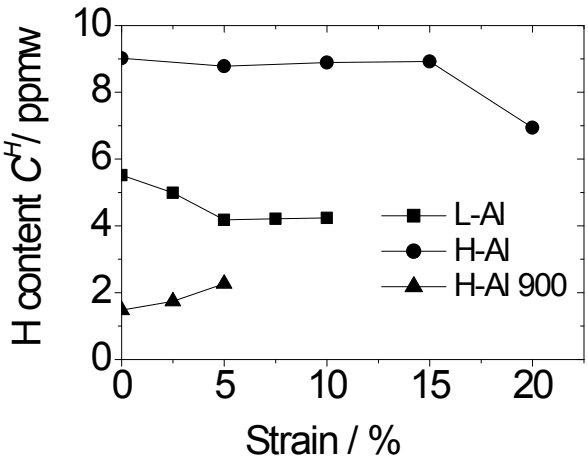

Fig. 3.9: Hydrogen contents C^H in specimens as a function of pre-strain.

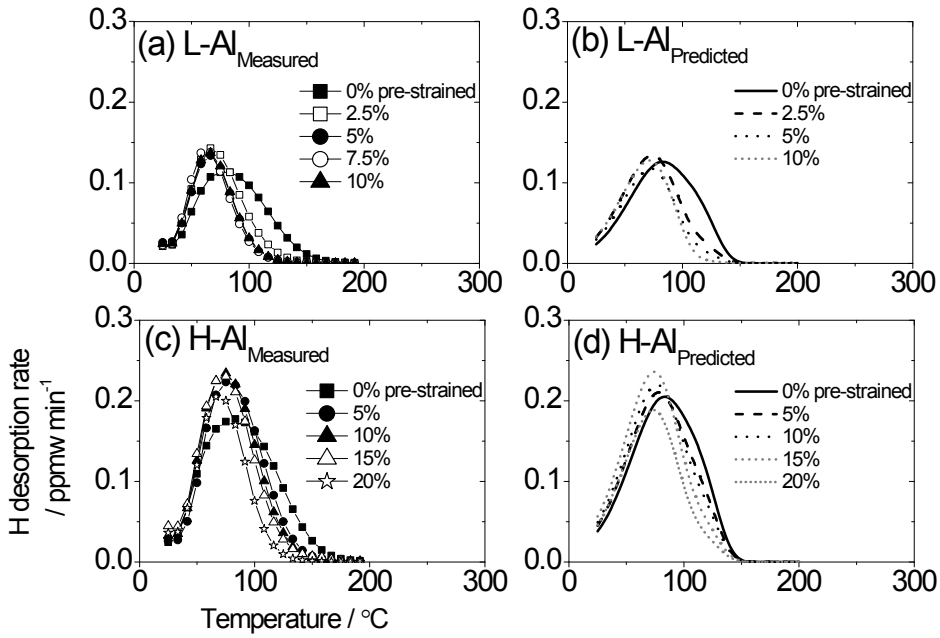

Fig. 3.10: Measured (a,c) and predicted (b,d) thermal desorption spectra for samples strained prior to saturation hydrogen-charging.

3.3.4 Tensile Properties and Trap Transfer

Fig. 3.11 shows the slow strain-rate tensile test results for L-Al and H-Al samples as a function of the amount of pre-charged hydrogen. There is the expected decrease in ductility with increasing hydrogen content but interestingly, no significant change in the work hardening behaviour. This is expected, since as shown above (Fig. 3.2), the hydrogen does not influence the stability of the austenite. Furthermore, the effect of hydrogen on solid solution strengthening at ambient temperature is rather small (< 35 MPa) (Asano and Otsuka, 1976), which probably is within the scatter expected in the strong steels studied here.

Austenite transforms into martensite during deformation, thereby transferring hydrogen into less potent trapping sites, thus leading to a greater quantity of diffusible hydrogen. This should lead to an enhanced deterioration in ductility specifically in TRIP-assisted steels as compared with those that do not transform as a function of plastic strain. The transfer of hydrogen and consequential effect on ductility was proven by conducting tensile tests using a higher strain rate of 10^{-2} s^{-1}, since it is known not only that austenite becomes less stable at higher strain rates in the absence of adiabatic heating, but also that the ductility increases because of a competition between hydrogen mobility and plastic deformation (Bernstein, 1970). This was confirmed in the tensile tests (Fig. 3.12a,b); the austenite fractions for the high strain rate samples at a strain corresponding to fracture, decreased to 0.05 and 0.20 in L-Al and H-Al respectively. The accompanying TDS results in Fig. 3.12c,d are quite revealing, where samples which were charged before straining, charged after straining, and those without straining, were subjected to TDS analysis. They prove conclusively that the deformation-induced decomposition of the austenite places the hydrogen into regions where it has a greater diffusivity.

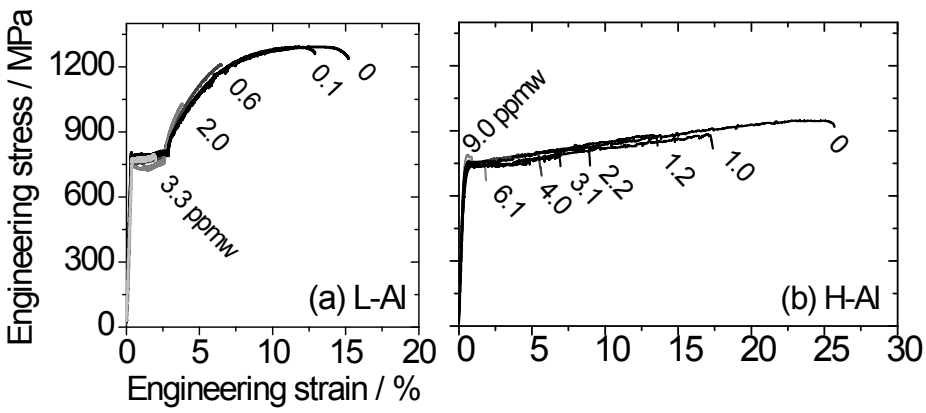

Fig. 3.11: Stress-strain curves of pre-charged (a) L-Al and (b) H-Al alloys tested at a strain rate of 10^{-5} s^{-1}. Diffusible hydrogen contents in specimen are labelled in ppmw.

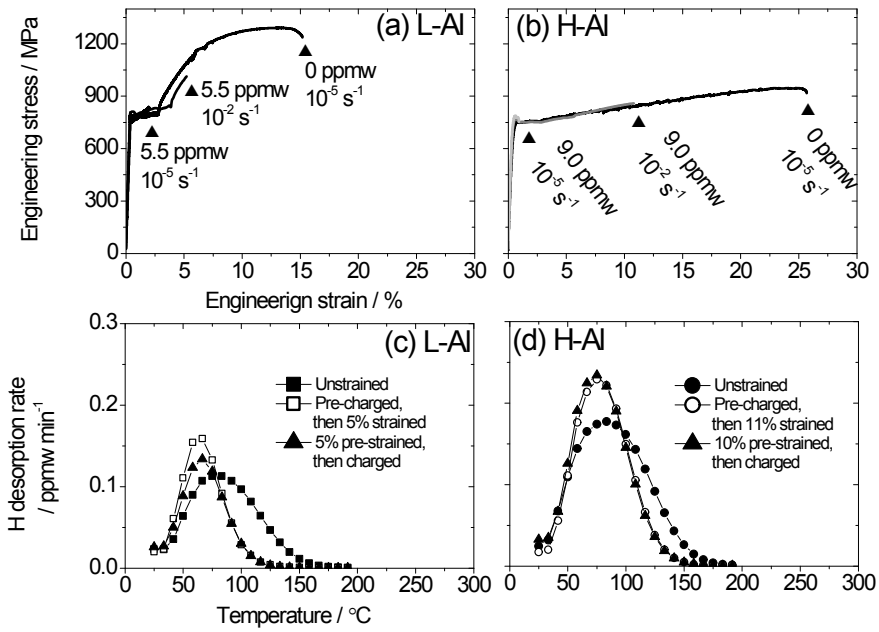

Fig. 3.12: Stress-strain curves of (a) L-Al and (b) H-Al alloys tested at different strain rates. Thermal desorption profiles of (c) L-Al and (d) H-Al alloys. Pre-charged and then strained specimens are compared with pre-strained and then charged ones.

Thus, the mechanical stability of austenite may affect the susceptibility to hydrogen embrittlement. Fig. 3.13 indicates that the L-Al alloy which contains austenite of lower stability has the higher susceptibility according to elongation *El* loss expressed as:

$$El \text{ loss} = 100 \times \left(El_{uncharged} - El_{charged}\right)/(El_{charged}) \qquad (3.4)$$

The fracture surfaces in Fig. 3.14a,b indicate the fracture occurs partially in a brittle manner for specimens charged. Many microcracks are found in the neighborhood of the fracture surface along the grain boundary in Fig. 3.14d, which propagates perpendicular to tensile axis. Furthermore, Fig. 3.14c indicates a microcrack adjacent to martensite. The conclusion that the region is martensitic is supported by the observation of a high manganese concentration, inherited from the austenite. Similarly, the larger amount of dissolved hydrogen in the austenite will be inherited by the martensite, thus causing it to be severely embrittled.

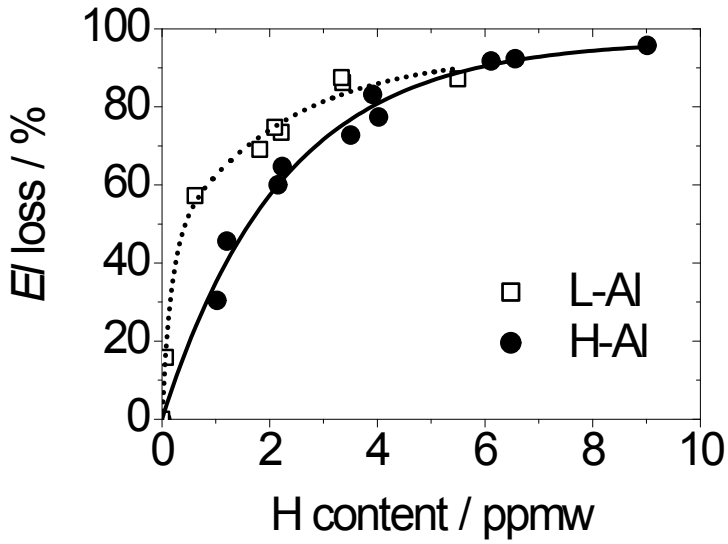

Fig. 3.13: Elongation *El* loss as a function of hydrogen content.

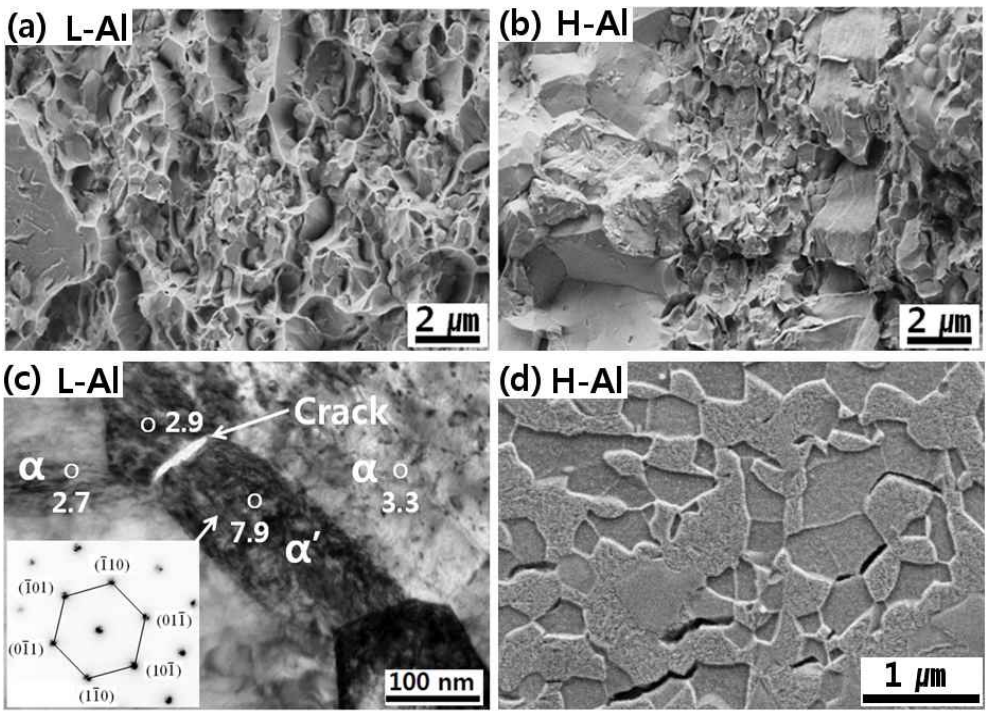

Fig. 3.14: Fracture surfaces and microcracks observed in (a,c) L-Al samples charged to 3.3 ppmw, and in (b,d) H-Al samples charged to 9.0 ppmw. Mn contents are labeled and α′ represents martensite.

3.4 Summary

The trapping of hydrogen at a variety of sites in multiphase transformation-induced plasticity (TRIP) steels has been characterised using thermal desorption spectroscopy and the results have been modelled using diffusion theory. It is discovered that austenite serves as a reversible trapping site which is more potent than grain boundaries or dislocations in ferrite. Plastic deformation which leads to the partial martensitic transformation of the austenite results in an alteration in the trapping condition of the inherited hydrogen. It is demonstrated that these phenomena can be incorporated into a mathematical model which permits the desorption of hydrogen to be predicted quantitatively as a function of, for example, the heating rate, phase fractions, and phase transformation. An interesting outcome is that the mechanical degradation of the steel by hydrogen is more pronounced in TRIP steel containing austenite which is relatively less stable to martensitic transformation during deformation. This is because the phase transformation causes a reduction in the trap binding energy, thus enhancing the apparent mobility of the hydrogen.

Chapter 4: Effect of Al on Hydrogen Embrittlement in TWIP Steel

4.1 Introduction

High-manganese twinning-induced plasticity (TWIP) steels are currently promising candidates for applications in the automotive industry due to their exceptional combination of strength and elongation (De Cooman *et al*., 2009). However, they have yet to be commercialised because some of them may be prone to delayed fracture after forming. Chin *et al*. (2011) reported that delayed fracture occurred after cup-forming and subsequent exposure in air for 7 days even though the specimen was not cracked or fractured during the forming of Fe–22Mn–0.6C wt% TWIP steel. However, in a Fe-18Mn-1.2Al-0.6C wt% TWIP steel, cracking did not occur regardless of the exposure times in air. Although fracture can be avoided by adding aluminum (Kim *et al.*, 2008), the operative mechanism has not been revealed.

There are several investigations about hydrogen embrittlment in TWIP steels to explain the delayed fracture (Ronevich *et al*., 2010; Jung *et al*., 2008; So *et al*., 2009; Mittal *et al*., 1994). However, the observed mechanical degradation by tensile testing after pre-charging with hydrogen has been found to be negligible. Only Koyama *et al*. (2011) have showed a clear deterioration of tensile properties for Fe-18Mn-0.6C (wt%) TWIP steels strained during charging. But, it remains the case that there is no research about the mechanistic effect of adding Al to TWIP steels, with respect to hydrogen embrittlement. It certainly cannot be concluded that the delayed fracture is related with hydrogen entry and can always be avoided by adding Al.

4.2 Experimental

4.2.1 Alloys

Table 4.1 lists the chemical compositions of two alloys, 0TWIP and 1.5TWIP.

The alloys were cold-rolled to 1.2 mm in thickness and then annealed using an infrared furnace at 900 ℃ for 15 min. The heating and cooling rates were 10 ℃ s^{-1}.

Table 4.1: Chemical compositions of samples in wt %

	C	Mn	Al
0TWIP	0.6	18	0
1.5TWIP	0.6	18	1.5

4.2.2 Microstructural Characterisation

To reveal optical microstructures, the samples were mechanically ground, polished, and then etched with an aqueous solution of 10 % $Na_2S_2O_5$. The microstructures also were observed using a field emission gun scanning electron microscope (FE-SEM) equipped with an electron back-scattered diffraction (EBSD) facility. In the latter case the specimens were finally mechanically polished with a colloidal silica suspension and the step size was 0.1 μm. The phases were determined using X-ray diffraction (XRD) with CuK_α radiation. Integrated intensities of $10\bar{1}0_\varepsilon$, $10\bar{1}1_\varepsilon$, $10\bar{1}2_\varepsilon$, $10\bar{1}3_\varepsilon$, and 111_γ, 200_γ, 220_γ reflections were used for the quantitative phase fraction measurements (Yang and Luo, 2000). A focused ion beam was used in preparing specimens for transmission electron microscopy to investigate the microstructure around the fracture surfaces which were preserved with carbon and platinum deposition.

4.2.3 Hydrogen Charging and Thermal Desorption

Tensile test coupons with a 50 mm gage length, 12.5 mm width and 1.2 mm thickness were prepared according to the ASTM E8M, polished with the 800 SiC grit papers and charged electrochemically with the hydrogen in an aqueous mixture of 3 % NaCl + 0.3 % NH_4SCN at 0.5-5 A m^{-2}. Thermal desorption spectroscopy (TDS) with gas chromatography was conducted at constant heating rates of

100 ℃ h^{-1} to a maximum temperature of 300 ℃. The gage length part of each charged-tensile sample was cut immediately after charging and placed in the TDS furnace. The sample gas was analysed at 3 min intervals using helium as a carrier gas and the desorption rate was defined as the amount of hydrogen evolved in 1 min per gram of the specimen. A standard mixture He + 10.2 volume ppm of H_2 was used for the calibration.

4.2.4 Mechanical Tests

Slow strain rate tensile tests were conducted on the specimens charged dynamically during the test at a constant crosshead speed of 0.03 mm min^{-1}, corresponding to a nominal strain rate of 10^{-5} s^{-1}. In the case the tests were done without an extensometer as shown in Fig. 4.1, and then total elongations were determined by measuring the gage length before and after the test. A faster strain rate of 10^{-3} s^{-1} was used to examine the hydrogen-induced phase transformation during deformation.

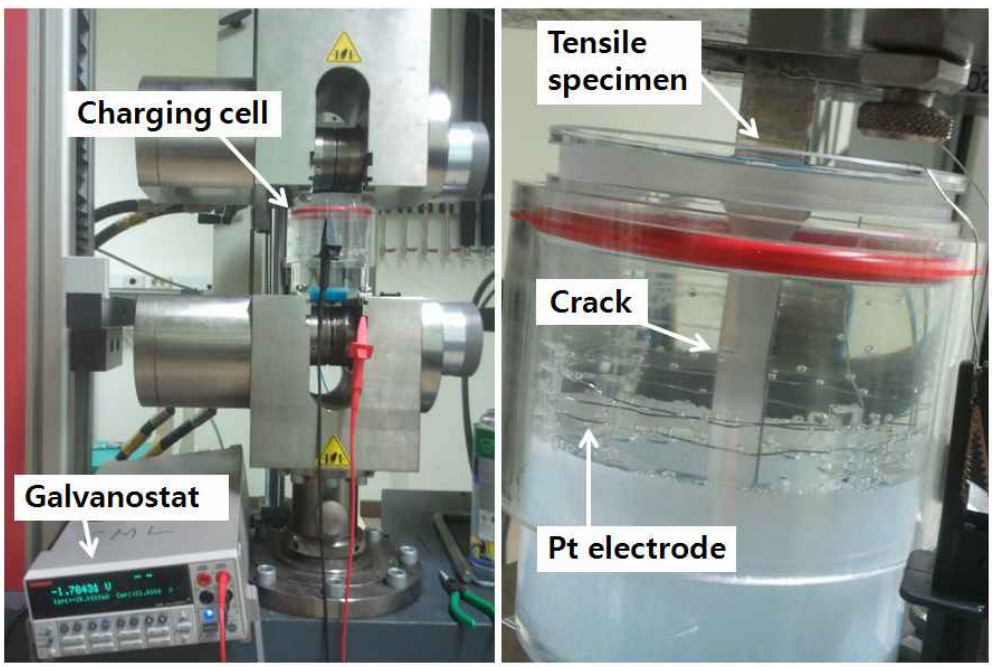

Fig. 4.1: Configuration of tensile test with dynamic hydrogen charging.

4.2.5 Hydrogen Microprint Technique

Hydrogen emission from samples was visualized using the hydrogen microprint technique (HMT) (Matsunaga and Noda, 2011; Ovejero-Garcia, 1985). The samples were mechanically polished and then charged with hydrogen. The sample surface was covered with a mixture of 5 g gelatin-based AgBr emulsion (Ilford L-4) + 10 ml distilled water. After holding the sample in ambient air for 10 min, it was dipped into 38 % formalin for 1 second to harden the gelatin film, and then immersed in 17 % $Na_2S_2O_3$ + 5 % $NaNO_2$ aqueous solution for 3 min to wash away any unreacted AgBr particles. After rinsing the sample surface with distilled water and drying, silver particles present on the sample surface were observed with the SEM and energy dispersive spectroscopy (EDS).

4.3 Results and Discussion

4.3.1 Microstructure

Fig. 4.2 illustrates representative microstructures; the grain sizes in 0TWIP and 1.5TWIP are 5.2 ± 0.6 and 6 ± 0.3 μm respectively as characterised with the mean linear intercept method (Dehoff and Rhines, 1968), including annealing twin boundaries. The stress-strain curves of the samples are presented in Fig. 4.3. The high strain hardening of the samples results from dynamic strain aging (Adler *et al*., 1986; Shun *et al*., 1992) or the dynamical Hall-Petch effect due to mechanical twinning (Remy, 1978; Allain *et al.*, 2004; Bouaziz *et al*., 2008; Idrissi *et al*., 2010). Adding of Al decreases the hardening because it reduces the strain aging which leads to serrated flow curves, and the mechanical twinning by increasing the stacking fault energy (SFE) of the alloys (Kim *et al*., 2011). Fig. 4.4 represents the microstructures for samples strained to 30 %. It reveals that a relatively large fraction of mechanical twinning occurs in 0TWIP, and that both alloys are fully austenitic. The XRD result in Fig. 4.5 confirms that martensitic transformation doesn't occur in the alloys even at fracture as reported by Jung *et al*. (2010).

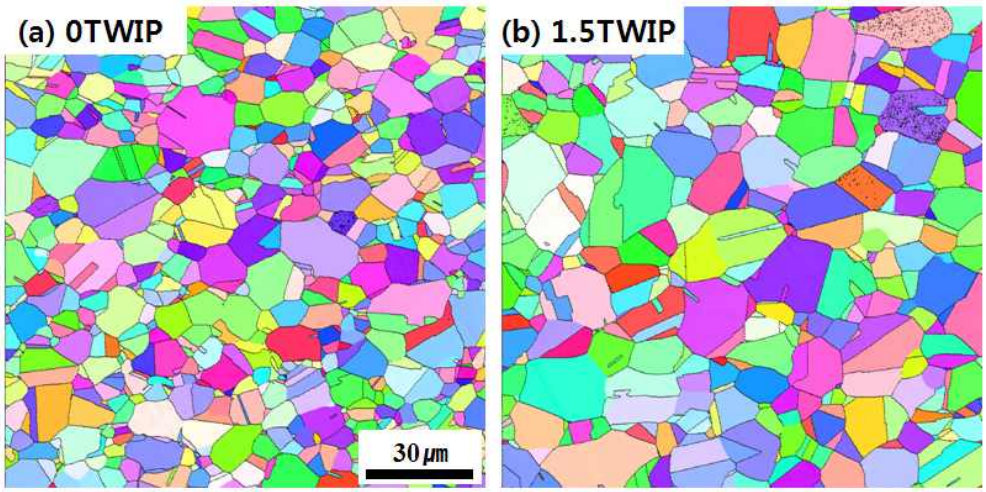

Fig. 4.2: EBSD inverse pole figure mapping of (a) 0TWIP and (b) 1.5TWIP alloy after annealing at 900 ℃ for 15 min.

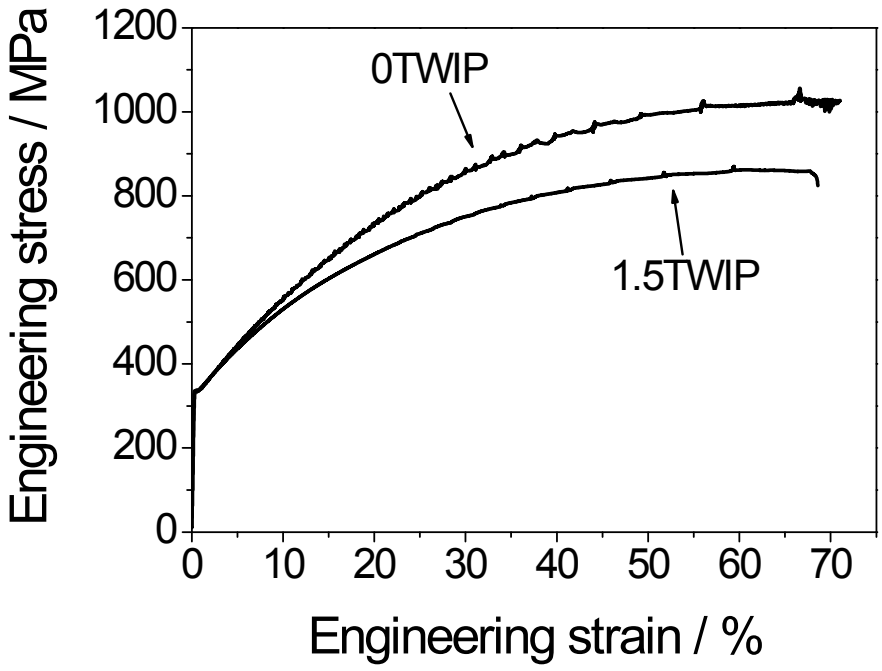

Fig. 4.3: Stress-strain curves of the alloys annealed at 900 ℃ for 15 min.

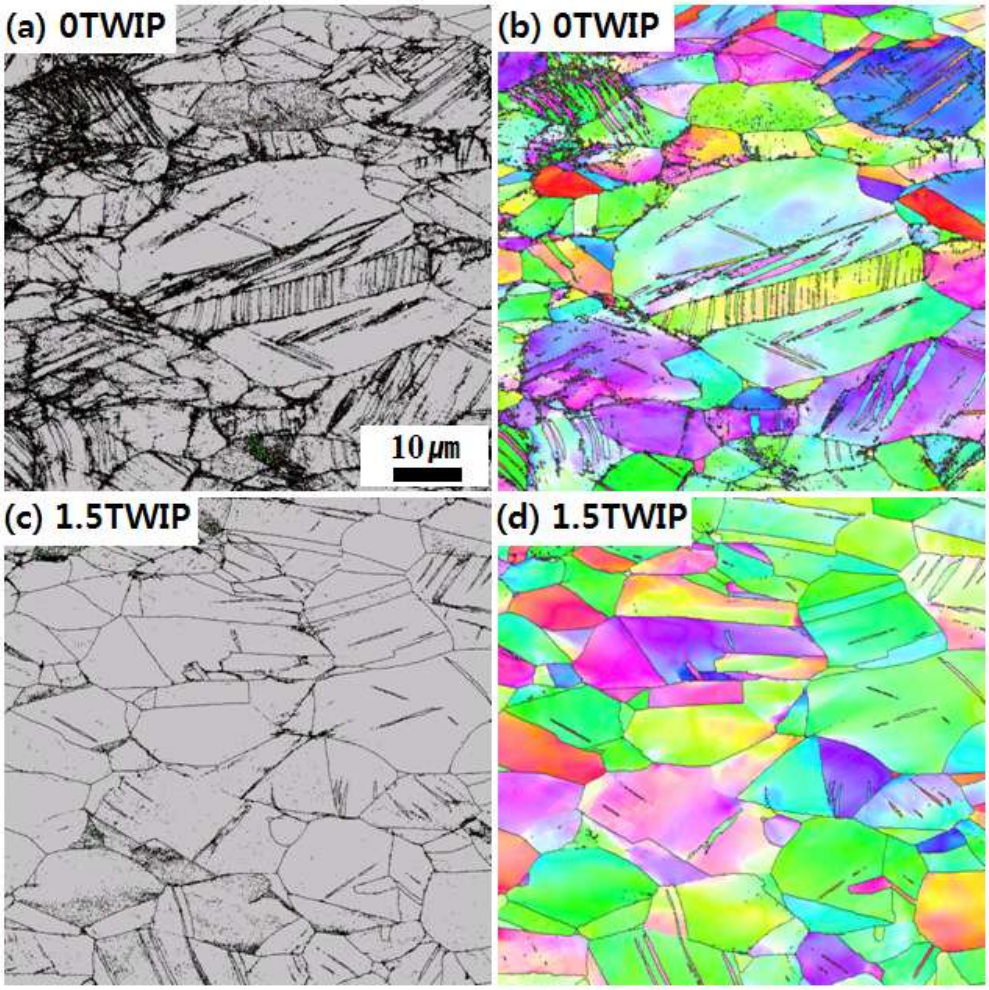

Fig. 4.4: EBSD phase mapping of (a) 0TWIP and (c) 1.5TWIP in which austenite is represented as gray. Inverse pole figure mapping of (b) 0TWIP and (d) 1.5TWIP.

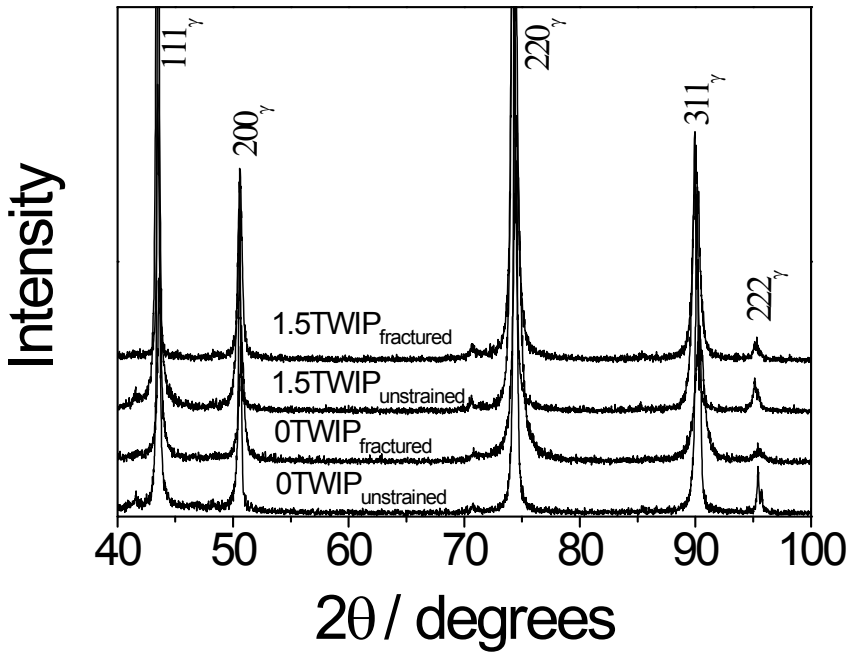

Fig. 4.5: XRD results of tensile samples before deformation, and after fracture.

4.3.2 Degradation of Tensile Properties

Fig. 4.6 shows the slow strain-rate tensile test results for 0TWIP and 1.5TWIP samples charged dynamically at varied current densities during the test. The total elongations were obviously deteriorated by the hydrogen charging. However, there is no significant change in the strain hardening behaviour, consistent with the work of Koyama *et al*. (2011) for the 0TWIP alloy. The level of degradation is presented in Fig. 4.7 with the losses expressed as:

$$El \text{ loss} = 100 \times \left(El_{uncharged} - El_{charged}\right)/(El_{uncharged}) \quad (4.1)$$

$$\sigma \text{ loss} = 100 \times \left(\sigma_{uncharged} - \sigma_{charged}\right)/(\sigma_{uncharged}) \quad (4.2)$$

The results indicate that the degradation increases with the current density, but is reduced by adding the Al.

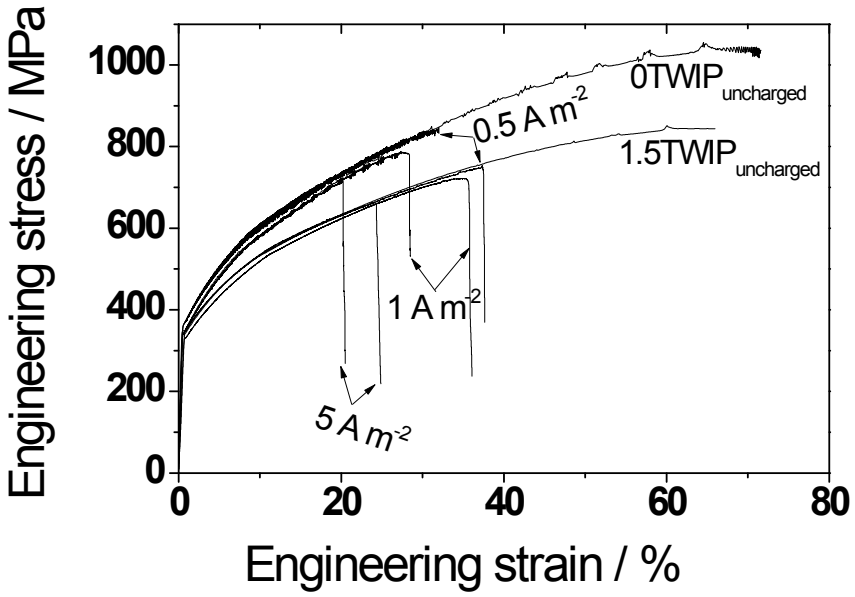

Fig. 4.6: Stress-strain curves of samples tensile-tested with dynamic hydrogen charging at varied current densities.

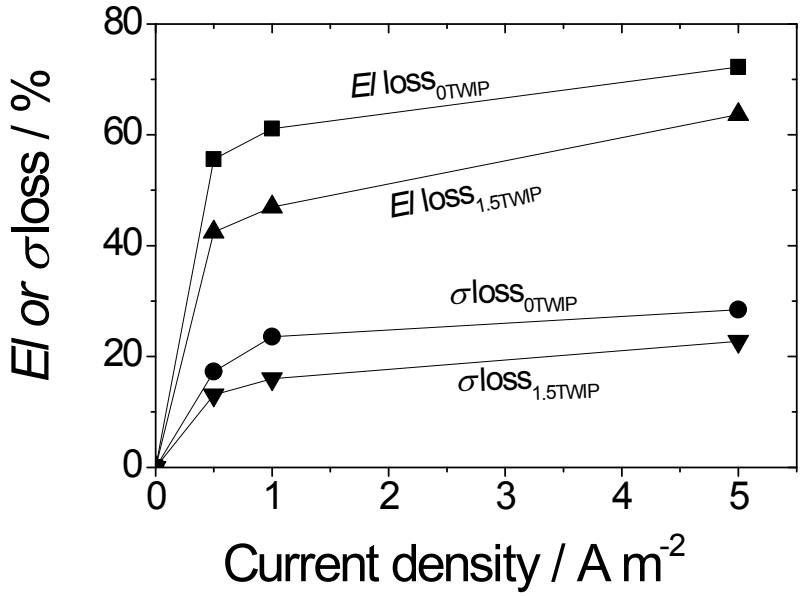

Fig. 4.7: Elongation *El* and strength σ loss as a function of charging current density.

The fracture surfaces in Fig. 4.8 indicate that the failure occurs partially in a brittle manner near the surface of the samples, and the depth of the brittle fractured part is proportional to the level of degradation. On the other hand, the fracture surfaces of the central region of the charged-samples showed ductile fracture with dimples which were similar to those of uncharged-samples as shown in Fig. 4.9.

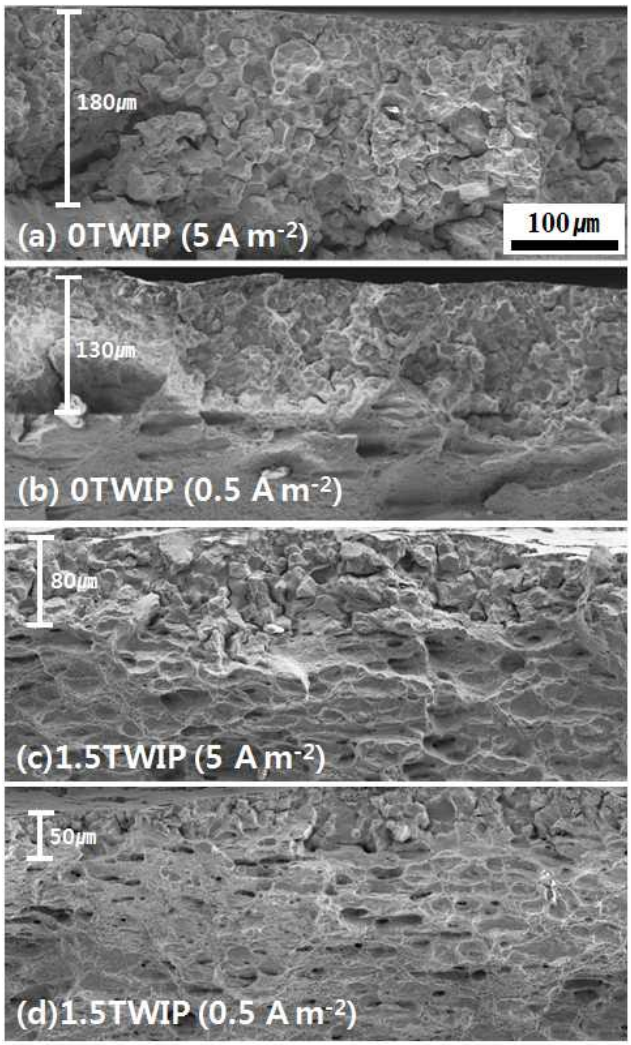

Fig. 4.8: Fracture surfaces of (a,b) 0TWIP and (c,d) 1.5TWIP charged at 5 A m^{-2} and 0.5 A m^{-2} respectively.

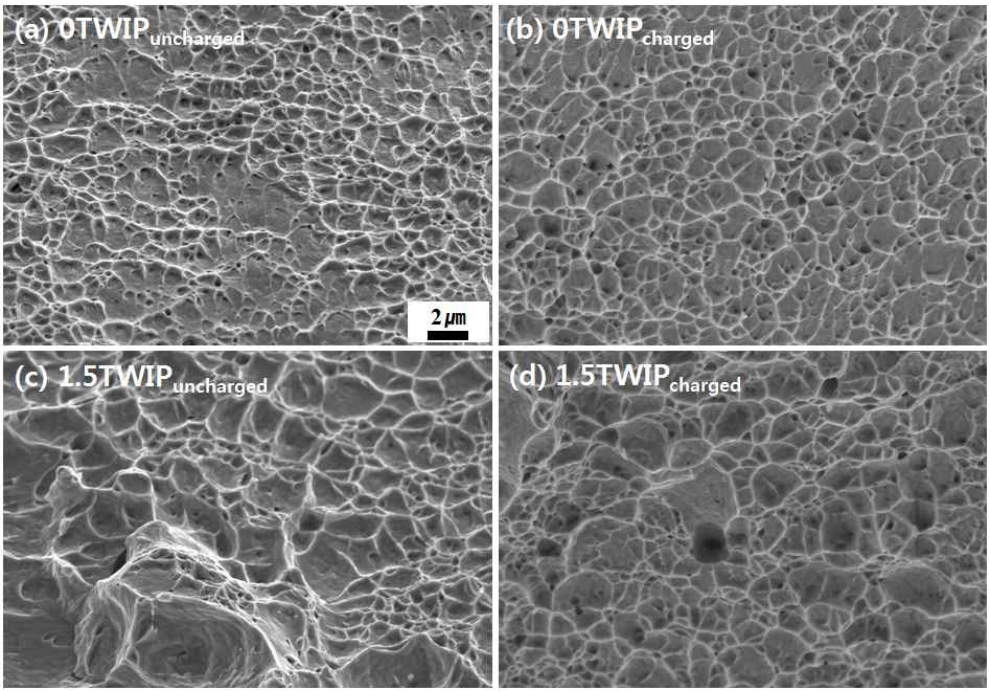

Fig. 4.9: Fracture surfaces of (a,c) uncharged samples and (b,d) center part of charged-samples .

Fig 4.10 shows the fracture surfaces of samples charged at 1 A m^{-2}. It clearly indicates not only intergranular but also transgranular fracture in the brittle area. It is well known that grain boundaries and dislocations are trap sites for diffusible hydrogen which causes the mechanical degradation. Furthermore, the hydrogen can be transported by the dislocations, and then accumulated on the boundaries, which may cause the intergranular fracture. Similarly, mechanical twins also act as a barrier to the dislocations for the dynamical Hall-Petch effect. Thus the hydrogen may also be segregated on the twins resulting in the transgranular fracture. It is necessary to research more about the trapping of hydrogen in these alloys.

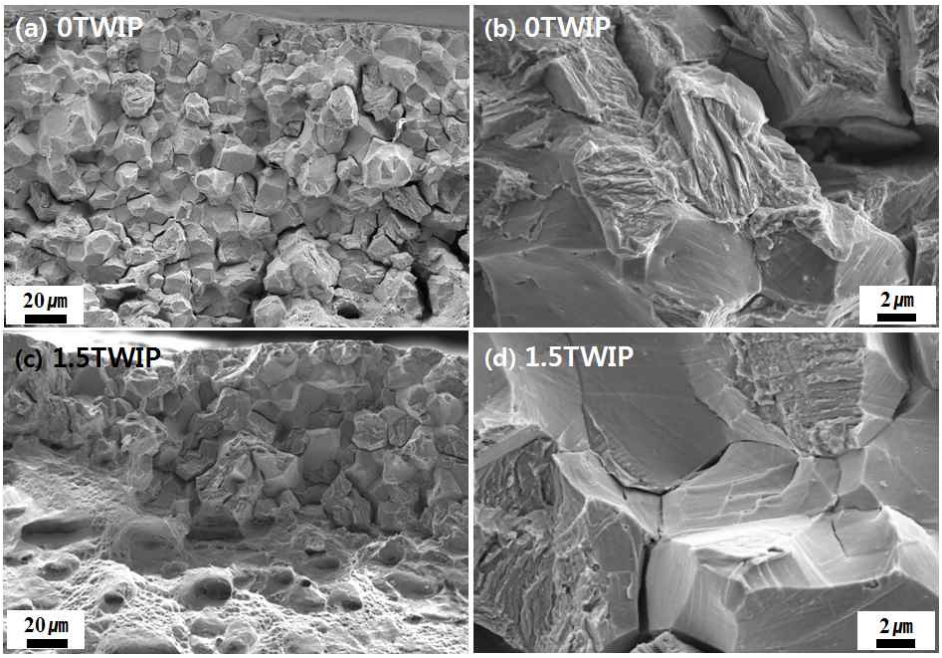

Fig. 4.10: Intergranular and transgranular fracture observed in (a,b) 0TWIP and (c,d) 1.5TWIP samples.

4.3.3 Hydrogen Trapping

Fig. 4.11 shows the TDS spectra for uncharged and dynamically hydrogen-charged samples, the latter charged during the tensile test, indicating that diffusible hydrogen (released at below 200 ℃) was introduced by the charging. The increase of charging current density which determines the concentration of hydrogen on the sample surface enhances the hydrogen uptake, and also mechanical degradation as shown in Fig. 4.7. Thus it reduces the charging time (duration of tensile test) and amount of strain to generate defects for the hydrogen trapping, resulting in a decrease of the measured hydrogen content C^H as shown in Table 4.2.

The cracking observed in the brittle part of fractured samples may initiate from the sample surface due to its larger concentration of hydrogen. In that case, the hydrogen is readily supplied to the crack tip without the need for lattice diffusion because the interior of the crack will be filled immediately by the charging solution.

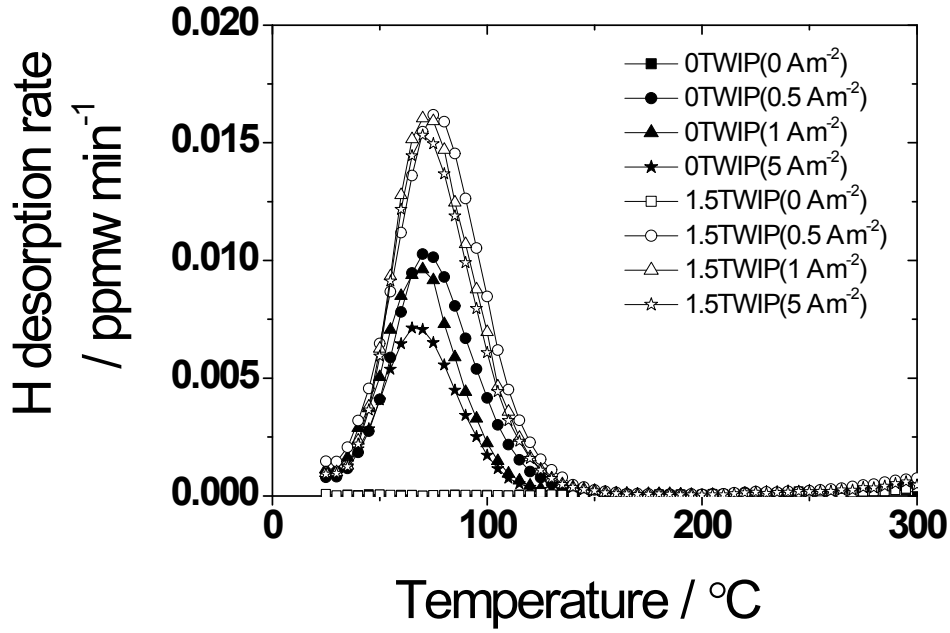

Fig. 4.11: Thermal desorption profiles for fractured samples.

Table 4.2: Hydrogen contents C^H of fractured samples and charging time (duration of tensile test) at varied charging current density.

	Current density / A m^{-2}	C^H / ppmw	Charging time / s
0TWIP	0.5	0.31	42132
	1	0.28	36117
	5	0.21	26985
1.5TWIP	0.5	0.53	49545
	1	0.48	45726
	5	0.45	32720

This will promote the propagation of the crack front. The hydrogen concentration

on the crack tip, therefore, is assumed to be same with the one on the sample surface if an effect of stress field on the hydrogen absorption there is ignored. To calculate the surface concentration at varied current densities, samples of 0TWIP and 1.5TWIP were charged for 72 h without deformation, then the hydrogen contents were measured as listed in Table 4.3. However, the values don't represent the local concentration of hydrogen. Fig. 4.12 shows the concentration as a function of depth z according to:

$$C_z^H = C_S^H \left(1 - \mathrm{erf}\left(\frac{z}{2\sqrt{D_H t}}\right)\right) \quad (4.3)$$

where C_z^H is the local concentration at a depth z from the surface, D_H is diffusion coefficient for hydrogen in austenite and t is the charging time; D_H was about 3.7×10^{-16} m^2 s^{-1} based on 310 austenitic stainless steel (Perng and Altstetter, 1986). The result shows that the surface concentrations C_S^H at 5 A m^{-2} are 23 and 29 ppmw for 0TWIP and 1.5TWIP respectively, and decrease with the current density. Thus, crack initiation and propagation can occur easily at high current density.

Table 4.3: Hydrogen contents C^H of samples charged without deformation for 72 h.

	Current density / A m^{-2}	C^H / ppmw
0TWIP	0.5	0.33
	1	0.36
	5	0.46
1.5TWIP	0.5	0.43
	1	0.48
	5	0.58

On the other hand, calculated diffusion lengths during the tensile tests are less than 20 μm using the Eq. 4.3 for the time to fracture in Table 4.2. However, the

observed depths of the brittle fracture in Fig. 4.8 are much larger than the diffusion length, suggesting the fast supply of hydrogen through the interior of the crack rather than the lattice diffusion as mentioned before or increase of apparent diffusivity due to hydrogen transport by mobile dislocations (Louthan *et al.,* 1972; Tien *et al*., 1976).

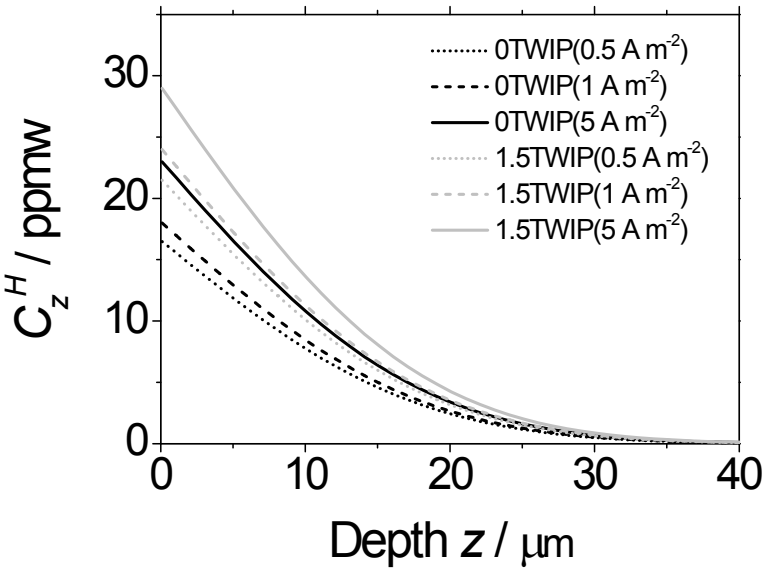

Fig. 4.12: (a) Local concentration C_z^H of hydrogen at a depth z.

Most of diffusible hydrogen in samples after the tensile test might be trapped in grain boundaries and dislocations. To confirm the trapping in grain boundaries, samples were annealed at different temperatures of 800, 900 and 100 ℃, and then charged at 1 A m^{-2} for 72 h; microstructures are presented in Fig. 4.13, and their grain sizes L in Fig. 4.14a. TDS results in Fig. 4.14b,d show the increase of

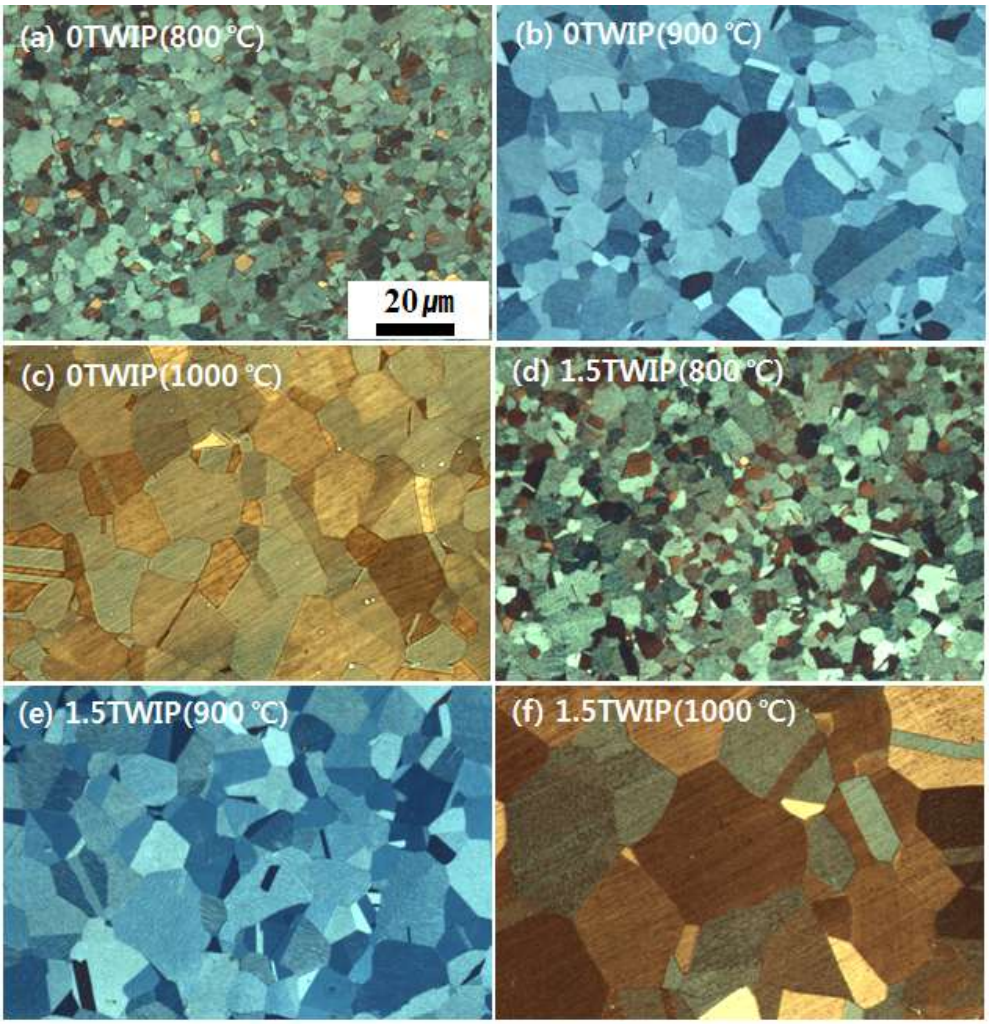

Fig. 4.13: Optical microstructure of samples annealed at different temperature for 15 min.

desorption rate by decreasing the grain size because the grain surface area per unit volume S_v is inversely proportional to the grain size as:

$$S_v = 2L^{-1} \tag{4.4}$$

Fig. 4.14c shows a linear relationship between the $2L^{-1}$ and hydrogen content C^H. It is noted that the contents of 1.5TWIP are larger than those of 0TWIP at same grain size, but the reason is not clear in this work; the hydrogen content in this

unsteady state charging may depend on both the diffusivity and solubility affected by various trap sites, and an effect of adding Al on the solubility in austenite lattice is not known, but contrary to expectations based on embrittlement, there is definitely a larger quantity of hydrogen absorbed.

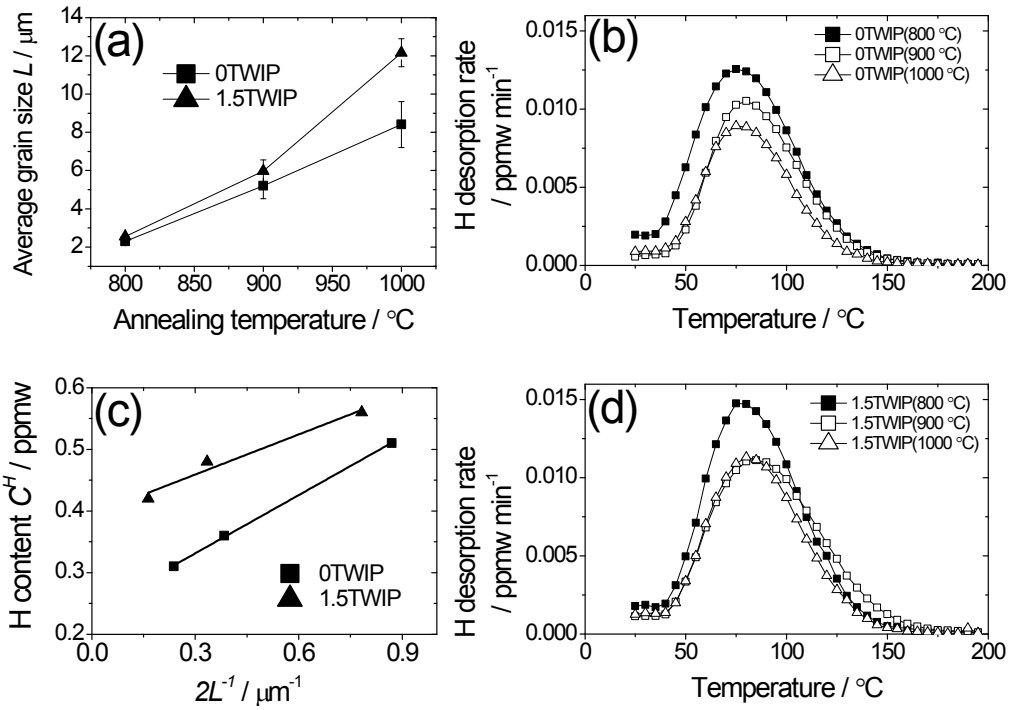

Fig. 4.14: (a) Average grain size L of sample annealed at different temperature. (b,d) TDS results of samples annealed and then charged at 1 A m^{-2} for 72 h. (c) H content C^H *vs* $2L^{-1}$ for the samples annealed and then charged.

Samples of 0TWIP and 1.5TWIP were pre-strained to 15, 30 and 45 %, and then charged at 1 A m^{-2} for 72 h to investigate the hydrogen trapping in dislocations. Fig. 4.15 shows enhanced desorption rates and C^H with the pre-strain due to the increase of dislocation density. However, further annealing at a recovery temperature 550 ℃ (Kang *et al*., 2010) for 10 min before the charging nearly eliminates the increased trapping by the dislocations.

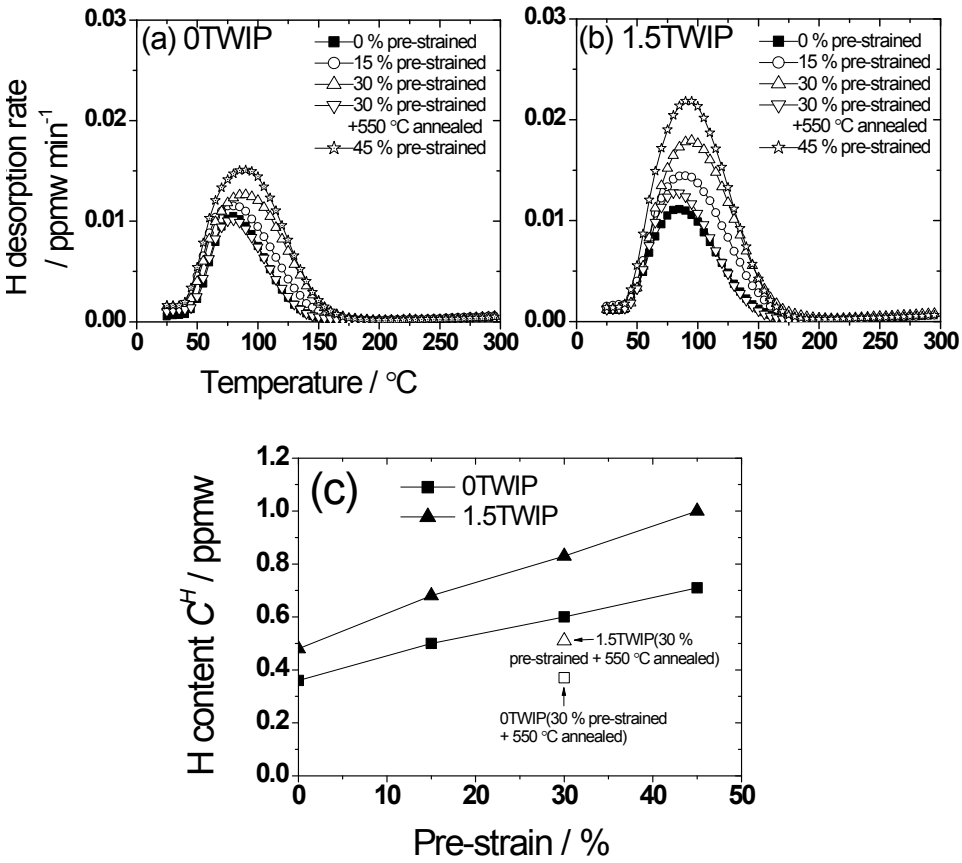

Fig. 4.15: (a,b) Thermal desorption profiles of samples pre-strained and then charged. (c) H content C^H as a function of pre-strain.

So *et al*. (2009) reported the strong trapping at mechanical twin boundaries in 1.5TWIP alloy and its trap energy was evaluated to be 62 kJ mol^{-1}. They also reported a separate peak of TDS for the twin boundaries in a temperature range 200 to 300 ℃, which was not observed even for the 45 % strained samples in this work. To reveal the trapping at mechanical twins directly, the HMT was applied for the samples 30 % pre-strained, polished and then charged at 1 A m^{-2} for 72 h. Fig. 4.16a,c show the segregation of hydrogen decorated with silver particles on the sample surface. It was confirmed that the segregation occurs at the mechanical twins as shown in Fig. 4.16d using EBSD after removing the particles by slight polishing.

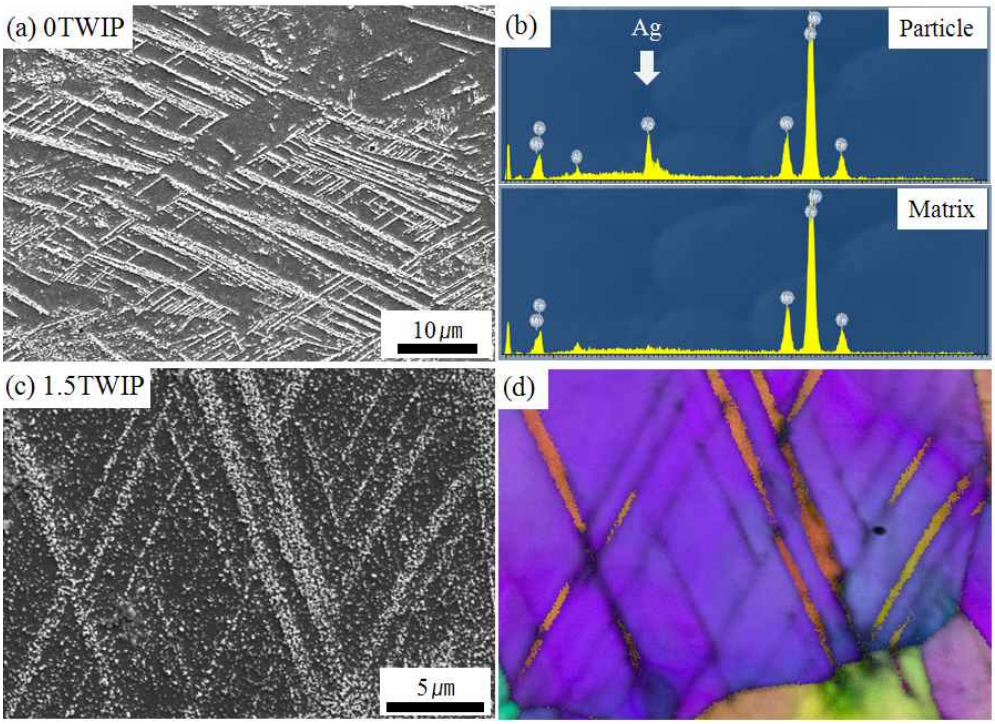

Fig. 4.16: SEM images after HMT for 30 % strained (a) 0TWIP and (c) 1.5TWIP. (b) EDS analysis for the matrix and particles. (d) Mixture of Kikuchi pattern quality and inverse pole figure mapping in same area for HMT of the 1.5TWIP.

However, the silver particles were not observed after HMT for samples charged and then heated up to 200 ℃ to remove totally the diffusible hydrogen, suggesting that the release of hydrogen trapped in the mechanical twins occurs at below 200 ℃, consistent with release from grain boundaries and dislocations. Idrissi *et al*. (2010) reported that the twins contain a huge density of sessile dislocations resulting from the mechanism of the twin nucleation and growth. Therefore, the trapping there may be caused by the dislocations, and the hydrogen transported by mobile dislocations intensifies the segregation during deformation.

4.3.4 Hydrogen-Induced ε Martensite

Martensitic phase transformation was not observed in the alloys uncharged even at the fracture. However, ε martensite was found on the sample surface of 0TWIP after tensile test with dynamic charging as shown in Fig. 4.17; the ε martensite fraction was 0.11 ± 0.02.

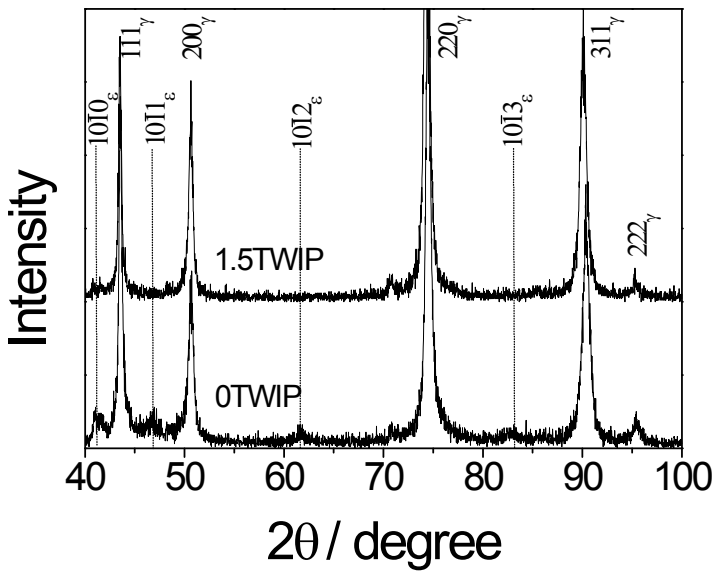

Fig. 4.17: XRD results for samples tensile-tested with dynamic charging at 1 A m^{-2}.

To study this further, samples were pre-charged at 1 A m^{-2} for 72 h, and then strained; in the case the strain rate was 10^{-3} s^{-1} to minimise the loss of hydrogen during testing. Fig. 4.18 indicates that the ε martensite was observed in 0TWIP strained to 5 % and 30 %; the martensite fractions were 0.05 ± 0.02 and 0.09 ± 0.02 for the strains respectively. However, the martensite was not found just after the charging, suggesting that the martensitic transformation occurred during deformation and its amount increased with strain. Fig. 4.19 also confirms the martensitic transformation in the 0TWIP. On the other hand, the transformation didn't occur in 1.5TWIP though it contains larger hydrogen content after the charging.

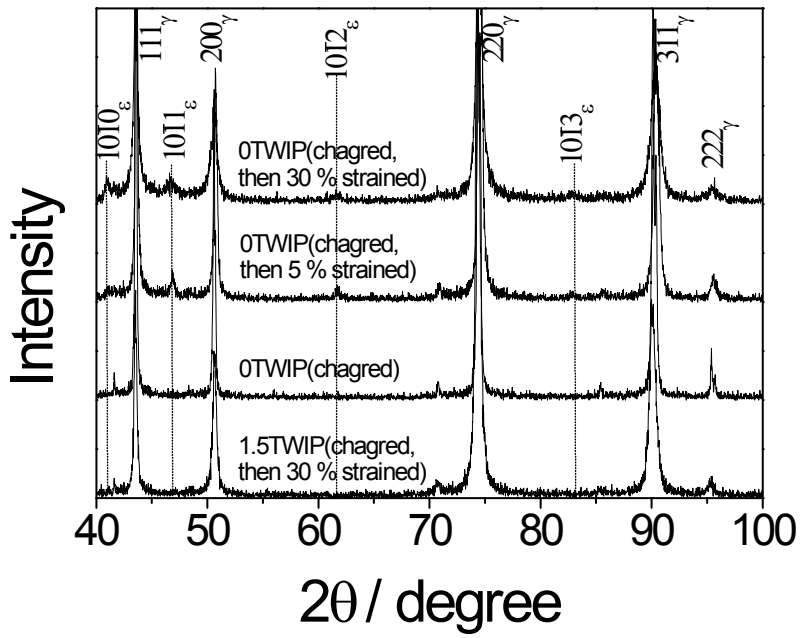

Fig. 4.18: XRD results for samples pre-charged at 1 A m^{-2} for 72 h, and then strained.

The ε martensitic transformation can be interpreted on the assumption that the hydrogen lowers the SFE of austenite. Whiteman and Troiano (1964) reported the reduction of SFE caused by hydrogen with TEM measurements on 310 stainless

steel. Pontini and Hermida (1997) measured by XRD a reduction of 37 % of SFE in the presence of 274 ppmw hydrogen at room temperature for 304 stainless steel. One possibility for the reduction of SFE is formation of H-H pairs during faulting (Moro *et al*., 1998; Hermida and Roviglione, 1998).

The reported SFEs for 0TWIP and 1.5TWIP are 19 and 28 mJ m^{-2} respectively; increment of the SFE by adding 1wt % Al is approximately 8.84 mJ m^{-2} (Jeong *et al*., 2012). Frommeyer *et al*. (2003) indicated that the SFEs smaller than 16 mJ m^{-2} results in the ε martensitic transformation instead of mechanical twinning during the deformation. Thus, the decrease of SFE in 0TWIP with the surface hydrogen concentration of 18 ppmw as shown in Fig. 4.12a is larger than 0.17 mJ m^{-2} $ppmw^{-1}$, but less than 0.5 mJ m^{-2} $ppmw^{-1}$ because the transformation was not observed in 1.5TWIP with the concentration of 24 ppmw.

Several investigations reported the hydrogen-induced ε martensite after the charging in unstable 304 stainless steel (Yang and Luo, 2000), stable 310 stainless steel (Narita *et al*., Minkovitz and Eliezer, 1982) and Fe-21Mn (wt %) alloy (Aikawa *et al*., 1993). Some cracks initiated and propagated through the ε martensite or along ε/γ interfaces in the alloys. Recently, Chun *et al*. (2012) investigated the effect of ε martensite on the hydrogen degradation behaviour of Fe-15Mn-2Cr-0.6C (wt%) alloy, concluding that there is an increase of degradation in proportion to the amount of ε martensite. Fig. 4.20 shows the TEM microstructure for 0TWIP sample prepared vertically to the transgranular fracture surface observed in Fig. 10b. The result indicates that the fracture occurs at the interface of ε martensite and austenite; the interface was parallel to the fracture surface. On the other hand, the result for 1.5TWIP as shown in Fig. 4.21 demonstrates that the segregation of diffusible hydrogen at mechanical twins can also result in fracture. As a consequence, adding of Al can enhance the resistance to cracking as shown in Fig. 4.22 by decreasing vulnerable sites such as not only ε martensite, but also mechanical twins, owing to an increase of SFE.

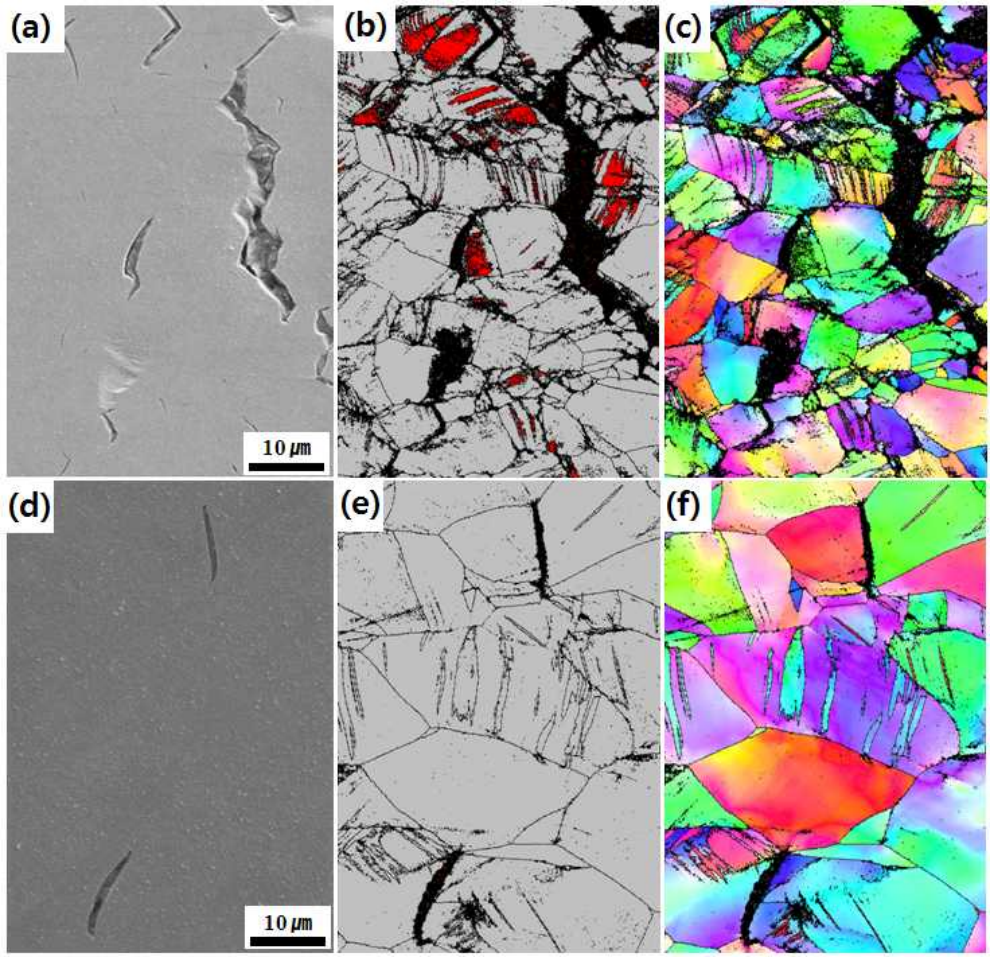

Fig. 4.19: SEM image, phase (gray: austenite, red: ε martensite, black: eliminated phase below confidence index 0.1) and inverse pole figure mapping of slightly polished surfaces of samples pre-charged, and then 30 % strained for (a,b,c) 0TWIP and those for (d,e,f) 1.5 TWIP.

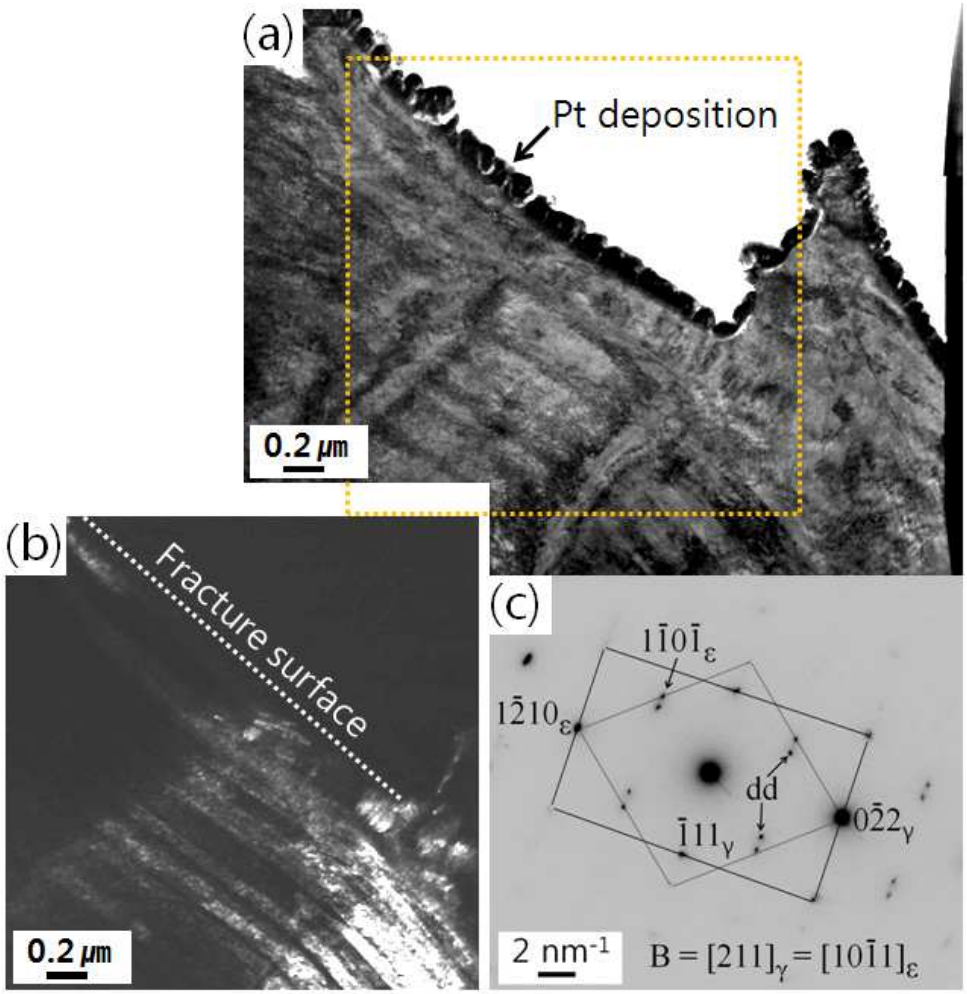

Fig. 4.20: (a) TEM micrograph for 0TWIP samples prepared vertically to the transgranular fracture surface. (b) ε martensite dark field image for the area marked with yellow line. (c) Corresponding diffraction pattern; spots not connected by lines (e.g. "dd") arise from double diffracted.

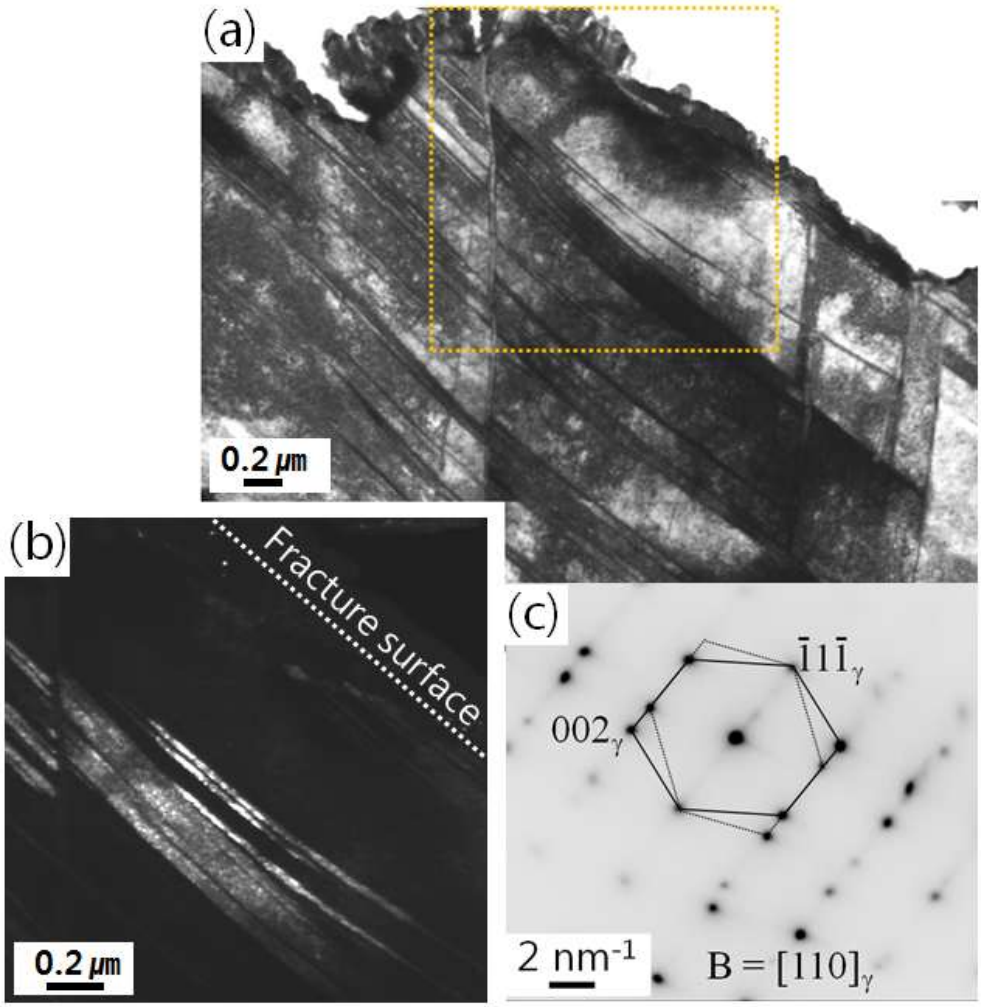

Fig. 4.21: (a) TEM micrograph for 1.5TWIP samples prepared vertically to the transgranular fracture surface. (b) Mechanical twin dark field image for the area marked with yellow line. (c) Corresponding diffraction pattern.

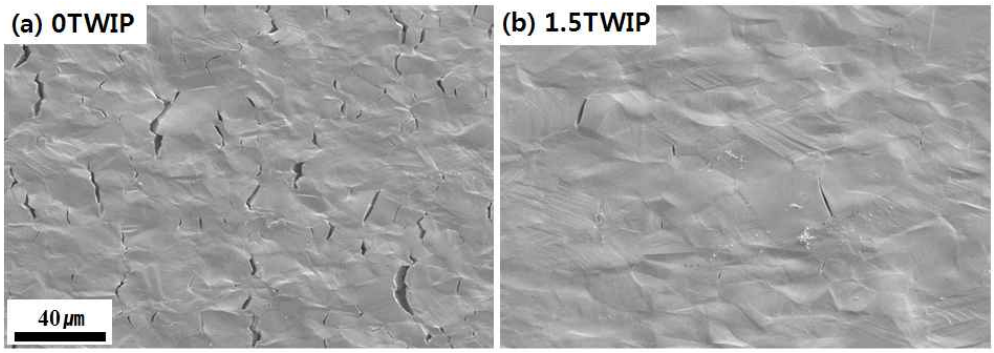

Fig. 4.22: Surface cracks of samples pre-charged at 1 A m^{-2} for 72 h, and then strained to 30%.

4.4 Summary

The mechanical degradation by hydrogen in TWIP steel has been characterized using tensile tests with dynamic hydrogen charging. The fracture surfaces show brittle intergranular and transgranular failure. This observation may be attributed to the segregation of diffusible hydrogen in grain boundaries and mechanical twins which act not only as trap sites, but also barriers for dislocation glide. Furthermore, the penetration of hydrogen increases due to transport via mobile dislocations during the tensile tests. It has also been found that ε martensite reported to be particularly susceptible to the embrittlement, forms by deformation in the hydrogen-charged steels because the hydrogen decreases stacking fault energy. The transgranular fracture surface tend to be parallel to an interface of the martensite and austenite, or mechanical twin boundaries. Thus adding of Al, which increases the stacking fault energy, in TWIP steels enhances the resistance to degradation by suppressing twinning and martensitic transformation.

Chapter 5: Conclusions

One of the important factors in the embrittlement of TRIP steels is the mechanical stability of retained austenite. It appears that the partitioning of strain between the different phases present in TRIP-assisted steels can lead to a misleading impression of the mechanical stability of retained austenite when comparisons are made between steels with substantially different microstructures, or when attempts are made to explain the stability in terms of chemical composition alone.

The desorption of hydrogen from multiphase TRIP–assisted steels with different austenite mechanical stabilities has been studied using thermal desorption analysis. The work shows that the hydrogen dissolved in austenite can be regarded as trapped given the large activation energy of diffusion, which is greater than that of generic traps found within the ferrite and martensite. As a consequence, the deformation-induced martensitic decomposition of the austenite leaves the inherited hydrogen in a more mobile state. The mechanical degradation of the steel by hydrogen is therefore more pronounced in TRIP steel containing austenite which is relatively less stable to martensitic transformation during deformation. A simple analysis has been presented of thermal desorption spectra which accounts for specimen size and can be utilised to predict quantitatively the behaviour of hydrogen in steels containing austenite and ferrite, as a function of changes in phase fractions.

The mechanical degradation by hydrogen in TWIP steel has also been characterized using tensile tests with dynamic hydrogen charging. It is discovered that the fracture surfaces reveal both intergranular and transgranular type in a brittle manner. It may be affected by segregation of diffusible hydrogen in grain boundaries and mechanical twins which act not only as trap sites but also barriers for dislocations glide, and the segregation deepens due to hydrogen transport by mobile dislocations during the tests. Furthermore, it has been found that ε martensite reported to be susceptible to the embrittlement forms by deformation in the hydrogen-charged steels because the hydrogen decreases stacking fault energy.

Transgranular fracture surfaces have been found to be parallel to the interface of the martensite and austenite, or mechanical twin boundaries. Therefore, the adding of Al, which increases the stacking fault energy, in TWIP steels enhances the resistance to degradation by suppressing twinning and martensitic transformation.

Appendix: Approach to Develop Stainless δ-TRIP Steel

A.1 Introduction

Transformation-induced plasticity (TRIP) assisted steels contain allotriomorphic ferrite as the major phase, with the rest of the microstructure consisting of carbide free bainitic ferrite and carbon enriched retained austenite. An unconventional TRIP assisted steels has recently been invented, designated δ-TRIP (Chatterjee *et al*., 2007), because the usual allotriomorphic ferrite grains are replaced by δ-ferrite, which grows from the liquid steel and persists at all temperature in the solid state. Otherwise, the residual microstructure is still the same, consisting of a mixture of bainitic ferrite with enriched austenite. The steel has interesting properties: an ultimate tensile strength in the as-cast condition of about 1000 MPa and a total elongation, almost all of which is uniform, of 23 %. It has been demonstrated that the combination of strength and ductility is due partly to the deformation induced transformation of the retained austenite into martensite, resulting in an enhanced resistance to plastic instabilities (Chatterjee *et al*., 2007). The alloy contains 2 wt% Al, which is known to retard the precipitation of cementite during the bainite reaction (Langer 1968; Bhat 1977) and also helps to ensure the presence of δ-ferrite during the solidification phase (Yi *et al*., 2010).

The aim of this work was to produce a stainless δ-TRIP steel. The stainless character occurs when a concentration of Cr, which also stabilizes the δ-ferrite, exceeds about 12 wt%. Duplex stainless steel consists of 50 % of the δ-ferrite and remanent austenite; the latter can persist by adding of about 5 wt% Ni. In this work, the bainitic transformation was introduced to stabilise the carbon enriched austenite rather than alloying, which allows the TRIP.

A.2 Alloy Design and Manufacture

The presence of δ-ferrite is crucial in this stainless δ-TRIP steel concept. The fraction of phases as a function of temperature in both equilibrium and

paraequilibrium, therefore, were calculated to design stable δ-ferrite using MTDATA (2005) in combination with the TCFE (version 1.21) database. Liquid, ferrite, austenite, M_7C_3, $M_{23}C_6$, and cementite were allowed coexist under equilibrium but M_7C_3, $M_{23}C_6$, and cementite was omitted in the case of paraequilibrium due to a lack of appropriate thermodynamic data.

Three alloys were manufactured with increasing carbon concentration; the compositions are listed in Table A.1. Alloy2 and Alloy3 contain a larger content of Al than the Alloy1 to replace Si which prevents a precipitation of cementite during bainite reaction (Kozeschnik and Bhadeshia, 2008) but raises surface quality and galvanizing problems (Jacques *et al*., 2001; Kizu *et al*., 2001). Other solutes of Ni and Mn were included to control the amount of phases. The 34 kg ingots of 100×170×230 mm dimensions were cast in a vacuum furnace in POSCO.

Table A.1: Design compositions in wt% and those achieved during manufacture.

Alloys		C	Mn	Si	Al	Cr	Ni
Alloy1	Design	0.13	1	1.5	0.7	12	0
	Actual	0.13	1.02	1.49	0.74	12	0
Alloy2	Design	0.15	1	0.7	1.4	12	1
	Actual	0.15	1.03	0.69	1.32	11.9	1.02
Alloy3	Design	0.2	1.5	0.8	1.5	12	1
	Actual	0.18	1.5	0.79	1.45	12	1.01

The calculated equilibrium phase diagrams for the manufactured alloys are presented in Fig. A.1; they show that the minimum amount of δ-ferrite to be expected in the microstructure is 57, 66 and 63 wt% for Alloy1, Alloy2 and Alloy3 under equilibrium condition. The alloys start solidification with δ-ferrite which remains the only solid phase until the liquid has been consumed completely. Austenite continues to grow in proportion by consuming the δ-ferrite on cooling.

After the amount of ferrite reaches the minimum, the austenite starts to transform in ferrite again, which, however, was a different morphology when compared with the δ-ferrite.

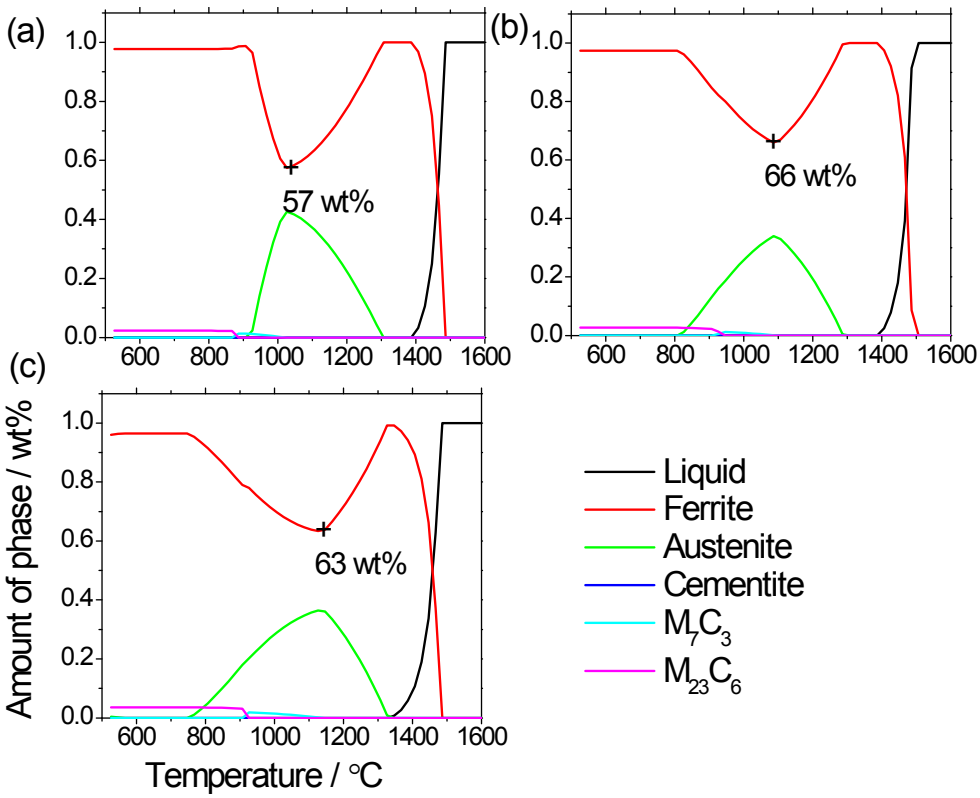

Fig. A.1: Calculated phase percentages as a function of temperature in equilibrium. (a) Alloy1. (b) Alloy2. (c) Alloy3.

A.3 Experimental

Optical microscopy samples were mechanically polished and then etched with a mixture of 1 g picric acid + 100 ml ethanol + 10 ml HCl. Higher resolution observations were done using field emission gun scanning electron microscope equipped with an electron back-scattered diffraction facility. In the latter case the specimens were finally mechanically polished with a colloidal silica suspension and the step size was 0.5 μm. The phases were determined using X-ray diffraction with

CuK_α radiation. Microhardness was measured with a Vickers hardness tester by using 300 gf loading and 10 s holding time. Thin foils for transmission electron microscopy were mechanically polished to a thickness of 80 μm and then electrolytically polished in a twin-jet polishing apparatus using a solution containing 10 % $HClO_4 + C_2H_5OH$.

Microstructure evolution simulations were conducted using a push-rod BAHR DIL805 high-speed dilatometer with radio frequency induction heating. Cylindrical dilatometric samples of diameter 5 mm and length 10 mm were used. The experiments were done in vacuum or argon atmosphere.

To investigate about effect of grain refinement on bainitic transformation, the as-cast of Alloy1 with 30 mm thick was reheated to 1200 ℃ for 1 h and hot-rolled to 3 mm in thickness with a finishing temperature above 900 ℃.

A.4 As-cast Microstructures

Fig. A.2 shows the microstructures of alloys in as-cast condition, consisting of δ-ferrite and dendritic martensite resulting from the solid-state transformation of austenite. Table A.2 shows microhardness for the δ-ferrite and martensite in the alloys. XRD results in Fig. A.3 confirms that the microstructures are fully ferritic. Total amounts of the δ-ferrite are 55 ± 3.3, 27 ± 3.3, 24 ± 3.3 vol. % for the Alloy1, Alloy2 and Alloy3 respectively, as determined by measuring point fractions; the amounts are consistent with weight percentage since the difference in density between ferrite and austenite is ignored. The amounts for Alloy2 and Alloy3 are quite inconsistent with the phase calculations in Fig. A.1. Yi *et al*. (2010) reported much reduced fractions of the ferrite in as-cast microstructure of δ-TRIP steel due to non-equilibrium solidification. However, the observed amounts for Alloy2 and Alloy3 also are much lower than the minimum amounts to be expected under paraequilibrium condition as shown in Fig. A.4.

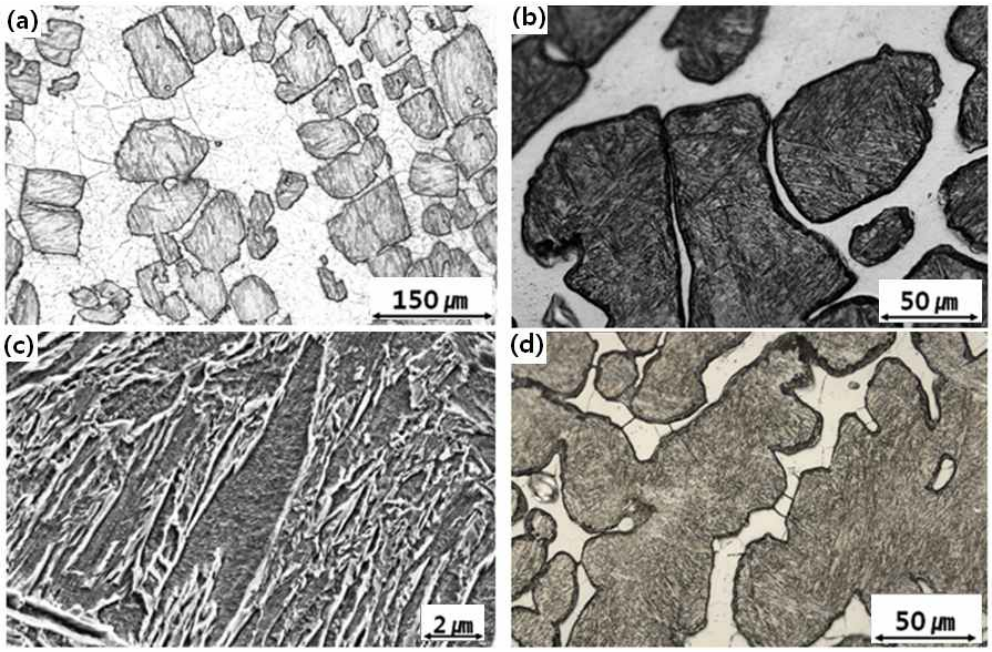

Fig. A.2: Microstructure of as-cast for (a) Alloy1, (b) Alloy2 and (d) Alloy3; the dark regions are martensite and the bright, δ-ferrite. (c) Higher magnification image of the dark area of Alloy2 showing martensite.

Table A.2: Microhardness of δ-ferrite and martensite in alloys.

	Microhardness (HV0.3 kgf)	
	δ-ferrite	Martensite
Alloy1	185±12	506±66
Alloy2	196±18	458±24
Alloy3	190±21	468±28

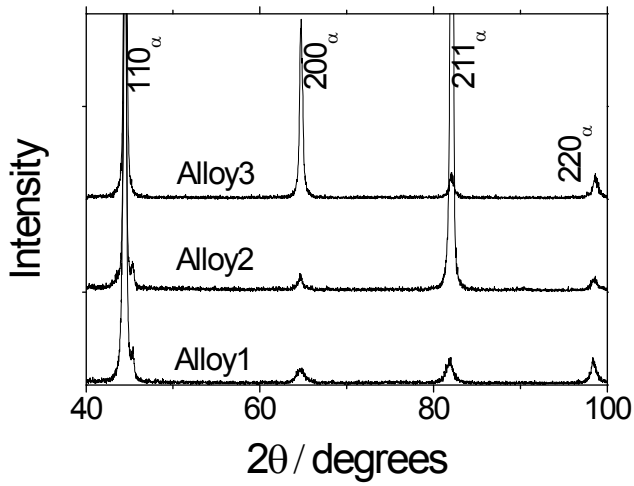

Fig. A.3: XRD results for as-cast alloys

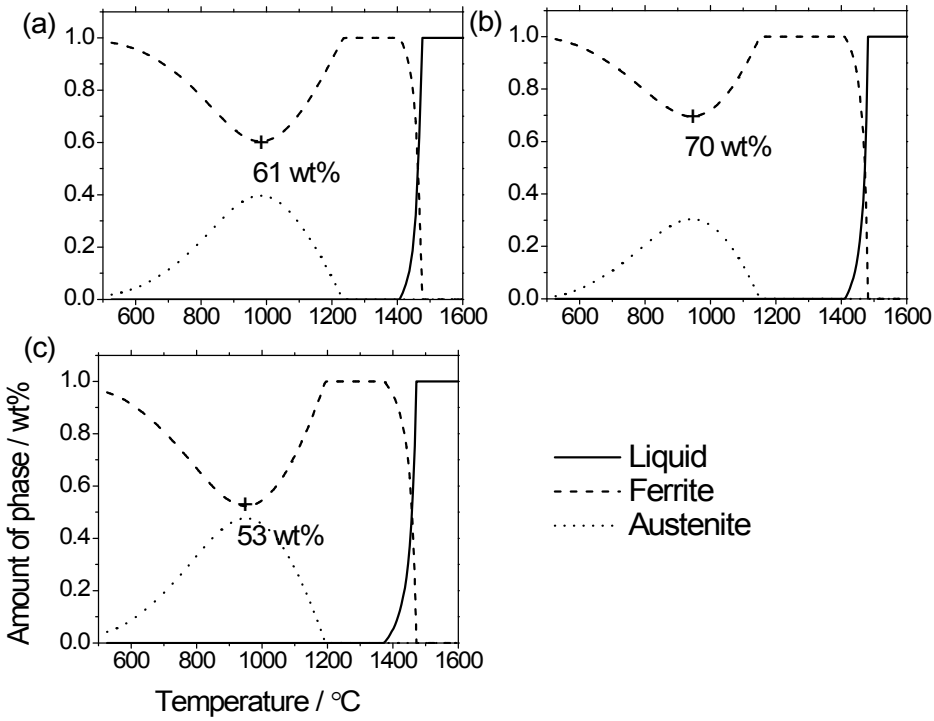

Fig. A.4: Calculated phase percentages for (a) Alloy1, (b) Alloy2 and (c) Alloy3 as a function of temperature in paraequilibrium.

A.5 Bainitic Transformation

A dilatometer was used for investigating transformation behaviour. The heating and cooling rate were 5 and 20 ℃ s^{-1}. Intercritical annealing was done at different temperatures for 3 min. Martensite-start temperature M_S were measured using a dilatometer with the data analysed using the offset method (Yang and Bhadeshia, 2007). The dilatometric curves presented in Fig. A.5a show the martensitic transformation for Alloy3 with the annealing temperatures. The measured M_s of

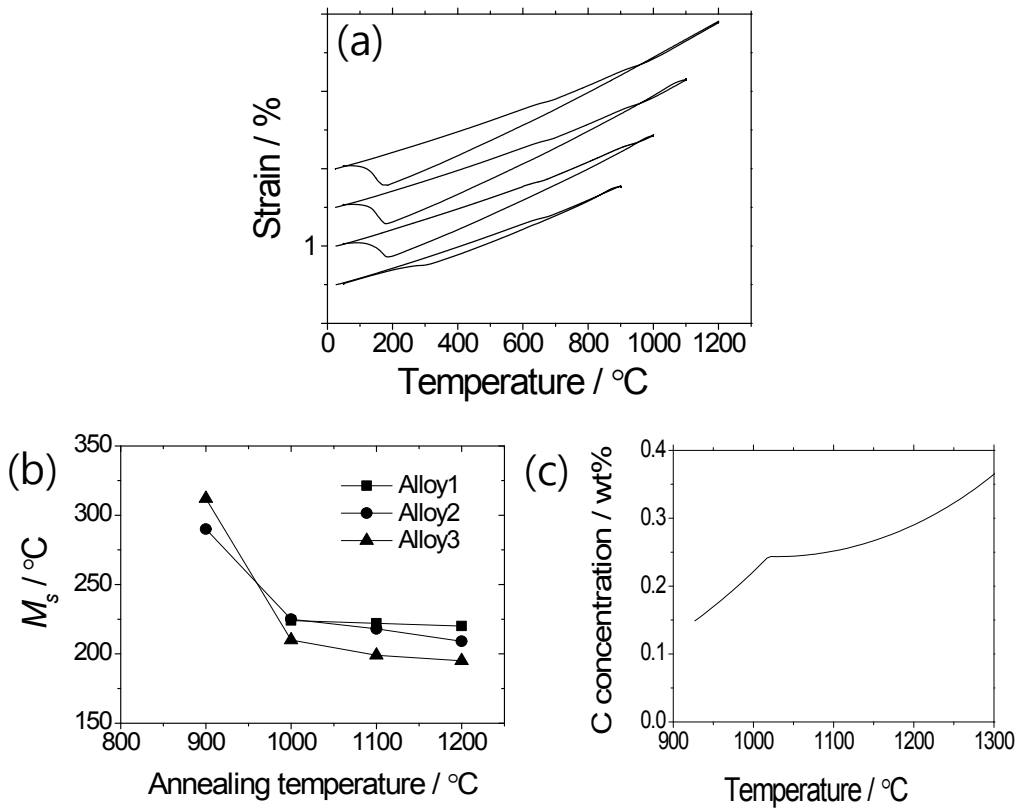

Fig. A.5: (a) Dilatometric curves which show martensitic transformation for Alloy3 with different annealing temperatures. (b) Martensite start temperature M_s of alloys *vs* the annealing temperature. (c) Carbon concentration of austenite in Alloy1 as a function of the temperature.

alloys increase when the annealing temperature decreases (Fig. A.5b), because calculated carbon concentration in austenite decreases due to carbide precipitation at below 1000 ℃ (Fig. A.5c). The microstructures after the annealing are shown in Fig. A.6, which reveals that the amounts of δ-ferrite are almost simillar with those in as-cast.

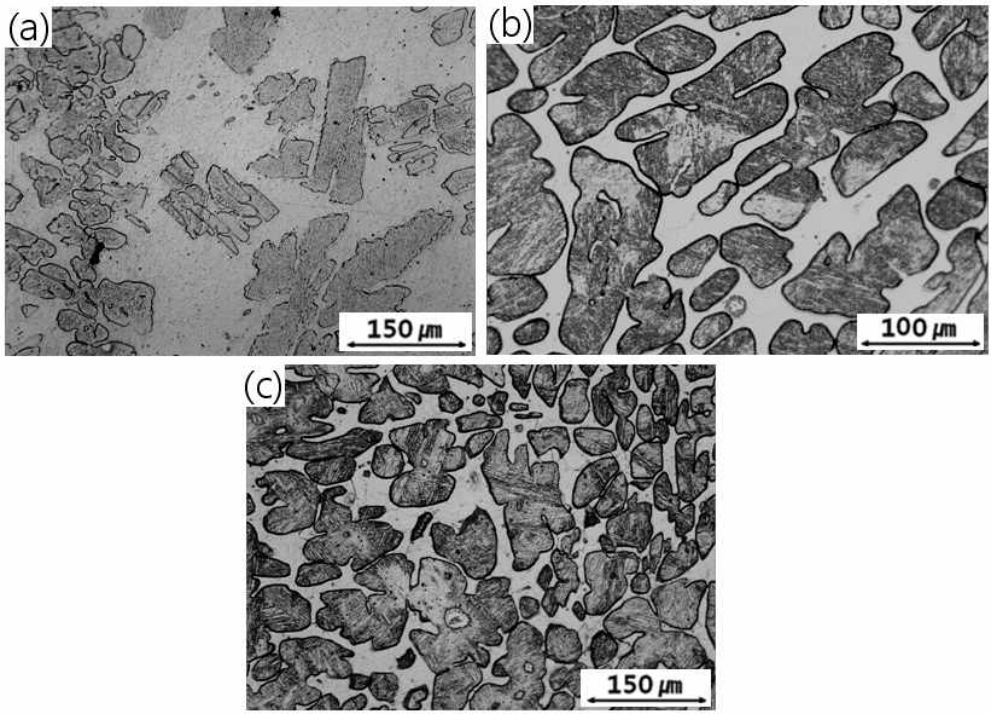

Fig. A.6: Microstructures of (a) Alloy1, (b) Alloy2 and (d) Alloy3 annealed at 1100 ℃ for 3 min using dilatometer.

Using the dilatometer, Alloy1 was austempered for 1 hour after the intercritical annealing at 1100 ℃. However, the results presented in Fig. A.7 indicate that bainitic transformation doesn't occur within the austempering time at different temperatures above M_s. Simillar experiments for Alloy2 and Alloy3 also revealed no bainitic transformation even though the time was increased to 20 h for Alloy3 (Fig. A.8).

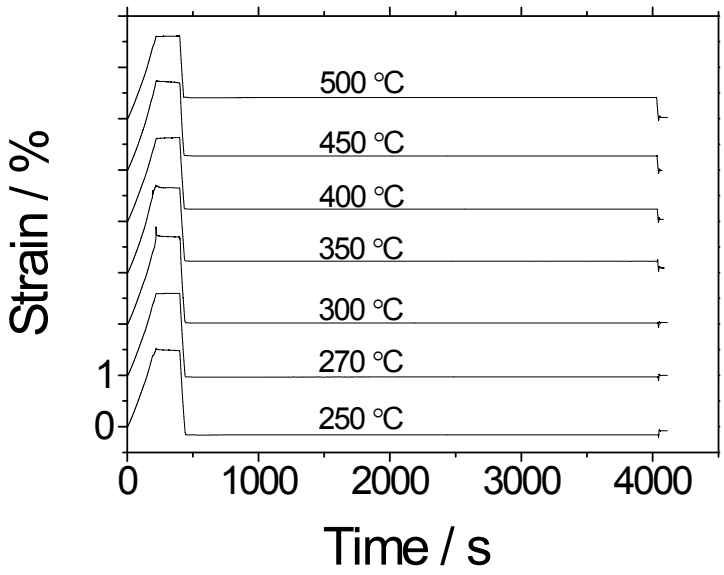

Fig. A.7: Dilatometric curves for Alloy1 annealed at 1100 ℃ for 3 min, and then austempered at different temperatures for 1 h.

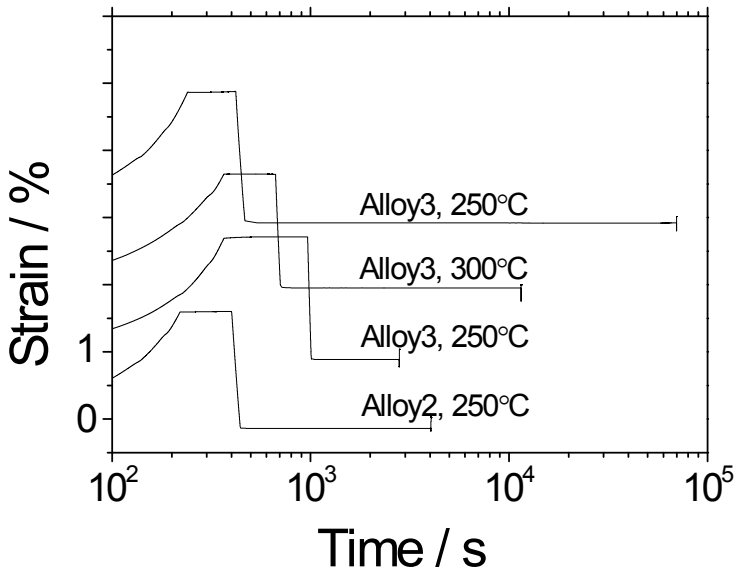

Fig. A.8: Dilatometric curves for Alloy2 and Alloy3 which were annealed at 1100 ℃, and then austempered at different temperatures.

Thus, the alloys were austempered for longer time using two furnaces; samples were annealed for 1 h in evacuated quartz capsules, and then austempered for 12 days at 250 ℃ in the other furnace after breaking the capsules. In this case, the annealing was done at an elevated temperature of 1200 ℃ to increase the carbon concentration in austenite by reducing the fraction of austenite. Fig. A.9 shows microstructures of the alloys water-quenched after the austempering.

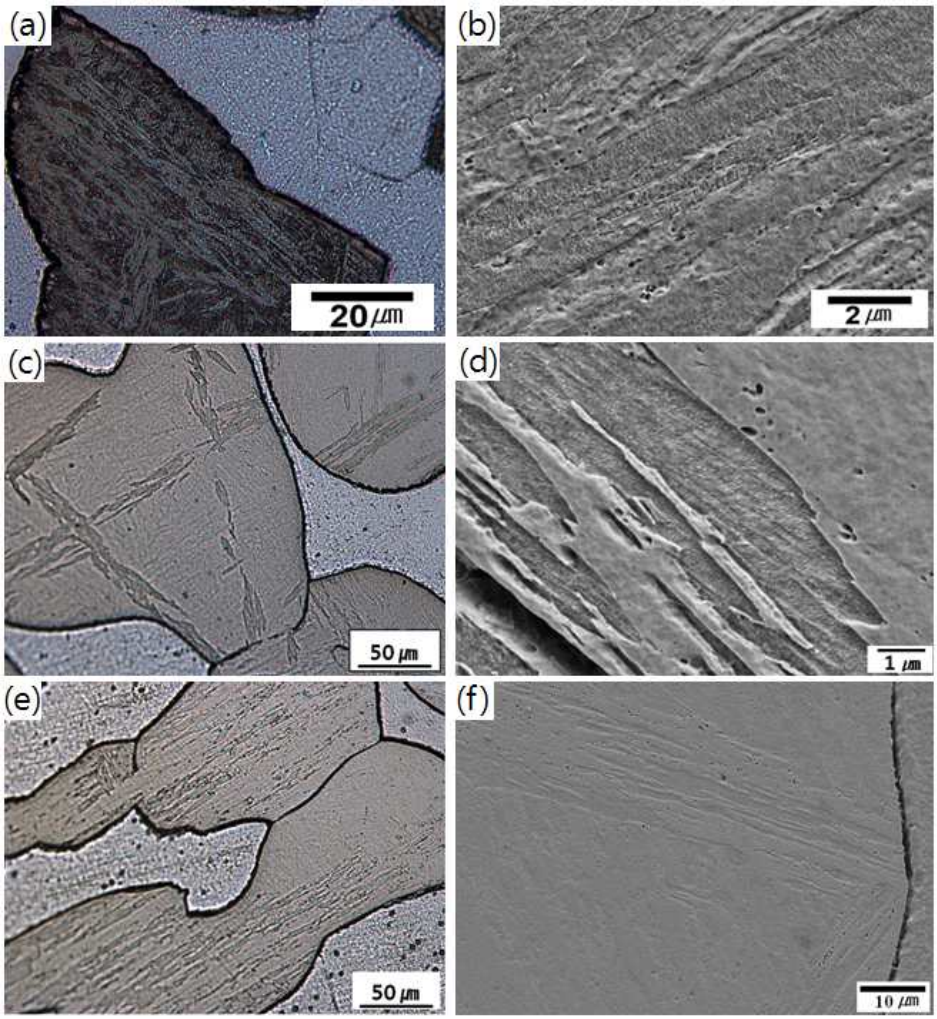

Fig. A.9: Optical and SEM images for (a,b) Alloy1, (b,c) Alloy2 and (e,f) Alloy3 annealed for 1 h at 1100 ℃, and then austempered for 12 days at 250 ℃.

Alloy2 shows clearly different microstructures after etching; etched-microstructures are bainitic sheaves which consit of bainitic plates and grow from grain boundaries, and remnant is martensite. Alloy1 and Alloy3 also show simillar microstructures. However, the retained austenite was not observed in the alloys as shwon in Fig. A.10. It is because because carbon enrichment in residual austenite after the partial bainitic transformation was not enough to make it stable to room temperature, which results in the martensite.

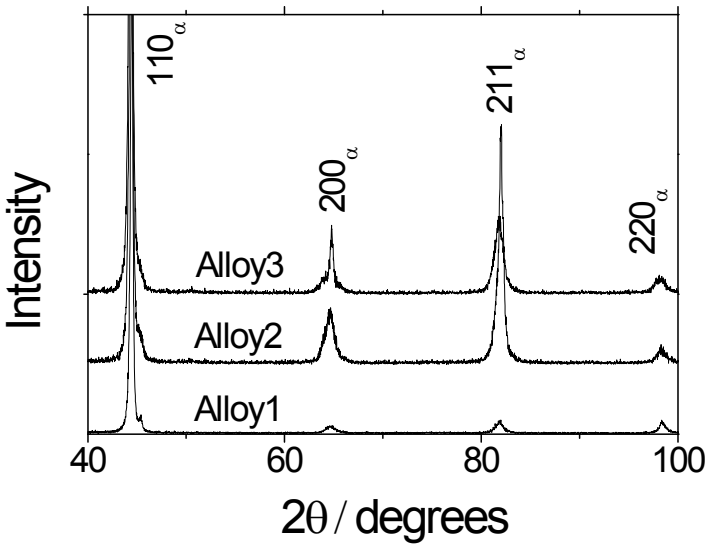

Fig. A.10: XRD results for the alloys annealed and austempered using furnaces.

A.6 Effect of Hot-Rolling

The previous results indicate that the rate of bainitic transformation is quite slow in these alloys, which might cause insufficient carbon partitioning into the residual austenite. One of the affecting parameters is the prior austenite grain size. Grain refinement by hot-rolling can increase the number density of grain nucleation sites, and thus accelerate the bainitic transformation dramatically in a steel where the

growth rate of bainite is small and thus nucleation is the dominant parameter for kinetics (Matsuzaki and Bhadeshia, 1999). Alloy1 was appropriate for hot-rolling because its microstructure contains the largest fraction of δ-ferrite after intercritical annealing, which is quite consistent with the thermodynamic calculations. The alloy also shows the biggest driving force for the diffusionless growth of bainite at same transformation temperature with the intercritical annealing at 1200 ℃ as shown in Fig. A.11.

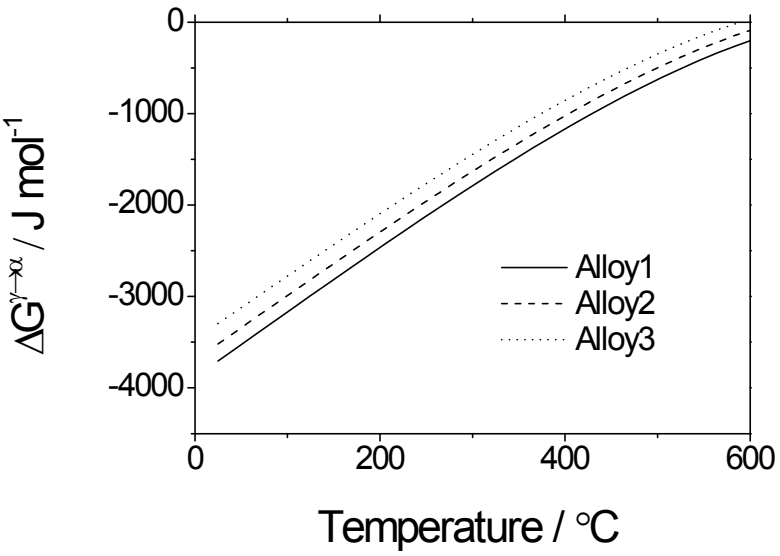

Fig. A.11: Chemical driving force $\Delta G^{\gamma\rightarrow\alpha}$ for diffusionless growth of bainite.

Fig. A.12a shows the hot-rolled microstructure which still contains the δ-ferrite. The M_s temperature was measured to be 203 ℃, which was about 17 ℃ lower than that of as-cast, with the annealing at 1200 ℃ for 3 min using dilatometer (Fig.A.12b). Then, the hot-rolled samples were austempered at 250 ℃ for 5, 9 and 12 days after the annealing at 1200 ℃ for 3 min using furnaces. However, retained austenite was not observed after the austempering as shown in Fig. A.13.

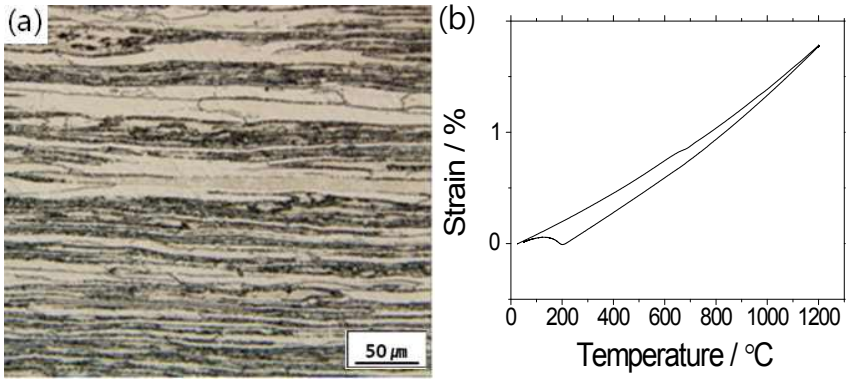

Fig. A.12: (a) Optical microstructure of hot-rolled sample for Alloy1, which contains the δ-ferrite (bright area). (b) Dilatometric curve for the sample.

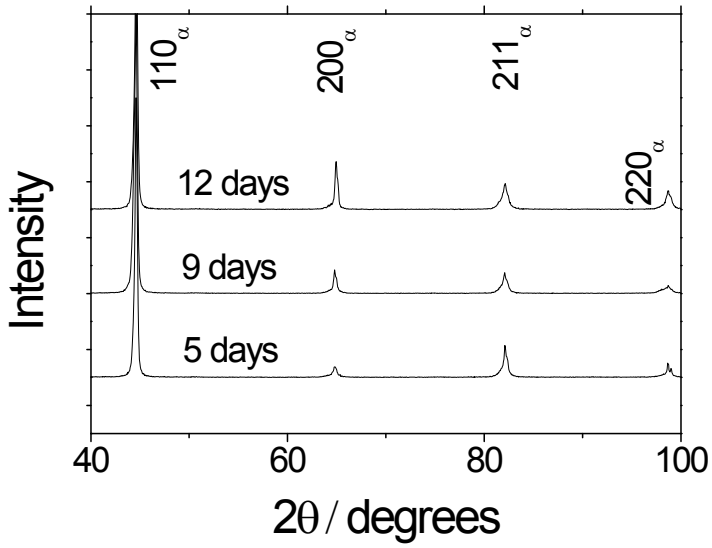

Fig. A.13: XRD results for Alloy1 hot-rolled, annealed and austempered for different times at 250 ℃ using furnaces

Fig. A.14 compares the microstructures between samples which were annealed and austempered for 12 days with and without hot-rolling. The grain size of the prior austenite were reduced only a factor of about 3 times by rolling because of the high

annealing temperature, which might give a small effect on the acceleration of bainitic transformation. Thus, the absence of retained austenite may be attributed to insufficient carbon partitioning. Furthermore, $Cr_{23}C_6$ carbide, which decreases the carbon concentration in austenite, was observed on grain boundaries (Fig. A.15) even though the annealing temperature was sufficiently higher than the calculated dissolution temperature for the carbide. Consequently, the samples exhibited poor tensile properties with a brittle fracture by cleavage as shown in Fig. A.16.

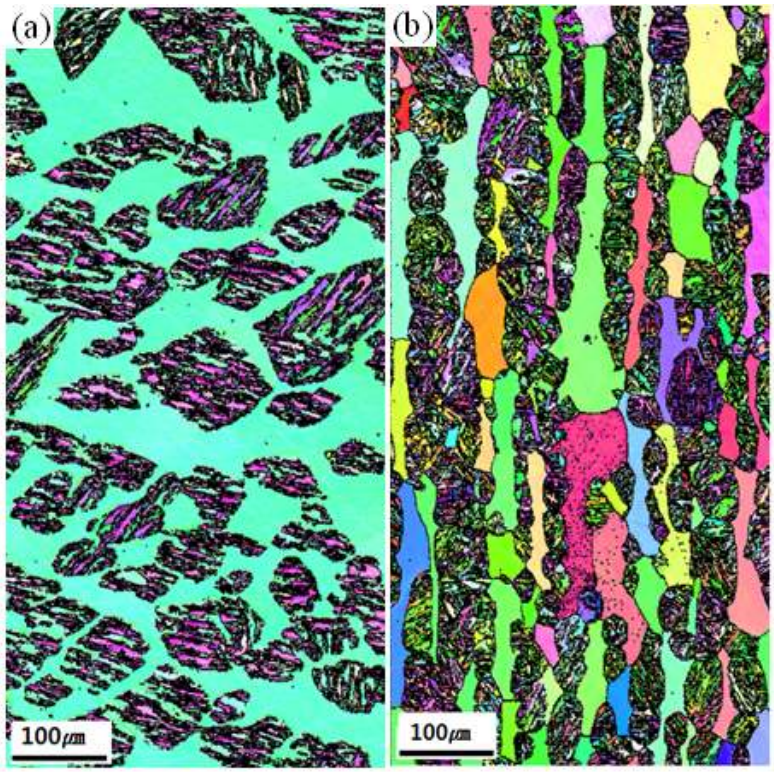

Fig. A.14: Inverse pole figure mapping of Alloy1 samples annealed and austempered (a) with and (b) without hot-rolling.

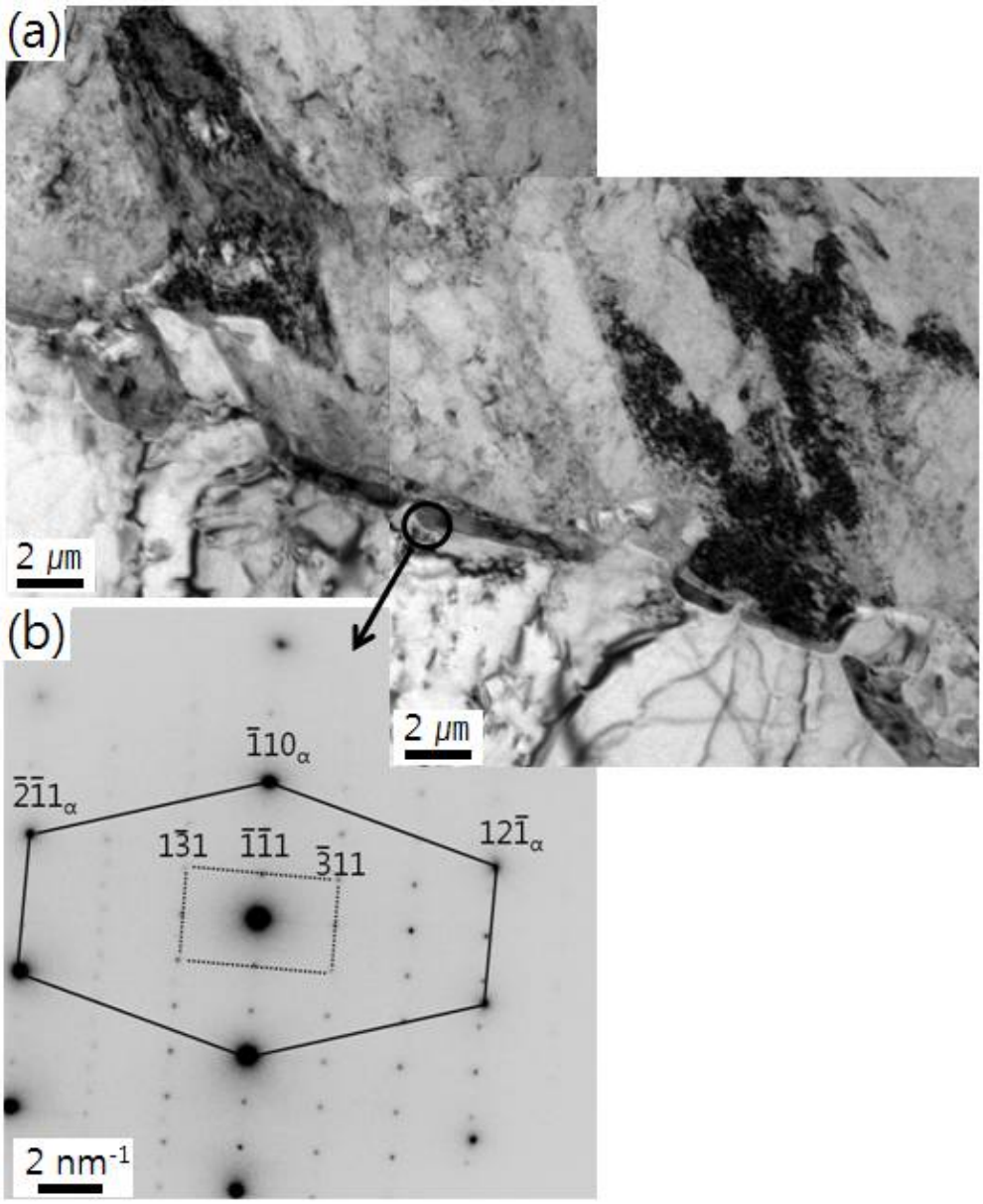

Fig. A.15: (a) TEM micrograph for Alloy1 hot-rolled, annealed and austempered for 12 days at 250 ℃. (b) Diffraction pattern for grain boundary region, B = $[113]_\alpha = [112]_{Cr_{23}C_6}$.

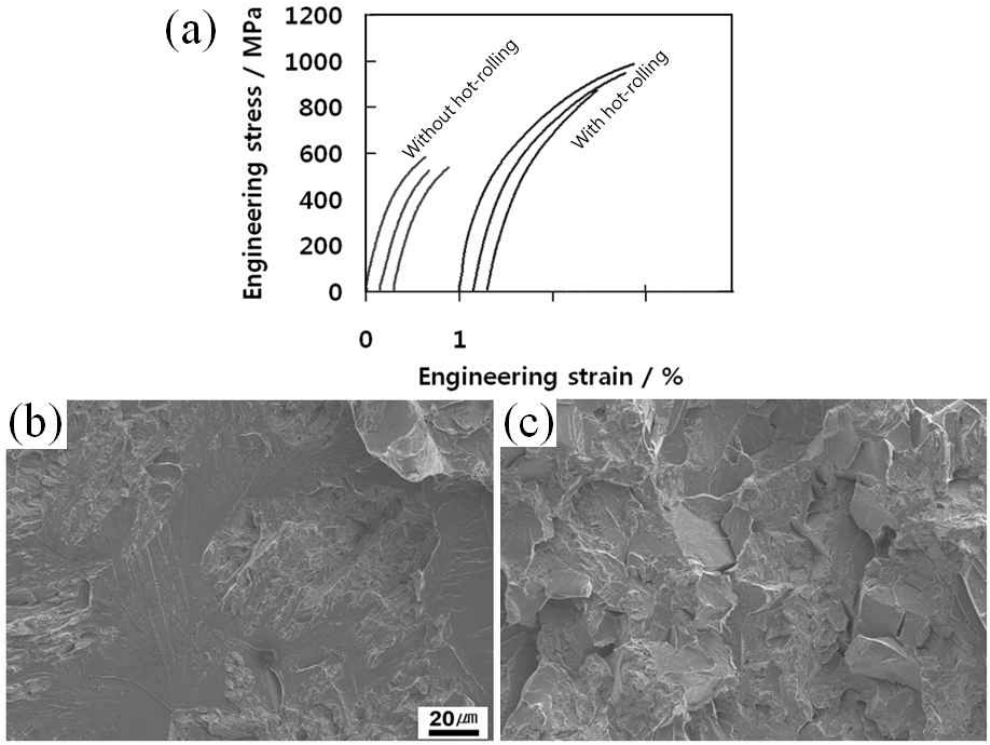

Fig. A.16: (a) Stress-strain curves at a strain rate of 0.001 s^{-1} for Alloy1 samples annealed and austempered with and without hot-rolling. Fracture surface of sample annealed and austempered (b) without and (c) with hot-rolling

A.7 Summary

The work presented in this chapter aimed to develop stainless δ-TRIP steel. Several difficulties were observed for the work. One of them is that some produced amounts of δ-ferrite in as-cast condition were lower than those expected in both equilibrium and paraequilibrium. The diminished quantity lowers the carbon concentration in austenite at intercritical annealing temperature. Another problem is the high intercritical annealing temperature to avoid carbide precipitation. The high temperature allows the fast coarsening of austenite grain and reduces the effect of grain refinement by hot-rolling on the rate of bainitic transformation. Furthermore, $Cr_{23}C_6$ carbides were observed even though the temperature was 100 ℃ higher than a dissolution temperature for carbide. Eventually, reduced amount of δ-ferrite, slow bainitic transformation and carbide precipitation are responsible for the absence of retained austenite.

References

Adler, P. H., Olson, G.B., Owen, W. S.: Strain hardening of Hadfield manganese steel. *Metallurgical Transactions A*, Vol. 17 (1986) pp. 1725–1737

Aikawa, T., Nishino, Y., Asano, S.: Stabilization of the HCP ε phase in an Fe21%Mn alloy subjected to cathodic hydrogen charging. *Scripta Metallurgica*, Vol. 29 (1993) pp. 135-137

Allain, S., Chateau, J.P., Bouaziz, O., Migot, S., Guelton, N.: Correlations between the calculated stacking fault energy and the plasticity mechanisms in Fe–Mn–C alloys. *Materials Science and Engineering A*, Vol. 387 (2004) pp. 158-162

Andreone, C. and Murut, A.: Influence of the austenite retained in the hydrogen embrittlement in AISI 4340, *Scripta Metallurgica*, Vol. 24 (1990) pp. 1453-1458

Asgari, S., El Danaf, E., Kalidindi, S. R., Doherty, R. D.: Strain hardening regimes and microstructural evolutions during large strain compression of low stacking fault energy fcc alloys that form deformation twins. *Metallurgical and Materials Transactions A*, Vol. 28 (1997) pp.1781–1795

Asano, S. and Otsuka, R.: The lattice hardening due to dissolved hydrogen in iron and steel. *Scripta Metallurgica*, Vol. 10 (1976) pp. 1015–1020

Bai, D. Q., Chiro, A. D., Yue, S.: Stability of retained austenite in a Nb microalloyed Mn-Si TRIP steel. *Materials Science Forum*, Vol. 284–286 (1998) pp. 253–260

Beachem, C. D.: A new model for hydrogen-assisted cracking (hydrogen

"embrittlement"). *Metallurgical Transactions A*, Vol. 3 (1972) pp. 437-451

Bentley, A. P. and Smith, G. C.: Phase transformation of austenitic stainless steels as a result of cathodic hydrogen charging. *Metallurgical Transactions A*, Vol. 17 (1986) pp. 1593-1600

Bernstein, I. M.: The Role of Hydrogen in the Embrittlement of Iron and Steel, *Materials and Science and Engineering*, Vol.6 (1970) pp. 1-19

Bhadeshia, H. K. D. H. and Edmonds, D. V.: Bainite in silicon steels: New composition-property approach. Part 1. *Metal Science*, Vol. 17 (1983) pp. 411–419

Bhadeshia, H. K. D. H.: Steels for bearings. *Progress in Materials Science*, Vol. 57 (2012) pp. 268–435

Bhat, M. S.: Microstructure and mechanical properties of AISI 4340 Steel modified with Al and Si. PhD thesis, Lawrence Berkley Laboratories, California, USA, 1977

Birnbaum, H. K. and Sofronis, P.: Hydrogen-enhanced localized plasticity-a mechanism for hydrogen-related fracture. *Materials Science and Engineering A*, Vol. 176 (1994) pp. 191-202

Bouaziz, O., Allain, S., Scott, C. P., Cugy, P. and Barbier, D.: High manganese austenitic twinning induced plasticity steels: A review of the microstructure properties relationships. *Current Opinion in Solid State and Materials Science*, Vol. 15 (2011) pp. 141–168

Bouaziz, O., Allain, S., Scott, C.: Effect of grain and twin boundaries on the hardening mechanisms of twinning-induced plasticity steels. *Scripta Materialia*, Vol. 58 (2008) pp. 484–487

Chan, S. L. I., Lee, H. L., Yang, J. R.: Effect of retained austenite on the hydrogen content and effective diffusivity of martensitic structure, *Metallurgical Transactions A*, Vol. 22 (1991) pp. 2579-2586

Chatterjee, S., Murugananth, M. and Bhadeshia, H. K. D. H.: δ-TRIP Steel. *Materials Science and Technology*, Vol. 23 (2007) pp. 819-827

Chin, K. G., Kang, C. Y., Shin, S. Y., Hong, S. K., Lee, S. H., Kim, H. S., Kim, K. H., Kim, N. J.: Effects of Al addition on deformation and fracture mechanisms in two high manganese TWIP steels. *Materials Science and Engineering A*, Vol. 528 (2011) pp. 2922–2928

Chornet, E. and Coughlin, R. W.: Chemisorption of hydrogen on iron. *Journal of Catalysis*, Vol. 72 (1972) pp. 246-265

Choo, W. Y. and Lee, J. Y.: Thermal analysis of trapped hydrogen in pure iron. *Metallurgical Transactions A*, Vol. 13 (1982) pp. 135–140

Chun, Y. S., Kim, J. S., Park, K. T., Lee, Y. K., Lee, C. S.: Role of ε martensite in tensile properties and hydrogen degradation of high-Mn steels. *Materials Science and Engineering A*, Vol. 533 (2012) pp. 87-95

Chun, Y.S., Park, K.T., Lee, C.S.: Delayed static failure of twinning-induced plasticity steels. *Scripta Materialia*, in presss

Cuitino, A. M. and Ortiz, M.: Ductile fracture by vacancy condensation in f.c.c. single crystals. *Acta Materialia*, Vol. 44 (1996) pp. 427-436

Darken, L. S. and Smith, R. P.: Behavior of hydrogen in steel during and after

immersion in acid. *Corrosion*, Vol. 5 (1949) pp.1-16

Dayal, R. K. and Parvathavarthini, N.: Hydrogen embrittlement in power plant steels. *Sadhana*, Vol. 28 (2003) pp. 431-451

De Cooman, B. C.: Structure-properties relationship in TRIP steels containing carbide-free bainite. *Current Opinion in Solid State and Materials Science*, Vol. 8 (2004) pp. 285–303

De Cooman, B. C., Chen, L., Kim, H. S., Estrin, Y., Kim, S. K., Voswinckel, H.: State-of-the-Science of High Manganese TWIP Steels for Automotive Applications. in: Haldar, A., Suwas, S., Bhattacharjee, D. (Eds), Microstructure and Texture in Steels, Springer London, (2009) pp. 165-183

Dehoff, R. T. and Rhines, F. N.: Quantitative microscopy, McGraw Hill, New York (1968)

Donovan, J. A.: Accelerated evolution of hydrogen from metals during plastic deformation. *Metallurgical Transactions A*, Vol. 7 (1976) pp.1677-1683

Duchateau, D. and Guttmann, M.: An X-ray microanalysis study of the partition of manganese in 6 and 9% Mn cryogenic steels and its influence on the stability of austenite dispersed in a tempered martensitic matrix. *Acta Metallurgica*, Vol. 29 (1981) pp. 1291–1297

Dumay, A., Chateau, J. P., Allain, s., Migot, S., Bouaziz, O.: Influence of addition elements on the stacking-fault energy and mechanical properties of an austenitic Fe–Mn–C steel. *Materials Science and Engineering A*, Vol. 483 (2008) pp. 184–187

Duprez, L., Verbeken, K., Verhaege, M.: Effect of hydrogen on the mechanical

properties of multiphase high strength steels. in: Somerday, B., Sofronis, P., Jones, R. (Eds.), Effects of Hydrogen on Materials, ASM International, Ohio, U. S. A. (2009) pp. 62-69

Escoba, D. P., Duprez, L., Verbeken, K., Verhaege, M.: Identification of the hydrogen trap sites in a high strength TRIP steel by means of thermal desorption spectroscopy. in: Somerday, B., Sofronis, P., Jones, R. (Eds.), Effects of Hydrogen on Materials, ASM International, Ohio, U. S. A. (2009) pp. 485–492

Frommeyer, G., Brüx, U., Neumann, P.: Supra-ductile anf high-strength manganese-TRIP/TWIP steels for high energy absorption purpose. *ISIJ International*, Vol. 43 (2003) pp. 438–446

Fukai, Y. and Okuma, N.: Formation of superabundant vacancies in Pd hydride under high hydrogen pressures. *Physical Review Letters*, Vol. 73 (1994) pp. 1640-1643

Furnémont, Q., Lacroix, G., Godet, S., Conlon, K. T., Jacques, P. J.: Critical assessment of the micromechanical behaviour of dual phase and trip-assisted multiphase steels. *Canadian Metallurgical Quarterly*, Vol. 43 (2004) pp. 35–42

Garber, R. I., Bernstein, I. M., Thompson, A. W.: Effect of hydrogen on ductile fracture of spheroidized steel. *Scripta metallurgica*, Vol. 10 (1976) pp. 341-345

Gardner, R. N. and Wilsdorf, H. G. F.: Ductile fracture initiation in pure α-Fe: Part II. Microscopic observations of an initiation mechanism. *Metallurgical Transactions A*, Vol. 11 (1980) pp. 659-669

Garrison, W. M., Hyzak, J. M.: Absence of hydrogen influence on the mechanical stability of retained austenite in a 0.2C/12Cr/1Mo steel. *Metallurgical Transactions*

A, Vol. 17 (1986) pp. 1876-1877

Gerberich, W. W., Chen, Y. T., John, C.: A short-time diffusion correlation for hydrogen-induced crack growth kinetics. *Metallurgical Transactions A*, Vol. 6 (1975) pp. 1485-1498

Gibala, R. and Kumnick , J.. in: Staehle, R. W., Hochmannn, J., McCright, R. D., Slater, J. E. (Eds), Stress Corrosion Cracking and Hydrogen Embrittlement of Iron Base Alloys, NACE-5, NACE, Houston, TX, (1977) pp. 244-268

Gonzalez, O. D.: *Transactions of the Metallurgical Society, American Institute of Mining, Metallurgical and Petroleum Engineers*, Vol. 245 (1969) pp. 607-611

Gordon, J. A., Hirth, J. P., Kumar, A. M., Moody Jr., A. M.: Effects of hydrogen on the mixed mode I/III toughness of a high-purity rotor steel. *Metallurgical Transactions A*, Vol. 23 (1992) pp. 1013-1020

Gu, J. L., Chang, K. D., Fang, H. S., Bai, B. Z.: Delayed fracture properties of 1500MPa Bainite/Martensite dual-phase high strength steel and its hydrogen traps, *ISIJ International*, Vol. 42 (2002) pp. 1560-1564

Hadfield, R. A.: Hadfield's Manganese Steel, *Science*, Vol. 12 (1888) pp. 284-286

Hagi, H., Hayashi, Y., Ohtani, N.: Diffusion coefficient of hydrogen in pure iron between 230 and 300 K. *Transactions of the Japan Institute of Metals*, Vol. 20 (1979) pp. 349-357

Ham, J. O., Kim, B. G., Lee, S. H.: Measurement method of sensitivity for hydrogen embrittlement of high strength bolts. *Korean Journal of Metals and Materials*, Vol. 49 (2011) pp. 1-8

Hancock, G. G. and Johnson, H. H.: Hydrogen, oxygen, and subcritical crack growth in a high-strength steel. *Transactions of the Metallurgical Society, American Institute of Mining, Metallurgical and Petroleum Engineers*, Vol. 236 (1965) pp. 513-516

Hermida, J. D. and Roviglione, A.: Stacking fault energy decrease in austenitic stainless steel induced by hydrogen pairs formation. *Scripta Materialia*, Vol. 39 (1998) pp.1145-1149

Hilditch, T. B., Lee, S. B., Speer, J. G., Matlock, D. K.: The influence of microstructure on the trapping and diffusion of hydrogen in a low carbon steel. *SAE Technical Paper*, (2003) 2003-01-0525

Hirth, J. P.: Effect of hydrogen on the properties of iron and steel. *Metallurgical Transactions A*, Vol. 11 (1980) pp. 861-890

Hirth, J.P.: Thermodynamics of stacking faults. *Metallurgical Transactions*, Vol. 1 (1970) pp. 2367–2374

Hojo, T., Sugimoto, K. I., Mukai, Y. C., Ikeda, S. S.: Effects of aluminum on delayed fracture properties of ultra high strength low alloy TRIP-aided steels. *ISIJ international*, Vol. 48 (2008) pp. 824-829

Idrissi, H., Renard, K., Schryversa, D., Jacques, P. J.: On the relationship between the twin internal structure and the work-hardening rate of TWIP steels. *Scripta Materialia*, Vol. 63 (2010) pp. 961–964

Iyer, K. J. L.: The influence of hydrogen on the austenite to martensite transformation in a ball-bearing steel. *Materials Letters*, Vol.5 (1987) pp. 405-408

Jacques, P. J., Girault, E., Martens, A., Verlinden, B., Van Humbeeck, J, and Delannay,F.: The Developments of Cold-rolled TRIP-assisted Multiphase Steels. Low Silicon TRIP-assisted Multiphase Steels. *ISIJ International*, Vol. 41 (2001) pp. 1068-1074

Jacques, P. J.: Transformation-induced plasticity for high strength formable steels. *Current Opinion in Solid State and Materials Science*, Vol. 8 (2004) pp. 259-265

Jatczak, C. F.: Retained Austenite and Its Measurement by X-Ray Diffraction. *SAE Technical Paper Series*, 800426 (1980) pp. 1–20

Jeong, J. S., Woo, W., Oh, K. H., Kwon, S. K., Koo, Y. M.: In situ neutron diffraction study of the microstructure and tensile deformation behavior in Al-added high manganese austenitic steels. *Acta Materialia*, Vol. 60 (2012) pp. 2290-2299

Johnson, H. H. and Hirth, J. P.: Internal hydrogen supersaturation produced by dislocation transport. *Metallurgical Transactions A*, Vol.7 (1976) pp. 1543-1548

Jung, J. K., lee, O. Y., Park, Y. K., Kim, D. E., Jin, K. G.: Hydrogen embrittlement behavior of high Mn TRIP/TWIP steels. *Korean Journal of Materials Research*, Vol. 18 (2008) pp. 394-399

Jung, J. K., Kim, N. K., Yeon, Y. S., Kim, H. H., lee, O. Y.: Effect of annealing temperature and alloying elements on the mechanical properties of Fe-Mn-C TWIP steels. *Korean journal of materials research*, Vol. 20 (2010) pp. 385-391

Kang, S. G., Jung, Y. S., Jun, J. H., Lee, Y. K.: Effects of recrystallization annealing temperature on carbide precipitation, microstructure, and mechanical properties in Fe-18Mn-0.6C-1.5Al TWIP steel. *Materials Science and Engineering A*, Vol. 527 (2010) pp. 745-751

Kizu, T., Nagataki, Y., Inazumi, T. and Hosoya, Y.: Effects of chemical composition and oxidation temperature on the adhesion of scale in plain carbon steels. *ISIJ International*, Vol. 41(2001) pp. 1495-1501

Kim, J. K., Chen, L., Kim, H. S., Kim, S. K., Estrin, Y., De Cooman, B. C.: On the tensile behavior of high-manganese twinning-induced plasticity steel. *Metallurgical and Materials Transactions A*, Vol. 40 (2009) pp. 3147-3158

Kim, J. K., Lee, S. J., De Cooman, B. C.: Effect of Al on the stacking fault energy of Fe-18Mn-0.6C twinning-induced plasticity. *Scripta Materialia*, Vol. 65 (2011) pp. 363-366

Kim, J. S., Lee, Y. H., Lee, D. L., Park, K. T., Lee, C. S.: Effect of intergranular ferrite on hydrogen delayed fracture resistance of ultrahigh strength boron-added steel. *ISIJ International*, Vol. 47 (2007) pp. 913-919

Kim, Y., Kang, N., Park, Y., Choi, I., Kim, G., Kim, S., Cho, K.: Effects of the strain induced martensite transformation on the delayed fracture for Al-added TWIP Steel. *Journal of the Korean Institute of Metals and Materials*, Vol. 46 (2008) pp. 780-787

Kissinger, H. E.: Reaction kinetics in differential thermal analysis. *Analytical Chemistry*, Vol. 29 (1957) pp. 1702-1706

Kiuchi, K. and McLellan, R. B.: The solubility and diffusivity of hydrogen in well-annealed and deformed iron. *Acta Metallurgica*, Vol. 31 (1983) pp. 961-984

Koyama, M., Akiyama, E., Tsuzaki, K.: Hydrogen embrittlement in a Fe–Mn–C ternary twinning-induced plasticity steel. *Corrosion Science*, Vol. 54 (2011) pp. 1-4

Kozeschnik, E. and Bhadeshia, H. K. D. H.: Influence of silicon on cementite precipitation in steels. *Materials Science and Technology*, Vol. 24 (2008) pp. 343-347

Kumnick, A. J. and Johnson, H. H.: Deep trapping states for hydrogen in deformed iron, *Acta Metallurgica*, Vol. 28 (1980) pp. 33-39

Kumnick, A. J. and Johnson, H. H.: Hydrogen transport through annealed and deformed Armco iron. *Metallurgical Transactions B*, Vol. 5 (1974) pp.1199-1206

Kushida, T., Kuratomi, N., Kudoh, T., Matsumoto, H., Tsumura, T., Nakasato, F.: Delayed fracture and hydrogen absorption of 1.3GPa grade high strength bolt steel. *Tetsuto-Hagane*, Vol. 82 (1996) pp. 297–302

Lacombe, P., Aucouturier, M., Laurent, J. P., Passet, G. L. in: Staehle, R. W., Hochmannn, J., McCright, R. D., Slater, J. E. (Eds), Stress Corrosion Cracking and Hydrogen Embrittlement of Iron Base Alloys, NACE-5, NACE, Houston, TX, (1977) pp. 423-430

Langer, E. W.: An investigation of carbide precipitation in iron. *Metal Science*, Vol. 2 (1968) pp. 59-66

Lee, H. G. and Lee, J. Y.: Hydrogen trapping by TiC particles in iron. *Acta Metallurgica*, Vol. 32 (1984) pp.131-136

Lee, J. L. and Lee, J. Y.: Hydrogen trapping in AISI 4340 steel. *Metal Science*, Vol. 17 (1983) pp. 426-432

Lee, J. L. and Lee, J. Y.: The interaction of hydrogen with the interface of Al_2O_3 particles in iron. *Metallurgical Transactions A*, Vol. 17 (1986a) pp.2183-2186

Lee, J. Y., Lee, S. M.: Hydrogen trapping phenomena in metals with bcc and fcc crystal structures by the desorption thermal analysis technique. *Surface and Coating Technology*, Vol. 28 (1986b) pp. 301-314

Lee, S. H., Lee, S. H., Kang, S. H., Han, H. N., Oh, K. W., Lee, H. C.: An observation of micro-crack in transformation-induced plasticity-assisted multiphase steel. *ISIJ International*, Vol. 48 (2008) pp. 1394-1397

Le-Houillier, R., Begin, G., Dubé, A.: A study of the peculiarities of austenite during the formation of bainite. *Metallurgical Transactions*, Vol. 2 (1971) pp.2645–2653

Loidl, M., Kolk, O., Veith, S., Goẗbel , T.: Characterization of hydrogen embrittlement in automotive advanced high strength steels. *Materialwissenschaft und Werkstofftechnik*, Vol. 42 (2011) pp.1105–1100

Lord, A. E.: Diffusion of hydrogen in α-iron at about 120 K. *Acta Metallurgica*, Vol. 15 (1967) pp. 1241-1244

Louthan, M. R., Caskey, G. R., Donovan, J. A., Rawl, D. E.: Hydrogen embrittlement of metals. *Materials Science and Engineering*, Vol. 10 (1972) pp. 357-368

Lovicui, G., Barloscio1, M., Bottazzi, M., DAiuto, F., De Sanctis, M., Dimatteo, A., Federici, C., Maggi, S., Santus, C., Valentini, R.: Hydrogen embrittlement of advanced high strength steels for automotive use, will be published (2012)

Luppo, M. I. and Ovejero-Garcia, J.: The influence of microstructure on the trapping and diffusion of hydrogen in a low carbon steel. *Corrosion Science*, Vol. 32

(1991) pp. 1125-1136

Lynch, S. P.: Mechanisms of H-Assisted Cracking. *Metals Forum*, Vol. 12 (1979) pp.189-200

Martinez-Madrid, M., Chan, S. L. I., Charles, J. A.: Hydrogen occlusivity and embrittlement in iron – Effect of grain structure and cold work. *Materials Science and Technology*, Vol. 1 (1985) pp. 454–460

Matsumura, O., Sakuma, Y. and Takechi, H., Enhancement of elongation by retained austenite in intercritical annealed 0.4C-1.5Si-0.8Mn steel, *Transactions ISIJ*, Vol. 27 (1987) pp. 570-579

Matsunaga, H. and Noda, H.: Visualization of hydrogen diffusion in a hydrogen-enhanced fatigue crack growth in type 304 stainless steel. *Metallurgical and Materials Transactions A*, Vol. 42 (2011) pp. 2696-2705

Matsuzaki, A. and Bhadeshia, H. K. D. H.: Effect of austenite grain size and bainite morphology on the overall transformation kinetics of the bainite reaction in steels. *Materials Science and Technology*, Vol. 15 (1999) pp. 518-521

McCoy, R. A. and Gerberich, W. W.: Hydrogen embrittlement studies of a TRIP steel. *Metallurgical Transactions*, Vol. 4 (1973) pp. 539-547

McLellan, R. B. and Xu, Z. R.: Hydrogen-induced vacancies in the iron lattice. *Scripta Materialia*, Vol. 36 (1997) pp. 1201-1205

Mine, Y., Horita, Z., Murakami, Y.: Effect of hydrogen on martensitie formation in austenitic stainless steels in high-pressure torsion. *Acta Materialia*, Vol. 57 (2009) pp. 2993-3002

Mine, Y., Horita, Z., Murakami, Y.: Effect of high-pressure torsion on hydrogen trapping in Fe–0.01 mass% C and type 310S austenitic stainless steel. *Acta Materialia*, Vol. 58 (2010) pp. 649–657

Minkovitz, E. and Eliezer, E.: Phase transitions at the crack tip in type 316L stainless steel cathodically hydrogen charged. *Scripta Metallurgica*, Vol. 16 (1982) pp. 981-984

Mittal, S. C., Prasad, R. C., Deshmuk, M. B.: Effect of hydrogen on fracture of austenitic Fe-Mn-Al steel. *ISIJ International*, Vol. 34 (1994) pp. 211-216

Moro, L., Obiol, E., Roviglione, A., Hermida, D., Juan, A.: A theory of hydrogen trapping in a faulted zone of FCC iron. *Journal of Physics D: Applied Physics*, Vol. 31 (1998) pp. 893-899

MTDATA, National Physical Laboratory, Teddington, London, 2005

Murakami, Y., Kanezaki, T., Mine, Y., Matsuoka, S.: Hydrogen embrittlement mechanism in fatigue of austenitic stainless steels. *Metallurgical and Materials Transactions A*, Vol. 39 (2008) pp. 1327–1339

Nagumo, M., Nakamura, M., Takai, K.: Hydrogen thermal desorption relevant to delayed-fracture susceptibility of high-strength steels. *Metallurgical and Materials Transactions A*, Vol. 32 (2001) pp. 339-347

Nagumo, M., Yoshida, H., Shimomura, Y., Kadokura, T.: Ductile crack growth resistance in hydrogen-charged steels. *Materials Transactions*, Vol. 42 (2001) pp. 132-137

Nagumo, M.: Hydrogen related failure of Steels-a new aspect. *Materials Science and Technology*, Vol. 20 (2004) pp. 940-950

Narita, N., Altstetter, C. J., Birnbaum, H. K.: Hydrogen-related phase transformations in austenitic stainless steels. *Metallurgical Transactions A*, Vol. 13 (1982) pp. 1355-1365

Oriani, R. A.: The diffusion and trapping of hydrogen in steel. *Acta Metallurgica*, Vol. 18 (1970) pp. 147-157

Oriani, R. A. and Josephic, P. H.: Equilibrium aspects of hydrogen induced cracking of steels. *Acta Metallurgica*, Vol. 22 (1974) pp.1065–1074

Oriani, R. A. and Josephic, P. H.: Equilibrium and kinetic studies of the hydrogen-assisted cracking of steel. *Acta Metallurgica*, Vol. 25 (1977) pp. 979-988

Ovejero-garcia, J.: Hydrogen microprint technique in the study of hydrogen in steels. *Journal of Materials Science*, Vol. 20 (1985) pp. 2623-2629

Park, Y. D., Maroef, I. S., Landau, A., Olson, D. L.: Retained austenite as a hydrogen trap in steel welds, *Welding Journal*, (2002) pp. 27-35

Patel, J. R. and Cohen, M.: Criterion for the action of applied stress in the martensitic transformation, *Acta Metallurgica*, Vol. 1 (1953) pp. 531-538

Perng, T. P. and Altstetter, C. J.: Effect of deformation on hydrogen permeation in austenitic stainless steels. *Acta Metallurgica*, Vol. 34 (1986) pp.1771-1781

Petch, N. J. and Stables, P.: Delayed fracture of metals under static load. *Nature*, Vol. 169 (1952) pp. 842-843

Podgurski, H. H. and Oriani, R. A.: Nitrogenation of Fe-Al alloys. III: Absorption of hydrogen in nitrogenated Fe-Al alloys. *Metallurgical Transactions*, Vol. 3 (1972) 2055-2063

Pontini, A. E. and Hermida, J. D.: X-ray diffraction measurement of the stacking fault energy reduction induced by hydrogen in an AISI 304 steel. *Scripta Mterialia*, Vol. 37 (1997) pp. 1831-1837

Pressouyre, G. M.: A Classification of Hydrogen Traps in steel. *Metallurgical Transactions A*, Vol. 10 (1979) pp. 1571-1573

Pressouyre, G. M. and Bernstein, I. M.: A quantitative analysis of hydrogen trapping. *Metallurgical Transactions A*, Vol. 9 (1978) pp. 1571–1580

Quick, N. R. and Johnson, H. H.: Hydrogen and deuterium in iron, 49–506°C. *Acta Metallurgica*, Vol. 26 (1978) pp. 903-907

Remy, L. and Pineau, A.: Twinning and strain-induced F.C.C. → H.C.P. transformation in the Fe-Mn-Cr-C system. *Materials and Science and Engineering*, Vol. 28 (1977) pp. 99–107

Remy, L.: Kinetics of fcc deformation twinning and its relationship to stress-strain behavior. *Acta Metallurgica*, Vol. 26 (1978) pp. 443–451

Rigsbee, J. M.: A TEM investigation of hydrogen-induced deformation twinning and associated martensitic phases in 304-type stainless steel. *Journal of Materials Science*, Vol. 12 (1977) pp. 406-409

Ronevich, J. A., Speer, J. G., Matlock, D. K.: Hydrogen embrittlement of

commercially produced advanced high strength sheet steels. *SAE Technical Paper*, (2010) 2010-01-0447

Rozenak, P. and Bergman, R.: X-ray phase analysis of martensite transformations in austenitic stainless steels electrochemically charged with hydrogen. *Materials Science and Engineering A*, Vol. 437 (2006) pp. 366-378

Ryu, J. H., Kim, D. I., Kim, H. S., Bhadeshia, H. K. D. H., Suh, D. W.: Strain partitioning and mechanical stability of retained austenite. *Scripta Materialia*, Vol. 63 (2010) pp. 297–299

Sakuma, Y., Matsumura, O. and Akisue, O., Influence of C content and annealing temperature on microstructure and mechanical properties of 400°C tTransformed steel sontaining retained austenite, *ISIJ International*, Vol. 31 (1991) pp. 1348-1353

Sakaki, K., Kawase, T. Hirato, M., Mizuno, M., Araki, H., Shirai, Y., Nagumo, M.: The effect of hydrogen on vacancy generation in iron by plastic deformation. *Scripta Materialia*, Vol. 55 (2006) pp. 1031–1034

Scott, C. P. and Drillet, J.: A study of the carbon distribution in retained austenite. *Scripta Materialia*, Vol.56 (2007) pp. 489-492

Sherif, M., Garcia-Mateo, C., Sourmail, T., Bhadeshia, H. K. D. H.: Stability of retained austenite in TRIP-assisted steels, *Materials Science and Technology*, Vol 20 (2004) pp. 319–322

Shun, T. S., Wan, C. M., Byrne, J. G.: A study of work hardening in austenitic Fe-Mn-C and Fe-Mn-Al-C alloys. *Acta Metallurgica*, Vol. 40 (1992) pp. 3407–3412

Sieverts, A.: Z. The solubility of gases in metals. *Metallk*, Vol. 21 (1929) pp. 37-46

Simmons, G. W., Pao, P. S., Wei, R. P.: Fracture mechanics and surface chemistry studies of subcritical crack growth in AISI 4340 steel. *Metallurgical Transactions A*. Vol. 9 (1978) pp. 1147-1158

So, K. H., Kim, J. S., Chun, Y. S., Park, K. T., Lee, Y. G., Lee, C. S.: Eff ect of Hydrogenon Fracture of Austenitic Fe-Mn-AI Steel. *ISIJ International*, Vol.49 (2009) pp. 1952-1959

Sojka, J., Vodarek, V., Schindler, I., Ly, C., Jerome, M., Vanova, P., Ruscassier, N., Wenglorzova, A.: Effect of hydrogen on the properties and fracture characteristics of TRIP 800 steels. *Corrosion Science*, Vol. 53 (2011) pp. 2575–2581

Sugimoto, K-I., Usui, N., Kobayashi, M. and Hashimoto, S. I., Effects of Volume Fraction and Stability of Retained Austenite on Ductility of TRIP-aided Dual-phase Steels, *ISIJ International*, Vol. 32 (1992) pp. 1311-1318

Sugimoto, K. I., Misu, M., Kobayashi, M., Shirasawa, H.: Effects of second phase morphology on retained austenite morphology and tensile properties in a TRIP-aided dual-phase steel sheet, *ISIJ International*, Vol. 33 (1993) pp. 775-782

Suh, D. W., Park, S. J., Lee, T. H., Oh, C. S., Kim, S. J.: Influence of Al on the microstructural evolution and mechanical behavior of low-carbon, manganese transformation-induced-plasticity steel. *Metallurgical and Materials Transactions A*,Vol. 41 (2010) pp. 397–408

Syn, C. K., Fultz, B., Morris, J. W.: Mechanical stability of retained austenite in tempered 9Ni steel. *Metallurgical Transactions A*, Vol. 9 (1978) pp. 1635–1640

Tabata, T., Birnbaum, H. K.: Direct observation of hydrogen enhanced crack

propagation in iron, *Scripta Metallurgica*, Vol. 18 (1984) pp. 231-236

Takahashi, M. and Bhadeshia, H. K. D. H.: Model for the microstructure of some advanced bainitic steels. *Materials Transactions JIM*, Vol. 32 (1991) pp. 689–696

Takai, K. and Watanuki, R.: Hydrogen in trapping states innocuous to environmental degradation of high-strength steels. *ISIJ International*, Vol. 43 (2003) pp. 520–526

Takai, K., Shoda, H., Suzuki, H., Nagumo, M.: Lattice defects dominating hydrogen-related failure of metals. *Acta Materialia*, Vol. 56 (2008) pp. 5158–5167

Terasaki, F., Kawakami, T., Yoshikawa, A., Takano, N.: Mechanism of crack propagation due to hydrogen embrittlement in iron single crystals stressed along [001] axis. *Revue de Metallurgie Cahiers D'Informations Techniques*, Vol. 95 (1998) pp. 1519-1529

Thompson, A. W. and Bernstein, I. M.: The role of metallurgical variable in hydrogen assisted environmental fracture. *Advances in Corrosion Science and Technology*, Vol.7 (1980) pp. 53–173

Tien, J. K., Thompson, A. W., Bernstein, I. M., Richards, R. J.: Hydrogen transport by dislocations. *Metallurgical Transactions A*, Vol. 7 (1976) pp. 821-829

Tofaute, W. and Linden, K.: Transformations in solid state of manganese steels containing to 1.2% C and 17% Mn. *Arch Eisenhuttenwesen*, Vol. 10 (1936) pp. 515-519

Tomita, Y. and Okawa, T.: Effect of microstructure on mechanical properties of isothermally bainite-transformed 300M steel. *Materials Science and Engineering A*

Vol. 172 (1993) pp.145–151

Tomota, Y., Kuroki, K., Mori, T., Tamura, I.: Tensile deformation of two-ductile-phase alloys: Flow curves of α-γ FeCrNi alloys. *Materials Science and Engineering*, Vol. 24 (1976) pp. 85–94

Troiano, A. R.: The role of hydrogen and other interstitials in the mechanical behavior of metals. *Transactions ASM*, Vol. 52 (1960) pp. 54-80

Tsubakino, H., Harada, H., Yin, J.: Thermal release of hydrogen from high strength steel containing retained austenite, *ISIJ International*, Vol. 39 (1999) pp. 298-300

Turnbull, A., Hutchings, R. b.: Analysis of hydrogen atom transport in a two-phase alloy. *Materials science and Engineering A*, Vol.177 (1994) pp. 161-171

Ulmer, D. G. and Altstetter, C. J.: Hydrogen-induced strain localization and failure of austenitic stainless steels at high hydrogen concentrations. *Acta Metallurgica and Materialia*, Vol. 39 (1991) pp. 1237-1248

Ulmer, D. G. and Altstetter, C. J.: Phase relations in the hydrogen-austenite system. *Acta Metallurgica*, Vol. 41 (1993) pp. 2235-2241

Vaughan, H. G. and de Morton, M. E.: Change of hardness in steel due to hydrogen. *Nature*, Vol.177 (1956a) pp. 1225

Vaughan, H. G. and de Morton, M. E.: The influence of hydrogen on the yield-point of mild steel. *Acta Metallurgica*, Vol. 4 (1956b) pp. 224–225

Whiteman, M. B. and Troiano, A. R.: The influence of hydrogen on the stacking

fault energy of an austenitic stainless steel. *Physica Status Solidi*, Vol. 7 (1964) pp. K109–K110

Xiukui, S., Jian, X., Yiyi, L.: Hydrogen permeation behavior in metastable austenitic stainless steels 321 and 304. *Acta Metallurgica*, Vol. 37 (1989) pp. 2171-2176

Yang, H. S. and Bhadeshia, H. K. D. H.: Uncertainties in dilatometric determination of martensite start temperature. *Materials Science and Technology*, Vol. 23 (2007) pp. 556-560

Yang, H. S. and Bhadeshia, H. K. D. H., Austenite grain size and the martensite-start temperature, *Scripta Materialia*, Vol. 60 (2009) pp. 493-495

Yang, Q. and Luo, J. L.: Martensite transformation and surface cracking of hydrogen charged and outgassed type 304 stainless steel. *Materials Science and Engneering A*, Vol. 288 (2000) pp. 75-83

Yang, Q., Qaio, L. J., Chiovelli, S., Luo, L. J.: Critical hydrogen charging condtions for martensite transformation and surface cracking in TYPE 304 stainless steel. *Scripta Materialia*, Vol. 40 (1999) pp. 1209-1214

Yi, H. L., Ghosh, S. K., Liu, W. J, Lee K. Y., Bhadeshia, H. K. D. H.: Non-equilibrium solidification and ferrite in δ-TRIP steel. *Materials Science and Technology*, Vol. 26 (2010) pp. 817-823

Yurioka, N. and Suzuki, H.: Hydrogen assisted cracking in C-Mn and low alloy steel weldments. *International Materials Reviews*, Vol. 35 (1990) pp. 217–249

Zapffe, C. A. and Sims, C. E.: Hydrogen embrittlement, internal stress and defects

in steels. *Transactions of the Metallurgical Society, American Institute of Mining, Metallurgical and Petroleum Engineers*,Vol. 145 (1941) pp. 225–227

Zielinski, A., Lunarska, E., Smialowski, M.: The interaction of hydrogen atoms and dislocations in irons of different purity. *Acta Metallurgica*, Vol. 25 (1977) pp. 551-556

Acknowledgements

I would like to express my heartfelt thanks to my supervisor, Professor Bhadeshia, H. K. D. H. for his endless encouragement, and for his unique and charming way of teaching the simplicity and beauty of science. I am really thankful to Professor Dong-Woo Suh, my co-advisor, for his enthusiastic guidance, strong support and enjoyable discussion. And thanks to Professor In Gee Kim for his advise and friendship. I acknowledge POSCO for their financial support to me and establishment of GIFT.

I would like to express my thanks to Professor Chong-Soo Lee and members in his laboratory, especially Young Soo Chun, for their help.

I also would like to thank Professor Hae-Geon Lee for introducing GIFT and kind encouragement when I joined GIFT. I would like to express my sincere thanks to all the people in the GIFT, especially those members in Computational Metallurgy Laboratory (CML), for all their help and for all the memories we shared. The life with CML members was quite pleasant and enjoyable.

Finally, I wish to record my deep sense of appreciation to my parents, wife and my two daughters for their love and support during the entire period.

CURRICULUM VITAE

Name: Ryu, Joo-Hyun (류 주 현)
E-mail: windhair@potsech.ac.kr; winhair@naver.com
Date of birth: 14th April, 1980
Place of birth: Jeonnam province, South Korea

Education

Ph. D. 2012, POSTECH (Pohang, Korea), Graduate Institute of Ferrous Technology, Computational Metallurgy Group.

M. S. 2008, POSTECH (Pohang, Korea), Graduate Institute of Ferrous Technology, Computational Metallurgy Group.

B. S. 2006, POSTECH (Pohang, Korea), Department of Chemical Engineering.

Publications

Ryu, J. H. and Bhadeshia, H. K. D. H.: Contribution of microalloying to the strength of hot-rolled steels. *Materials and Manufacturing Processes*, Vol. 24 (2009) pp. 138-144

Joo, M. S., Ryu, J. H., Bhadeshia, H. K. D. H.: Domains of steels with identical properties. *Materials and Manufacturing Processes*, Vol. 24 (2009) pp. 53-58

Bhadeshia, H. K. D. H., Dimitriu, R. C., Forsik, S., Pak, J. H., Ryu, J. H.: On the performance of neural networks in materials science. *Materials Science and Technology*, Vol. 25 (2009) pp. 504-510

Ryu, J. H., Kim, D. I., Kim, H. S., Bhadeshia, H. K. D. H., Suh, D. W.: Strain partitioning and mechanical stability of retained austenite. *Scripta Materialia*, Vol. 63 (2010) pp. 297-299

Yi, H. L., Ryu, J. H., Bhadeshia, H. K. D. H., Yen, H. W., Yang, J. R.: Low-alloy duplex, directly quenched transformation-induced plasticity steel. *Scripta Materialia*, Vol. 65 (2011) pp. 604-607

Ryu, J. H., Chun, Y. S., Lee, C. S., Bhadeshia, H. K. D. H., Suh, D. W.: Effect of Deformation on Hydrogen Trapping and Effusion in TRIP-Assisted Steel. *Accepted to Acta Materialia*, (2012)

Ryu, J. H., Kim, S. K., Lee, C. S., Bhadeshia, H. K. D. H., Suh, D. W.: Effect of Al on Hydrogen Embrittlement in TWIP Steel. *To be submitted,* 2012